CHARACTERIZATION OF MOLECULAR BEAM EPITAXIALLY GROWN CDTE LAYERS OVER GAAS BY SPECTROSCOPIC ELLIPSOMETRY

A Thesis Submitted to
The Graduate School of Engineering and Sciences of
İzmir Institute of Technology
In Partial Fulfillment of the Requirements for the Degree of

MASTER OF SCIENCE

in Physics

by
Merve GÜNNAR

December 2014
İZMIR

We approve the thesis of **Merve GÜNNAR**

Examining Committee Members:

Assoc. Prof. Dr. Yusuf SELAMET
Department of Physics, İzmir Institute of Technology

Assoc. Prof. Dr. Gül GÜLPINAR
Department of Physics, Dokuz Eylul University

Assoc. Prof. Dr. Gülnur AYGÜN ÖZYÜZER
Department of Physics, İzmir Institute of Technology

19 December 2014

Assoc. Prof. Dr. Yusuf SELAMET
Supervisor, Department of Physics
İzmir Institute of Technology

Prof. Dr. Nejat BULUT
Head of the Department of Physics

Prof. Dr. Bilge KARAÇALI
Dean of the Graduate School of
Engineering and Sciences

ACKNOWLEDGEMENTS

I would like to first thank my parents for encouraging me during this work and their endless support.

I'm thankful to my advisor Assoc. Prof. Dr. Yusuf Selamet for giving me chance to study with him and also for teaching and sharing me his great knowledge about this study area. I also would like to thank him for his support and guidance through my research.

I would like to thank the other members of my thesis committee Assoc. Prof. Dr. Gül Gülpınar, Assoc. Prof. Dr. Gülnur Aygün Özyüzer for their participation.

I'm also very thankful to my colleagues and friends helped me and encouraged me to complete this thesis. Especially, I would like to thank Elif Bilgilisoy for her great friendship and for AFM measurements and Selin Özden for her FTIR measurements. I would like to thank Elif Özçeri for her encouraging me to complete this study on time. I would like to thank Begüm Yavaş for her friendship and helping me for the experimental process. I also thank to Mustafa Polat and Ozan Arı for XRD measurements. I would like to also thank to Hasan Aydın, Nesli Yağmurcukardeş, Emine Bakali, Alper Yanılmaz and Sinem Duman for their all contribution on this study.

I'm especially very thankful to Caner Karakaya who always encouraged and motivated me throughout my study.

I would also thank very much to Thomas Wagner for helping about ellipsometric data analysis procedure and Vural Köksal for teaching to use spectroscopic ellipsometer.

Finally, I wish to acknowledge the plentiful financial support of ASELSAN and SSM for all facilities in our laboratory.

ABSTRACT

CHARACTERIZATION OF MOLECULAR BEAM EPITAXIALLY GROWN CDTE LAYERS OVER GAAS BY SPECTROSCOPIC ELLIPSOMETRY

The infrared detectors consist of two main parts that are optical elements and sensing elements. The sensor component is generally formed by semiconductor materials that can detect Infrared (IR) light which cannot be seen by human eye. Mercury Cadmium Telluride (MCT, HgCdTe) is widely used as a sensor material for this purpose. The adjustable bandgap (0-1.5 eV) which corresponds to energies of IR light can be obtained by changing the composition x of cadmium (Cd) in the ternary alloy $Hg_{1-x}Cd_xTe$. HgCdTe has very high quantum efficiency for the detectible IR wavelengths in the atmospheric windows. HgCdTe which has a great importance in defense industry as an IR detecting material should be grown with high crystallinity in order to obtain high resolution images even under bad weather conditions. In addition, HgCdTe must be grown uniformly over a large area in order to have large format and high operability focal plane arrays.

The defect density of HgCdTe strongly depends on the lattice mismatch between substrate and HgCdTe. In order to reduce the lattice mismatch which causes dislocations in HgCdTe the best suitable option is to grow Cadmium Telluride (CdTe) buffer layer on a substrate before growing HgCdTe. Studies have been focusing on semiconductors which are Gallium Arsenide (GaAs), Silicon (Si) and Germanium (Ge) as alternative substrates for CdTe growth.

In this study, the CdTe films grown on (211) oriented GaAs wafers by molecular beam epitaxy (MBE) were characterized by *ex-situ* spectroscopic ellipsometry (SE). The properties of CdTe films such as thickness, surface roughness and optical constants were characterized by comparison with the growth conditions. It was also investigated that how these properties vary over the film surface. Characterization results were compared to those obtained by atomic force microscopy (AFM), Nomarski microscopy, Fourier transformation infrared spectroscopy (FTIR) and X-ray diffraction (XRD). The temperature dependencies of the optical properties of the material obtained by SE were also investigated.

ÖZET

MOLEKÜLER DEMET EPİTAKSİ İLE GAAS ÜZERİNE BÜYÜTÜLEN CDTE KATMANLARININ SPEKTROSKOPİK ELİPSOMETRİ İLE KARAKTERİZASYONU

Kızıl ötesi dedektörler optik kısım ve algılayıcı kısım olmak üzere iki ana bölümden oluşmaktadır. Algılayıcı kısım gözle görülmeyen kızıl ötesi ışınları algılayabilen yarı iletken malzemelerden yapılmaktadır. Algılayıcı malzeme olarak Cıva Kadmiyum Tellür (HgCdTe) kullanımı yaygındır. Kadmiyum (Cd) oranının değişmesi ile kızıl ötesi ışınların enerjisine denk gelen dar bant aralığı (0-1.5 eV) elde edilebilmektedir. HgCdTe atmosferik koşullarda algılanabilen kızılötesi dalga boyu aralıkları için yüksek kuantum etkisine sahip olması sebebiyle tercih edilmektedir. Savunma sanayinde kızıl ötesi algılayıcı olarak büyük öneme sahip olan HgCdTe malzemesinin olumsuz hava koşullarında da yüksek çözünürlüklü görüntü elde edilmesi için iyi kristal kalitede büyütülmesi ve daha iyi verim için geniş alanlı alt taban üzerine homojen olarak iyi kalitede büyütülmesi gerekmektedir.

HgCdTe'ün kristal kalitesi alt taban ile örgü uyumsuzluğunun azaltılmasına bağlıdır. Dislokasyonlara sebep olan bu örgü uyumsuzluğunu azaltmak için de en uygun seçenek Kadmiyum Tellür (CdTe) tampon katmanının kullanılmasıdır. CdTe büyütmede alternatif alt katman olarak Galyum Arsenik (GaAs), Silikon (Si) ve Germanyum (Ge) üzerine çalışmalar yoğunluk göstermektedir.

Bu çalışmada ise (211) yönelimli GaAs üzerine Moleküler ışın epitaksisi (MBE) ile büyütülen CdTe ince filmleri büyütme sonrası spektroskopik elipsometre (SE) ile karakterize edilmiştir. Elipsometre verisinin analizi için uygun model seçimi yapılmıştır. CdTe filmlerinin kalınlık, yüzey pürüzü ve optik özellikleri gibi parametreler büyütme koşulları ile karşılaştırılarak karakterize edilmiştir. Bu özelliklerin yüzey üzerinde nasıl dağıldığına bakılmıştır. Atomik kuvvet mikroskobu (AFM), Nomarski mikroskobu, Fourier dönüşümlü kızılötesi spektroskopisi (FTIR) ve X ışınları kırınımı (XRD) sonuçlarıyla karşılaştırılmıştır. Ayrıca malzemelerin SE ile tayin edilen optik özelliklerinin sıcaklık ile bağlılığı incelenmiştir.

TABLE OF CONTENTS

LIST OF FIGURES viii

LIST OF TABLES xiii

LIST OF ABBREVIATIONS xiv

CHAPTER 1. INTRODUCTION 1

CHAPTER 2. SPECTROSCOPIC ELLIPSOMETRY 3

2.1.History and Purpose 3

2.2.What Is Spectroscopic Ellipsometry? 4

2.3.Polarization of Light 6

2.3.1.Jones Vector and Jones Matrix 7

2.4.Dielectric Function of Reflecting Medium 9

2.5.Properties of the Spectroscopic Ellipsometer 14

2.6.Ex Situ Data Analysis Procedure 15

2.7.Optical Model Construction 21

2.7.1.Lorentz model 22

2.7.2.Cauchy Model for Transparent Materials 25

2.7.3.General Oscillator Model for Semiconductors 26

2.7.3.1.Band Structure and Critical Points 29

2.7.4.Effective Medium Approximation 31

CHAPTER 3. HGCDTE AND CDTE ON ALTERNATIVE SUBSTRATES 33

3.1.HgCdTe for IR detectors 33

3.2.Alternative Substrates for HgCdTe Growth 36

3.3.HgCdTe and CdTe Growth 38

CHAPTER 4. DIELECTRIC FUNCTION DETERMINATION 39

4.1.Woollam Library Model 39

4.2.General Oscillator Model 44

4.2.1.CdTe Band Structure and Critical Points 51
4.2.1.1.Temperature Dependency of Critical Points of CdTe 57
4.2.2.CdZnTe Band Structure and Critical Points................................... 60
4.2.3.GaAs Band Structure and Critical Points....................................... 63

CHAPTER 5. EXPERIMENTAL RESULTS FOR CDTE GROWN ON GAAS 67
5.1.MBE Grown CdTe Buffer Layers... 67
5.1.1.CdTe Thickness Determination... 70
5.1.2.Growth Uniformity of CdTe 73
5.1.3.CdTe Surface Roughness Obtained From SE and AFM................. 81
5.2.MBE Grown CdTe Nucleation Layers 85

CHAPTER 6. CONCLUSIONS AND FUTURE STUDIES.. 91

REFERENCES 93

LIST OF FIGURES

Figure **Page**

Figure 1. Illustration of polarization planes of light and elliptical polarization angles 4
Figure 2. Spectroscopic ellipsometry characterization process 5
Figure 3. Illustration of linearly polarized incident light and elliptically polarized reflected light [20]. 6
Figure 4. Examples for polarization states; (a) linear polarization, (b) circular polarization, (b) elliptical polarization [20]. 7
Figure 5. Ellipsometric components and corresponding Jones matrices. 9
Figure 6. Refraction and reflection of the incident light. 10
Figure 7. Imaginary and real part of the dielectric function of (a) transparent material SiO_2 (a) semiconductor Si, and (c) metal material Al. 13
Figure 8. The spectroscopic ellipsometer used for this study. 14
Figure 9. Configuration of a rotating analyzer ellipsometer (RAE) [24]. 15
Figure 10. Rotating-compensator ellipsometer (RCE). 15
Figure 11. Ellipsometric data analysis flow chart [25]. 16
Figure 12. Experimental data of pseudo dielectric function of Si with a native oxide... 17
Figure 13. Si with native oxide model. 17
Figure 14. Optical constants of (a) Si and (b) oxide layer. 17
Figure 15. Model data for Si with native oxide sample. 18
Figure 16. Experimental and model data for Si with native oxide. 18
Figure 17. MSE versus native oxide thickness. 19
Figure 18. Dielectric function models used in ellipsometry [20]. 21
Figure 19. Classical Lorentz model [20]. 22
Figure 20. An example of dielectric function calculated from the Lorentz model [20]. 24
Figure 21. Imaginary part of the dielectric function of GaAs at Woollam library and Lorentz model with six oscillators. 25
Figure 22. Optical constants versus wavelength according to Cauchy model with parameters A=1.45, B=0.05 and C=0.0. 26
Figure 23. Harmonic and Lorentz oscillator model with same parameter values. (A_j=5, Γ_j=0.5 eV, E_{oj}=2.25 eV). 27

Figure 24. Gaussian and Lorentz oscillator model with same parameter values. (A_j=5, Γ_j=0.5 eV, E_{oj}=2.25 eV). 28
Figure 25. Psemi-tri oscillator. 28
Figure 26. Psemi-Tri oscillators for three different values of broadening (Br or Γ) parameters. Other parameters are same for all oscillators (A_j=1, AL_j=0.75, AR_j=0.2, Ec_j=2 eV, WL_j=0.2 eV and WR_j=1 eV). 29
Figure 27. Imaginary part of the CdTe dielectric function at 20 K (solid line), 208 K (dot and dashed line), and 294 K (dashed line) [33]. 30
Figure 28. Electronic band structure of CdTe at 0 K calculated with the empirical pseudo-potential method [35]........ 30
Figure 29. Evolution of EMA overlayer of CdTe during growth on GaAs [11]. 31
Figure 30. EMA and surface roughness........ 32
Figure 31. Energy band structures of CdTe and HgTe at room temperature and band gap range for $Hg_{1-x}Cd_xTe$. 33
Figure 32. Energy gap value of $Hg_{1-x}Cd_xTe$ versus Cd fraction near the Γ point. 34
Figure 33. Electromagnetic wave spectrum. 34
Figure 34. The atmospheric transmission versus IR wavelength. 35
Figure 35. Substrates for HgCdTe growth 36
Figure 36. Energy gap versus lattice parameter for several materials [60]. 37
Figure 37. Gen-20MZ MBE system facility in the department of physics at Iztech. 38
Figure 38. Imaginary (e2) and real part (e1) of the dielectric function of the CdTe Oxide Cauchy material in Woollam library. 40
Figure 39. Imaginary and real part of the dielectric function of the CdTe material in Woollam library. 41
Figure 40. Imaginary and real part of the dielectric function of the GaAs material in Woollam library. 41
Figure 41. Experimental and Woollam model fit data of pseudo-dielectric function of the CdTe film on GaAs (Sample CT7). 42
Figure 42. The optical model for CdTe on GaAs film by using Woollam library for each layer........ 42
Figure 43. Depolarization data and model fit. 43
Figure 44. Imaginary and real part of the dielectric function of the CdTe material (Sample CT7) which was formed using 5 general oscillators........ 45

Figure 45. Experimental and 5 gen-osc model data of pseudo-dielectric function of the CdTe on GaAs film (Sample CT7).. 45
Figure 46. The optical model for CdTe on GaAs film by using 5 general oscillators for CdTe layer. 46
Figure 47. Imaginary and real part of the dielectric function of the CdTe material (Sample CT7) which was formed using 7 general oscillators....................... 47
Figure 48. Experimental and 7 gen-osc model data of pseudo-dielectric function of the CdTe on GaAs film (Sample CT7).. 47
Figure 49. The optical model for CdTe on GaAs film by using 7 general oscillators for CdTe layer. 48
Figure 50. Imaginary and real part of the dielectric function of the CdTe material (Sample CT7) which was formed using 9 general oscillators....................... 49
Figure 51. Experimental and 9 gen-osc model data of pseudo-dielectric function of the CdTe on GaAs film (Sample CT7).. 49
Figure 52. The optical model for CdTe on GaAs film by using 9 general oscillators for CdTe layer. 50
Figure 53. Imaginary part of dielectric function of CdTe near the bandgap and the psemi-tri oscillator (Sample CT7).. 51
Figure 54. Real part of dielectric function of CdTe near the bandgap (Sample CT7).... 52
Figure 55. Imaginary part of the CdTe dielectric function and some critical points for the band structure of CdTe using 9 Gen-Osc model. 53
Figure 56. Comparison of critical points obtained from oscillator parameters and derivation of e2.. 54
Figure 57. Comparison of critical points of CdTe at room temperature obtained from [65], [33] and 9 oscillator model.. 55
Figure 58. Comparison of broadening parameters of CdTe at room temperature from different studies. 56
Figure 59. Imaginary part and first derivative of imaginary part of the CdTe dielectric function.. 56
Figure 60. Imaginary part and second derivative of the imaginary part of the CdTe dielectric function. Arrow indicates the bandgap value of 1.506 eV.. 57
Figure 61. Temperature dependency of CdTe imaginary part dielectric function of sample CT7. 58

Figure 62. Temperature dependency of CdTe imaginary part dielectric function from 2.7 eV to 4.2 eV for sample CT7 58
Figure 63. Temperature dependency of critical points E_1 and $E_1+\Delta$ of CdTe. 59
Figure 64 Temperature dependency of $E_1$of CdTe obtained from Li et al. [69] 59
Figure 65. Temperature dependency of critical points E_g and E_1 of CdTe. 60
Figure 66. Real and imaginary parts of the pseudo dielectric function of the CdZnTe bulk with native oxide. 61
Figure 67. Real and imaginary parts of the dielectric function of the CdZnTe bulk that was modeled with 9 general oscillators. 62
Figure 68. Real part of the dielectric function of the CdZnTe (4 % Zn) and CdTe near the bandgap. 62
Figure 69. Real and imaginary parts of the pseudo dielectric function of the GaAs substrate with oxide. 64
Figure 70. Band structure of GaAs and its main inter-band transitions [35]. 65
Figure 71. Imaginary parts of the dielectric function of the GaAs that was modeled with 6 general oscillators. E_1=2.909 eV, $E_1+\Delta$= 3.095 eV, E_o'=4.424 eV and $E_2+\Delta$=4.701 eV. 65
Figure 72. Real part and second derivative of real part of the dielectric function of the GaAs sample. 66
Figure 73. Comparison of the three different GaAs samples at room temperature. Dotted lines are GaAs materials in Woollam library and solid lines are our modeled GaAs sample. 66
Figure 74. RHEED patterns before (left) and after deoxidation of GaAs. 68
Figure 75. VI/II rate versus bandgap of CdTe. 69
Figure 76. <e1> and <e2> versus wavelength for CT10 (5054.17 nm). 71
Figure 77. <e1> and <e2> versus wavelength for CT13 (2147.63 nm). 71
Figure 78. <e1> and <e2> versus wavelength for CT7 (1045.52 nm). 71
Figure 79. CdTe thickness obtained from SE measurements and FTIR measurements. 72
Figure 80. CdTe thicknesses versus FWHM values. 72
Figure 81. CT9 thickness map. 73
Figure 82. CT9 optical image and 51 points that measurements were taken. 75
Figure 83. 30x30 μm^2 AFM images of CT9 for four regions. (a) RMS=18.7 nm, (b) RMS=15.5 nm, (c) RMS= 7.6 nm, (d), RMS= 16.4 nm. 75
Figure 84. CT9 <e2> (3.31 eV) map. 76

Figure 85. CT9 refractive index map (n values at 632.8 nm). 76
Figure 86. CT10 thickness map. 78
Figure 87. CT10 refractive index map (n values at 632.8 nm). 78
Figure 88. CT13 thickness map. 80
Figure 89. CT13 <e2> (3.31 eV) map 80
Figure 90. Comparison of imaginary parts of the pseudo dielectric functions of CT1, CT3, CT4, CT5, CT6, CT10, CT14 and CT15. 81
Figure 91. RMS roughness values versus <e2> values at 3.31 eV for CT1, CT3, CT4, CT5, CT6, CT10, CT14 and CT15.. 82
Figure 92. Exponantially fitted RMS roughness values versus <e2> values at 3.31 eV for CT1, CT3, CT4, CT5, CT6, CT10, CT14 and CT15............................... 82
Figure 93. AFM images of (a) CT1 (rms=3.01 nm), (b) CT3 (rms=8.4 nm), (c) CT6 (rms=10.63 nm), (d) CT4 (rms=21.12 nm), (e) CT15 (rms=25.44 nm), (f) CT14 (rms=35.53 nm)... 84
Figure 94. Surface images of (a) CT5, (b) CT6, (c) CT15, (d) CT14 samples obtained by Nomarski microscope (100x zoom). 85
Figure 95. Comparison of imaginary parts of the pseudo dielectric functions of CT16 (8.02 nm), CT17 (8.45 nm) and CT20 (8.89 nm) nucleation layer samples. . 87
Figure 96. Comparison of imaginary parts of the pseudo dielectric functions of CT18 (~4 nm) and CT21 (~150 nm), nucleation layer samples and GaAs and CT7 (~1000 nm). 88
Figure 97. Comparison of imaginary parts of the pseudo dielectric functions of CT18 (~4 nm), CT17 (~8 nm), CT19 (~25 nm) and CT21 (~150 nm) nucleation layer samples. 89
Figure 98. Comparison of imaginary parts of the dielectric functions which were obtained from two different layer model (CdTe/Oxide/GaAs and Oxide/CdTe/GaAs) for CT17 and CdTe in the software library.................. 90
Figure 99. Comparison of imaginary parts of the dielectric functions which were obtained from CdTe/Oxide/ GaAs layer model for CT16, CT17, CT20 andCT21 and imaginary part of the dielectric function of CdTe in the software library. 90

LIST OF TABLES

Table **Page**

Table 1. Comparison of substrates for HgCdTe/CdTe growth (Adapted from [56]). 37

Table 2. Comparison of the three alternate models and 9 Gen-Osc model. 50

Table 3. Comparison of some CdTe parameters obtained from four different models. . 52

Table 4. Comparison of critical points of CdTe at room temperature from different studies. 54

Table 5. Comparison of broadening parameters of CdTe at room temperature from different studies. 55

Table 6. Critical transition energies of CdZnTe (Zn, 4%) obtained from different methods and their comparison. 63

Table 7. CdTe films grown on GaAs and some characterization results and growth parameters. 69

Table 8. The growth conditions of CT16, CT17, CT18, CT19, CT20 and CT21. 86

Table 9. SE data analysis results according to two different models. 86

LIST OF ABBREVIATIONS

AFM	Atomic Force Microscopy
CdTe	Cadmium Telluride
CdZnTe	Cadmium Zinc Telluride
CP	Critical Point
EMA	Effective Medium Approximation
FTIR	Fourier Transformation Infrared
FWHM	Full Width at Half Maximum
GaAs	Gallium Arsenide
HOA	Harmonic Oscillator Approximation
IR	Infrared
IZTECH	İzmir Institute of Technology
LWIR	Long Wavelength Infrared
MBE	Molecular Beam Epitaxy
MCT	Mercury Cadmium Telluride (HgCdTe)
MDF	Model Dielectric Function
MWIR	Mid Wavelength Infrared
RAE	Rotating Analyzer Ellipsometry
RCE	Rotating Compensator Ellipsometry
RHEED	Reflection High Energy Electron Diffraction
RTSE	Real Time Spectroscopic Ellipsometry
SE	Spectroscopic Ellipsometry
SWIR	Small Wavelength Infrared
XRD	X-ray Diffraction

CHAPTER 1

INTRODUCTION

High performance IR detectors are fabricated by using HgCdTe as sensor material which is the most effective material under atmospheric conditions. The short wavelength (SWIR), middle wavelength infrared (MWIR) and long wavelength infrared (LWIR) detectors can be produced by changing Cd composition of HgCdTe [1].

HgCdTe growth over CdZnTe with 4% Zn composition substrates are preferred especially for LWIR window due to very low lattice mismatch and very low thermal expansion coefficient mismatch with HgCdTe [2]. However, CdZnTe has some disadvantages like lack of uniformity in crystallinity and Zn distribution on large area substrates, high cost per unit area, and the low mechanical strength. For these reasons alternative substrates such as Si [3], Ge [4], GaAs [5] and InSb [6] have been studying for HgCdTe growth. Between alternative substrates and HgCdTe, a CdTe buffer layer is grown to reduce lattice mismatch. In some studies, nucleation layers like ZnTe [7] between CdTe and alternative substrates was grown in order to reduce lattice mismatch and to maintain the surface orientation of the substrate.

Ellipsometric measurements are frequently used in this area to characterize CdTe film or to determine the composition of Cd in HgCdTe. In the standard *in situ* ellipsometric data analysis model that includes dielectric functions of a bulk layer, film layer and a surface roughness which is modelled in the effective medium approximation (EMA) is generally used [8]. EMA thickness which can be considered as surface roughness and surface roughness value obtained from atomic force microscopy (AFM) was found to be in good agreement [9]. Composition and temperature of a sample can also be simultaneously controlled using ellipsometry during growth [10].

In this study, GaAs (211)B was used as the choice of substrate for all growths for the following reasons; GaAs is commercially available as "epiready" so it does not require chemical preparation before the growth. In addition, the lattice mismatch between CdTe and GaAs is %14. 6 which is lower than the lattice mismatch between CdTe and Si substrate (19.6%). Furthermore, the polar nature of GaAs simplifies the

growth of Te rich surface (B-face) of CdTe. B face is needed in HgCdTe growth due to larger Hg sticking coefficient on this surface [11].

CdTe films grown on GaAs by molecular beam epitaxy (MBE) were characterized by *ex-situ* spectroscopic ellipsometer (SE). A proper model which includes dielectric functions of GaAs bulk, CdTe film layer and oxide layer on the surface was selected to analyze *ex situ* ellipsometric data.

- In the following chapter, the theoretical background, measurement principle and data analysis procedure of the spectroscopic ellipsometry and some knowledge about ellipsometer configuration were given.
- In Chapter 3, motivation behind the CdTe growth on GaAs and some background information about HgCdTe material for IR detectors were given. Various CdTe growth techniques were compared and MBE growth technique was explained.
- In Chapter 4, dielectric function determination and selection of an optical model for a CdTe on GaAs sample for ellipsometric characterization were demonstrated. Temperature dependency of dielectric function and its critical points of CdTe for this sample were mentioned. The ternary alloy CdZnTe and epiready GaAs were also characterized by SE and their dielectric functions were constructed.
- In Chapter 5, experimental results and discussions of molecular beam epitaxially grown CdTe thin films were given. These samples were grown under different growth conditions and had different thicknesses. For these samples SE determined thickness values were correlated with those obtained by FTIR measurements. In addition, the growth uniformity was also determined for some of the samples by mapping film thicknesses and several optical parameters. Surface roughnesses of these samples were compared with some of their optical properties and with those obtained by AFM measurements. The *ex situ* ellipsometric measurements were also carried out for six nucleation samples and various locations over the surfaces were used while modeling these samples.
- In Chapter 6, conclusions drawn from this study were given.

CHAPTER 2

SPECTROSCOPIC ELLIPSOMETRY

2.1. History and Purpose

Ellipsometric studies were firstly performed by Paul Drude in late 1880s [12]. His experimental studies were on both absorbing and transparent solids. He constructed the optical properties of those solids at only a few wavelengths due to the absence of fast computational methods. Nonetheless, his results were very close to Palik's studies which were carried out by a modern computer [13, 14]. After Paul Drude, very little development was reported for a while about ellipsometry, however, in 1945 Alexandre Rothen defined the half-shade technique to detect the change of the polarization state of light upon reflection from a sample surface, and suggested the term "ellipsometry" [15].

In 1960s and 1970s, automated ellipsometers were developed for various purposes [16]. Two main types of automated ellipsometers are still widely used: (i) rotating element ellipsometer and (ii) the phase modulator ellipsometer [17]. The photon energy range and number of wavelengths of spectroscopic ellipsometry has extended over the years. First rotating analyzer ellipsometer (RAE) covering near-infrared (NIR) to near-ultraviolet range was developed by D. E. Aspnes and A. A. Studna in 1975 [18]. In order to obtain the entire spectral range simultaneously for analysis of thin film growth and materials processing, the technique of real time spectroscopic ellipsometry (RTSE) was developed in 1990 [19].

SE is widely used to determine the optical properties of materials. Thin film thicknesses can be found by using optical models. In order to carry out thickness measurements by spectroscopic ellipsometry, the light must penetrate through the thin film, reflect from the substrate interface, return through the film, and reach the detector. For this reason, wide spectral range is important to determine the thickness of the film. In order to determine the thickness of a semiconductor film, the light spectrum must have lower energies than the bandgap of the semiconductor. Therefore, these lights cannot be absorbed and can be reflected from the interface of the film that enables wave superposition and phase shifts. In addition to thickness, other properties such as

roughness, crystal quality, alloy composition, area uniformity, and temperature of the growth surface may be determined by SE. Real time measurements may also provide a depth profile of the film structure [13].

2.2. What Is Spectroscopic Ellipsometry?

Spectroscopic Ellipsometry (SE) is a measurement technique that determines the dielectric function of sample by measuring the polarization angles of reflected or transmitted light. There are two polarization angles psi (ψ) and delta (Δ). Psi is related to the amplitude ratio of the electric field components of polarized light and delta is related to phase difference of light that moves through polarization planes. These two polarization planes are generally labeled as 's' and 'p' planes. The s plane axis is parallel to sample surface and the p plane axis is perpendicular to the s plane axis (Figure 1).

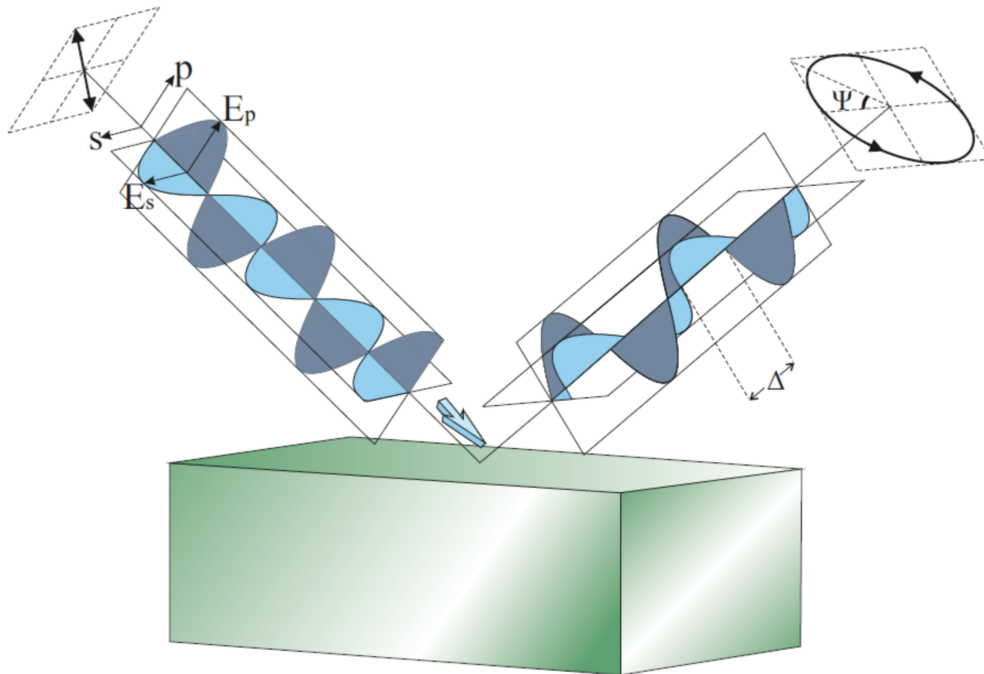

Figure 1. Illustration of polarization planes of light and elliptical polarization angles

In ellipsometric measurement, generally the linearly polarized light is sent to the sample surface and reflected light becomes elliptically polarized. The measured parameters ψ and Δ which are light energy depended, yield film thickness and optical

constants of the sample after constructing an optical model. Some important information about the sample, such as energy bandgap, surface temperature, alloy composition etc. can be determined by obtaining the optical constants (dielectric constants or refractive index) of the sample. The characterization process of some properties of a material is indicated in Figure 2.

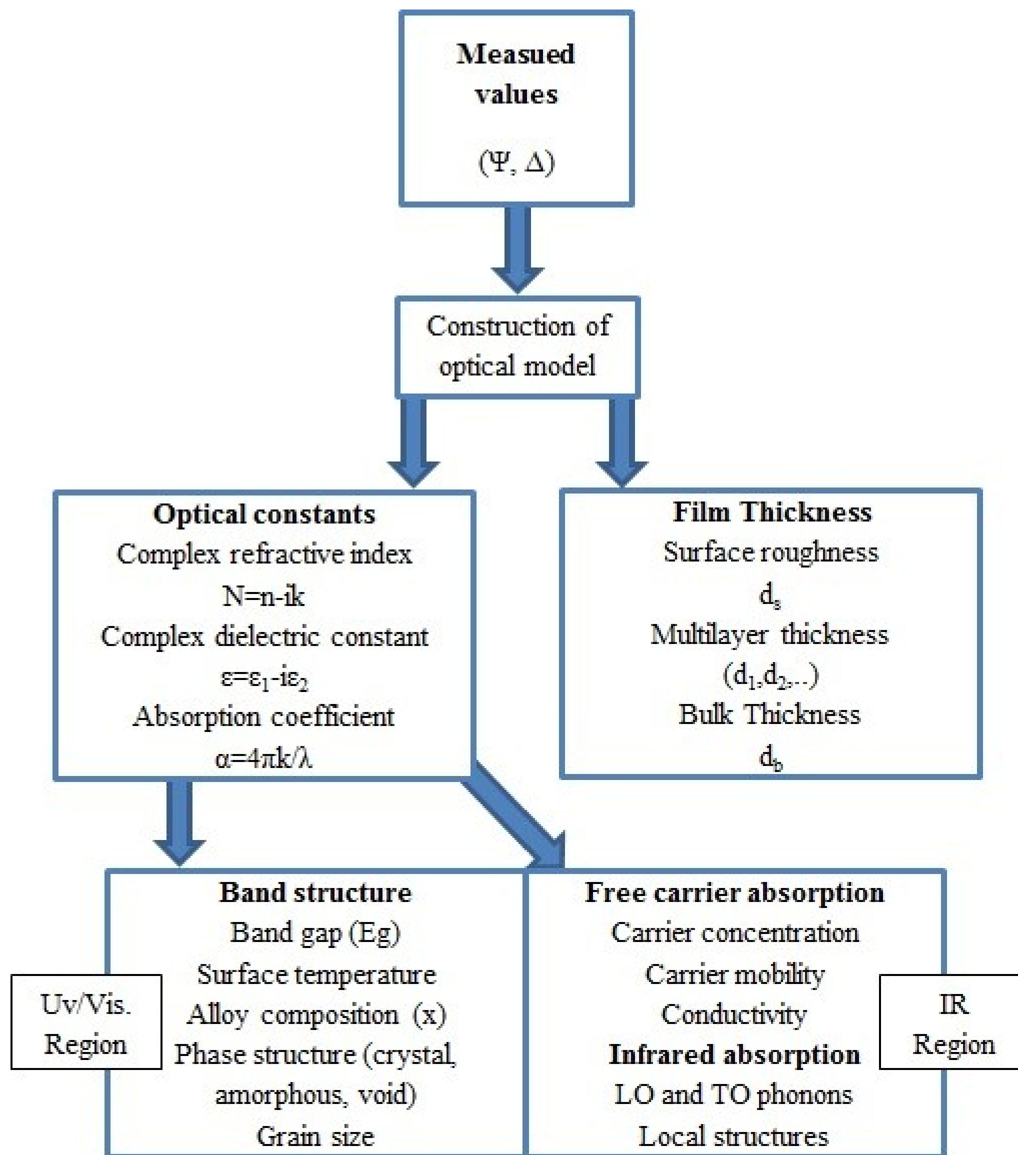

Figure 2. Spectroscopic ellipsometry characterization process

2.3. Polarization of Light

Spectroscopic Ellipsometry measurements are performed by determining the polarization states of light. Polarized light is such light that its electric fields are oriented in specific directions. As it is seen in Figure 1 the polarization planes s and p represent polarization of the waves. It can be also seen in Figure 3 that how linearly polarized light becomes elliptically polarized after reflecting on a sample. There are two kinds of parameter that specify polarization states of light;

1) Phase difference between E_s and E_p planes (Δ)
2) The angle related to the amplitude ratio of E_s and E_p electric fields (ψ)

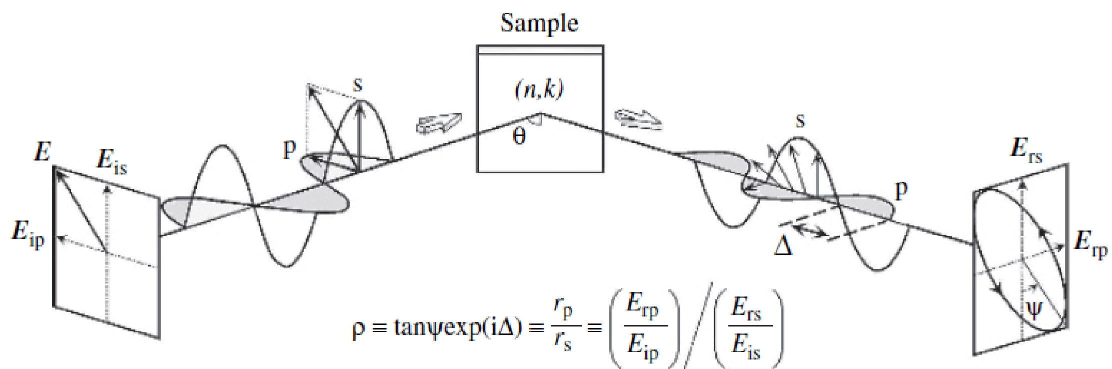

Figure 3. Illustration of linearly polarized incident light and elliptically polarized reflected light [20].

Figure 4 shows three specific polarization states. If the phase difference between E_s and E_p is zero (Δ=0), this light is said to be linearly polarized (Figure 4a). Circular polarization is also a kind of specific polarization state that require the angles to be $\Delta=90^o$ and $\psi=45^o$ (Figure 4 b). As an example of elliptical polarization the state $\Delta=45^o$ and $\psi=45^o$ is given in Figure 4c. Elliptical polarization is a general state that occurs almost in all configurations of polarization angles with the exceptions of circular and linear polarization.

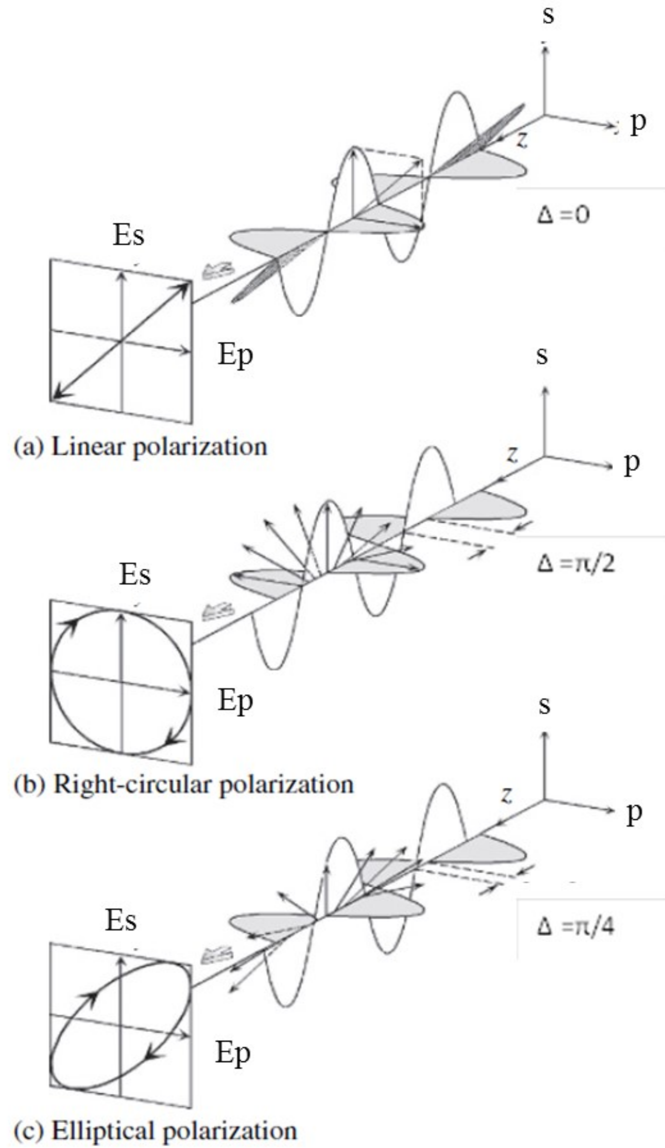

Figure 4. Examples for polarization states; (a) linear polarization, (b) circular polarization, (b) elliptical polarization [20].

2.3.1. Jones Vector and Jones Matrix

Jones vectors are utilized to explain the states of polarization of light. The electric field of light in terms of the electrical field components is written as Jones vector:

$$\mathbf{E} = \begin{bmatrix} E_s \\ E_p \end{bmatrix} \tag{2.1}$$

where $E_s=E_{s0}\exp(i\Delta)$ and $E_p=E_{p0}$ [20]. As an example, linearly s-polarized light $(\psi,\Delta)=(90^o,0^o)$ and p-polarized light $(\psi,\Delta)=(0^o,0^o)$ can be written as:

$$\mathbf{E}_{linear,s}=\begin{bmatrix}1\\0\end{bmatrix}, \quad (2.2)$$

$$\mathbf{E}_{linear,p}=\begin{bmatrix}0\\1\end{bmatrix}. \quad (2.3)$$

The linear polarization state on which the light oriented at 45° between s and p direction is $(\psi,\Delta)=(45^o,0^o)$ and Jones vector is expressed as:

$$\mathbf{E}_{linear}=\frac{1}{\sqrt{2}}\begin{bmatrix}1\\1\end{bmatrix}. \quad (2.4)$$

Jones vector that represents the general case of elliptical polarization [20] in terms of ψ and Δ is given as,

$$\mathbf{E}_{elliptical}=\begin{bmatrix}\sin\psi\exp(i\Delta)\\\cos\psi\end{bmatrix}. \quad (2.5)$$

In order to give an example for Jones vector of an elliptically polarized light the case $(\psi, \Delta) = (45^o,45^o)$ can be chosen. In this case the electric field of light is written as:

$$\mathbf{E}_{elliptical}=\frac{1}{2}\begin{bmatrix}1+i\\\sqrt{2}\end{bmatrix}. \quad (2.6)$$

In ellipsometric measurement set-up, there are various optical elements such as analyzer, polarizer and compensator etc. Each element can be mathematically described by a Jones matrix (Figure 5). By applying the Jones matrix to any Jones vector one can obtain Jones vector of the new polarization state.

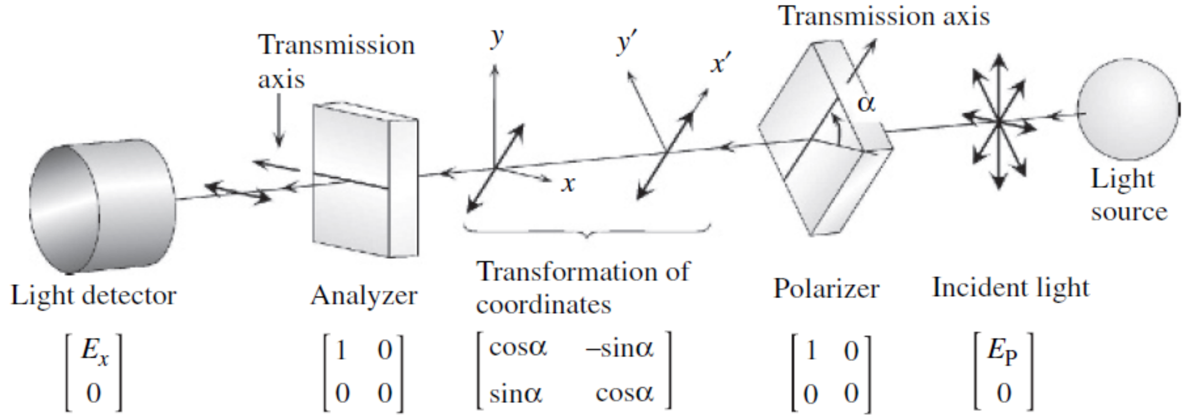

Figure 5. Ellipsometric components and corresponding Jones matrices [20].

2.4. Dielectric Function of Reflecting Medium

When light moves into a medium some portion of light is transmitted into the medium and the rest of the light is reflected from the surface. The dielectric properties of the medium can be determined by measuring the elliptical polarization states of the reflected or transmitted light. By using two basic optical laws (Snell's law and Fresnel equations) one can derive dielectric function of the medium. In this section derivation of the dielectric function of reflected medium is given.

There are four Fresnel coefficients R_p, R_s, T_p and T_s. These coefficients give the proportion of the electric field of incident light to that of the reflected light and the electric field of the incident light to the electric field of the transmitted light for p- and s-polarized light, respectively.

In order to find the dielectric function of the medium, either reflectance coefficients or transmittance coefficients are used. In this derivation only reflectance coefficients are used to derive dielectric function of the medium due to the fact that only reflected light is analyzed by spectroscopic ellipsometer. Fresnel coefficients (R_p, Rs) are given by [21],

$$R_P=\frac{N\cos\theta_i-n\cos\theta_t}{n\cos\theta_t+N\cos\theta_i}, \tag{2.7}$$

$$R_s=\frac{n\cos\theta_i-N\cos\theta_t}{n\cos\theta_i+N\cos\theta_t}, \tag{2.8}$$

where N is the complex refractive index of the medium, n is the refractive index of the ambient through where light moves, θ_i is the angle between surface normal and incident light, θ_t is the angle between surface normal and transmitted light (Figure 6). Snell's law is also used to determine the angle of transmittance θ_t;

$$N\sin\theta_t = n\sin\theta_i \tag{2.9}$$

It is important to use Snell's law in order to reduce an unknown parameter in Fresnel's coefficients. We assume that θ_i and n parameters are known. If we take square for both sides of Snell's equation, $\cos\theta_t$ can be easily obtained.

$$N^2\sin^2\theta_t = n^2\sin^2\theta_i \tag{2.10}$$

where $\sin^2\theta = 1-\cos^2\theta$ then,

$$\cos\theta_t = \pm\frac{\sqrt{N^2-n^2\sin^2\theta_i}}{N} \tag{2.11}$$

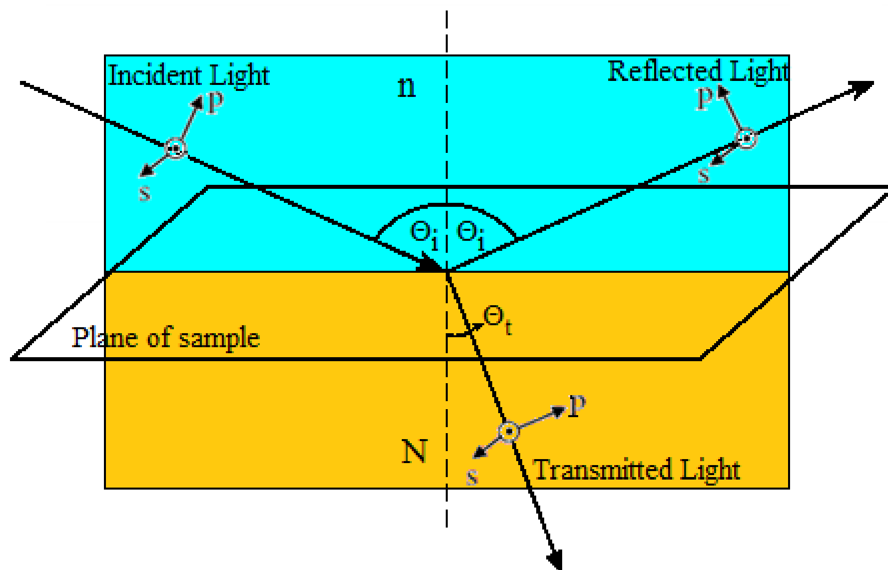

Figure 6. Refraction and reflection of the incident light.

The R_p/R_s ratio also gives the ratio of the electric field of reflected p-polarized light to that of s-polarized light due to the fact that the ratio of the electric field of incident p- and s- polarized light is one. So this gives [20],

$$\rho=\frac{R_p}{R_s}=\tan\psi e^{i\Delta} \tag{2.12}$$

By using equation (2.7) and equation (2.8) and rewriting $\cos\theta_t$ with equation (2.11) the ratio Rp/Rs gives:

$$\rho=\frac{n\sin^2\theta_i\mp\cos\theta_i\sqrt{N^2-n^2\sin^2\theta_i}}{n\sin^2\theta_i\pm\cos\theta_i\sqrt{N^2-n^2\sin^2\theta_i}} \tag{2.13}$$

where N is an unknown parameter, but other parameters (n, θ_i, ρ) are accessible. Therefore, this equation can be rewritten as,

$$N^2=n^2\sin^2\theta_i\left[1+\left(\frac{1-\rho}{1+\rho}\right)^2\tan^2\theta_i\right] \tag{2.14}$$

or

$$N^2=n^2\sin^2\theta_i\left[1+\left(\frac{1-\tan\psi e^{i\Delta}}{1+\tan\psi e^{i\Delta}}\right)^2\tan^2\theta_i\right] \tag{2.15}$$

From Maxwell's equations, the relation between refractive index and dielectric constant can be written as [22],

$$N^2=\varepsilon \tag{2.16}$$

So the equation (2.15) becomes,

$$\varepsilon=\varepsilon_0\sin^2\theta_i\left[1+\left(\frac{1-\tan\psi e^{i\Delta}}{1+\tan\psi e^{i\Delta}}\right)^2\tan^2\theta_i\right] \tag{2.17}$$

where the measured values ψ and Δ are energy dependent and the incident angle θ_i is a known parameter. If the ambient is air or vacuum, the dielectric constant is taken as

ε_0=1. Because of the fact that the sample may include not only one homogeneous layer, but also it has a surface layer or multi-layer structure, the measured dielectric function is said to be a pseudo-dielectric function. Therefore, pseudo-dielectric function can be expressed as,

$$\langle\varepsilon\rangle=\sin^2\theta_i\left[1+\left(\frac{1-\tan\psi e^{i\Delta}}{1+\tan\psi e^{i\Delta}}\right)^2\tan^2\theta_i\right] \qquad (2.18)$$

It is easily seen from the equation that dielectric function is a complex quantity so the dielectric function has both real part, ε_1, and imaginary part, ε_2. Consequently, refractive index N consists of real part n and imaginary part k;

$$\varepsilon=\varepsilon_1-i\varepsilon_2 \qquad (2.19)$$

$$N=n-ik \qquad (2.20)$$

According to the equation, $N^2=\varepsilon$, real part ε_1 and imaginary part ε_2 can be expressed as,

$$\varepsilon_1=n^2-k^2 \qquad (2.21)$$

$$\varepsilon_2=2nk \qquad (2.22)$$

where k is the extinction coefficient. When light is not absorbed by the sample, the extinction coefficient is zero. The absorption coefficient is also directly proportional to extinction coefficient,

$$\alpha=\frac{4\pi k}{\lambda} \qquad (2.23)$$

where α is absorption coefficient and λ is the wavelength of the light. For transparent materials $\alpha=k=\varepsilon_2=0$ for the given spectrum. In order to understand the behavior of imaginary and real part of the dielectric functions, some examples are given in Figure 7 for transparent materials, semiconductors and metals.

The dielectric function defines the electrical and optical properties of a material versus wavelength, or energy. The dielectric function basically describes the electric

polarizability and absorption properties of the material. The real part of the dielectric function ε_1 represents amount of electric dipoles in the material when an electric field is applied. If the induced dipole oscillations in a material become large the material may start absorbing energy from the applied electric field. When absorption takes place the imaginary part of the dielectric function ε_2 becomes important.

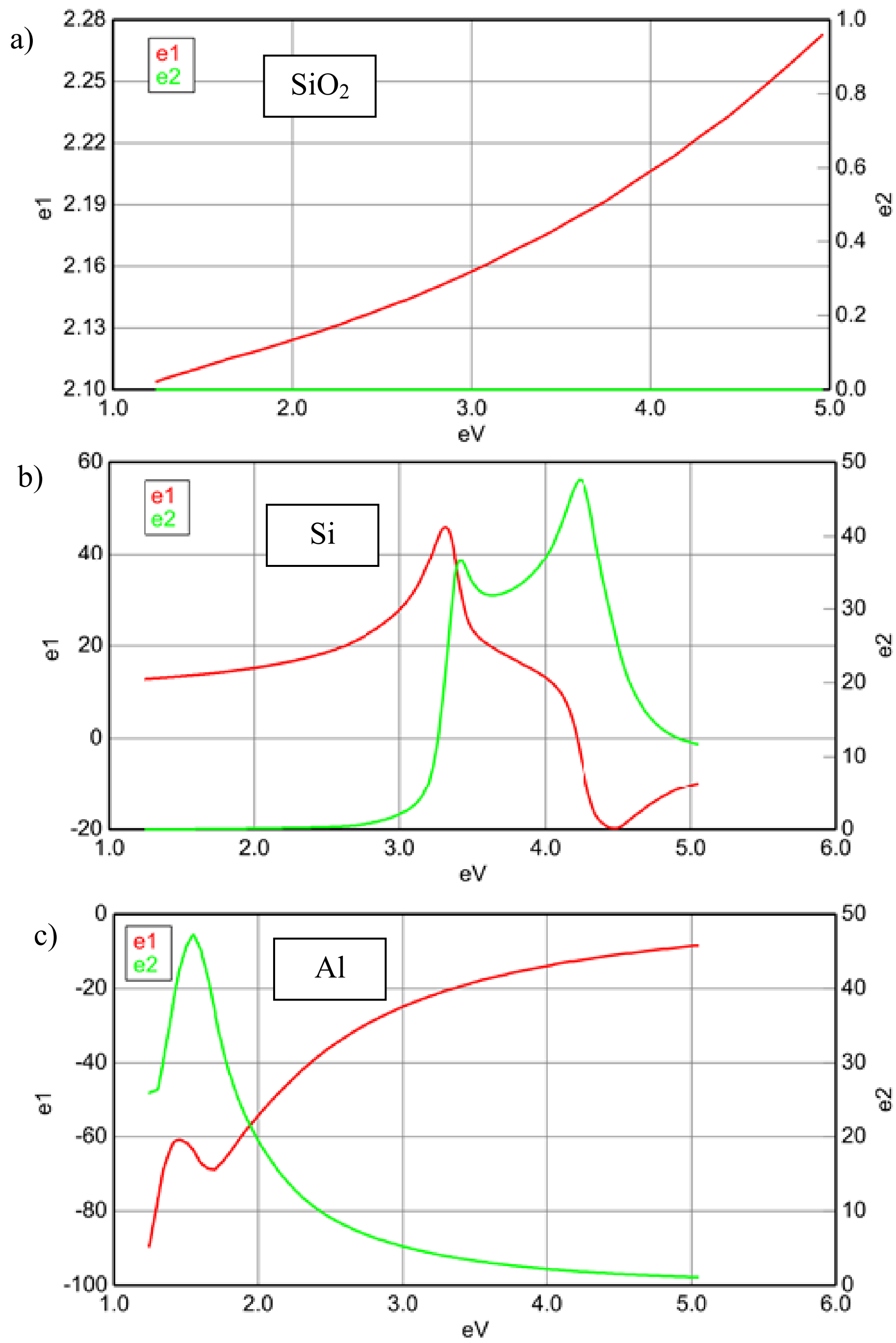

Figure 7. Imaginary and real part of the dielectric function of (a) transparent material SiO_2 (a) semiconductor Si, and (c) metal material Al.

2.5. Properties of the Spectroscopic Ellipsometer

The spectroscopic ellipsometer used for this study is model M-2000X of J. A. Woollam Company (Figure 8), which is a rotating-compensator ellipsometer (RCE). The photon energy range is from 1.24 eV to 5.05 eV (or wavelength range is from 245 nm to 1000 nm). This spectrum is divided into 470 wavelengths. 75W Xenon arc lamp is used as light source. *Ex-situ* measurements were carried out at a fixed incidence angle. of 65.82^o.

Figure 8. The spectroscopic ellipsometer used for this study.

Before RCE technology the first instruments used were rotating polarizer ellipsometer (RPE) or rotating analyzer ellipsometer (RAE) (Figure 9). RPE and RAE systems have some particular limitations: the parameter Δ value will be poor when it is near 0° or 180° and Δ value will be reported as $\Delta = 360^o - \Delta_{actual}$ when $\Delta > 180^o$. On the contrary, RCE systems provide ellipsometric data more accurately. The parameters ψ and Δ are measured reliably over their full ranges (ψ:0-90°, Δ:0-360°). For greater accuracy, especially in *in situ* measurements, the angle of incidence is chosen near Brewster's angle to keep $\Delta \sim 90^o$ or to keep it away from 180° or 0° [23].

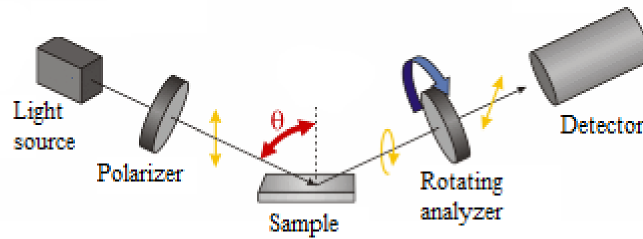

Figure 9. Configuration of a rotating analyzer ellipsometer (RAE) [24].

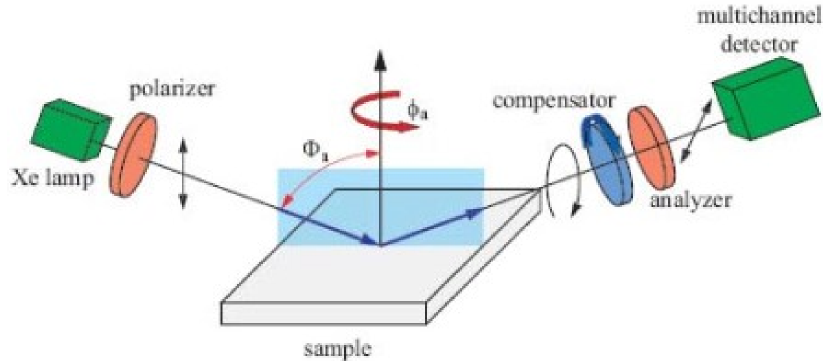

Figure 10. Rotating-compensator ellipsometer (RCE).

RCE configuration (Figure 10) can distinguish depolarized and polarized light. Depolarization of light occurs when the polarized light was subjected to some effects such as non-uniform film thickness, bandwidth, backside reflection, surface scattering.

2.6. Ex Situ Data Analysis Procedure

Ellipsometric measurements give the spectrum of two polarization angles (ψ, Δ) that depend on energy of the incident light. These experimental parameters can be easily transformed into pseudo-dielectric function as it is seen in chapter 2.4. By this transformation, pseudo-dielectric function gives only information about all of the sample but not about its layers. This superficial information requires being an optical model to characterize the optical properties of the sample. Even if the sample consists of only one layer or in other words, the sample is only a substrate the surface of the sample must be modeled in order to find real optical properties of the sample rather than pseudo optical function. Data analysis procedure is given in Figure 11.

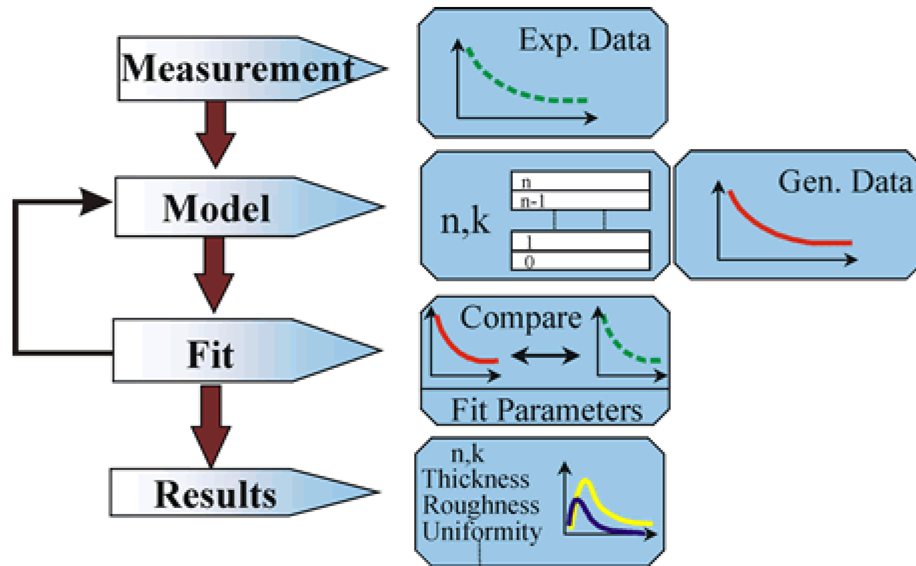

Figure 11. Ellipsometric data analysis flow chart [25].

Experimental data of the pseudo dielectric function of Si with a native oxide can be seen in Figure 12. First data analysis step is the construction of an optical model. The optical model for this sample includes a Si substrate and oxide layer (Figure 13). Optical constants of Si substrate (Figure 14a) and oxide layer (Figure 14b) are available in Woollam library [26]. In order to find the thickness of oxide layer a reasonable starting value is chosen to ease fitting process. This model, which is seen in Figure 13, provides estimation of (ψ, Δ) spectral data which is said as model data (Figure 15). This initial model data and experimental data are compared to see the degree of the fit (Figure 16). In this example only the thickness of the oxide layer is fit parameter so in fitting step oxide thickness value is obtained as result by some iteration which is controlled by SE software. If the result is not reasonable or mean squared error (MSE) is not sufficiently small then different optical model is constructed.

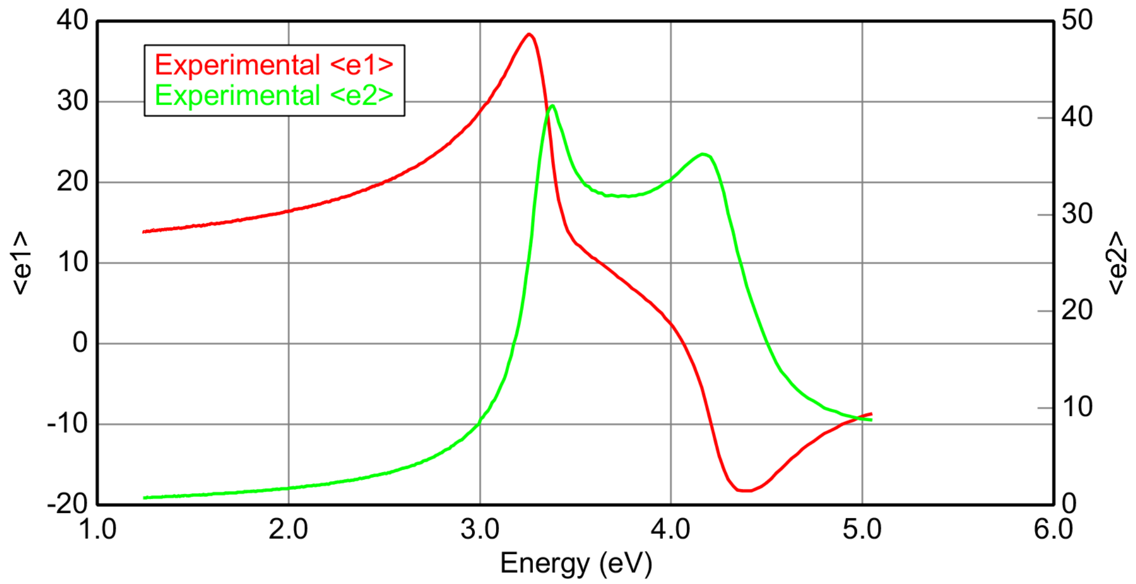

Figure 12. Experimental data of pseudo dielectric function of Si with a native oxide.

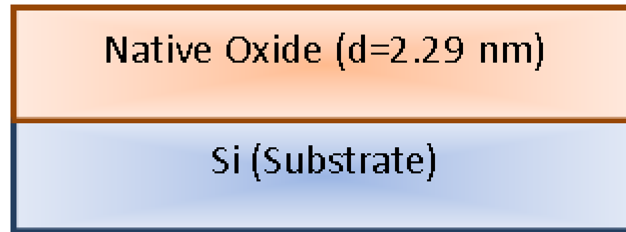

Figure 13. Si with native oxide model.

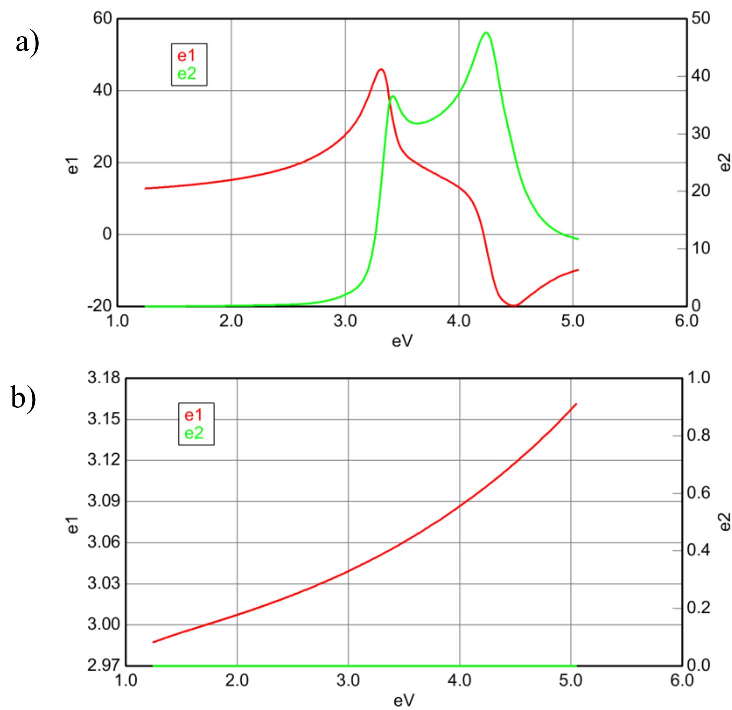

Figure 14. Optical constants of (a) Si and (b) oxide layer.

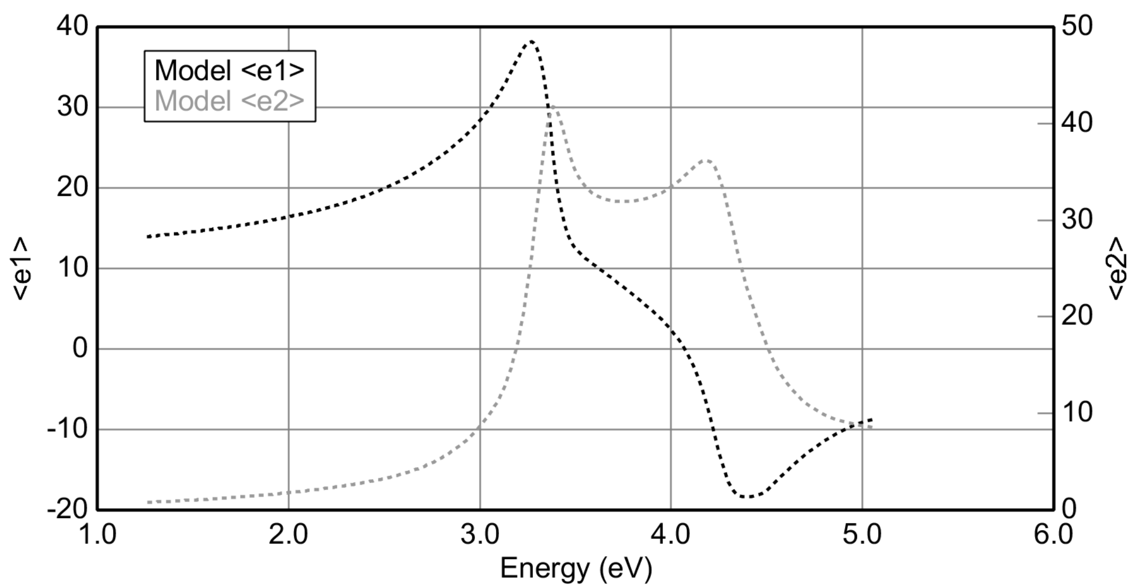

Figure 15. Model data for Si with native oxide sample.

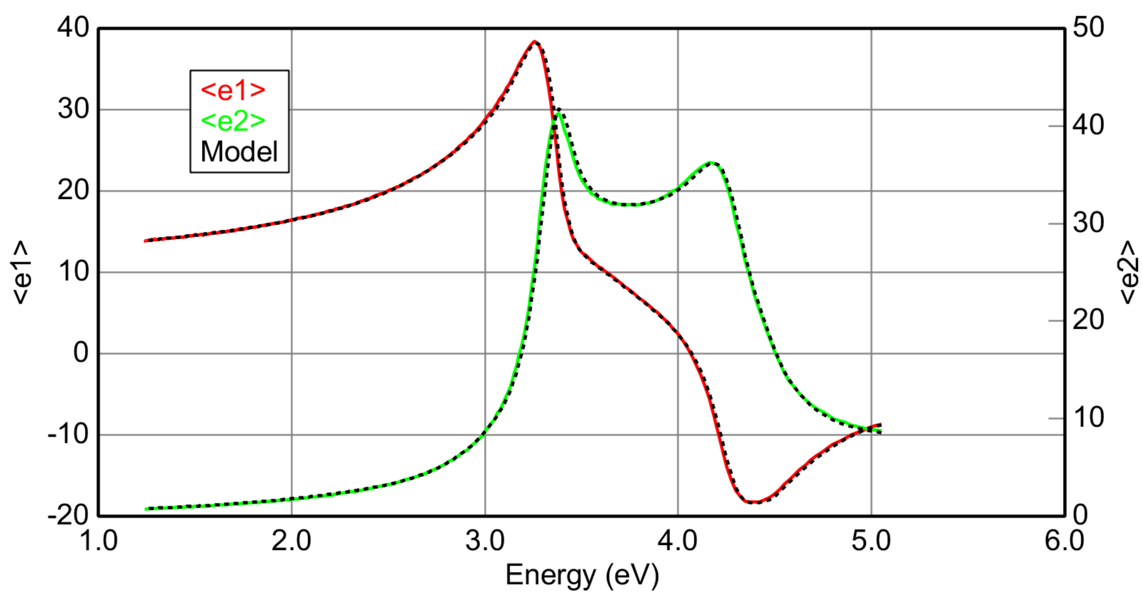

Figure 16. Experimental and model data for Si with native oxide.

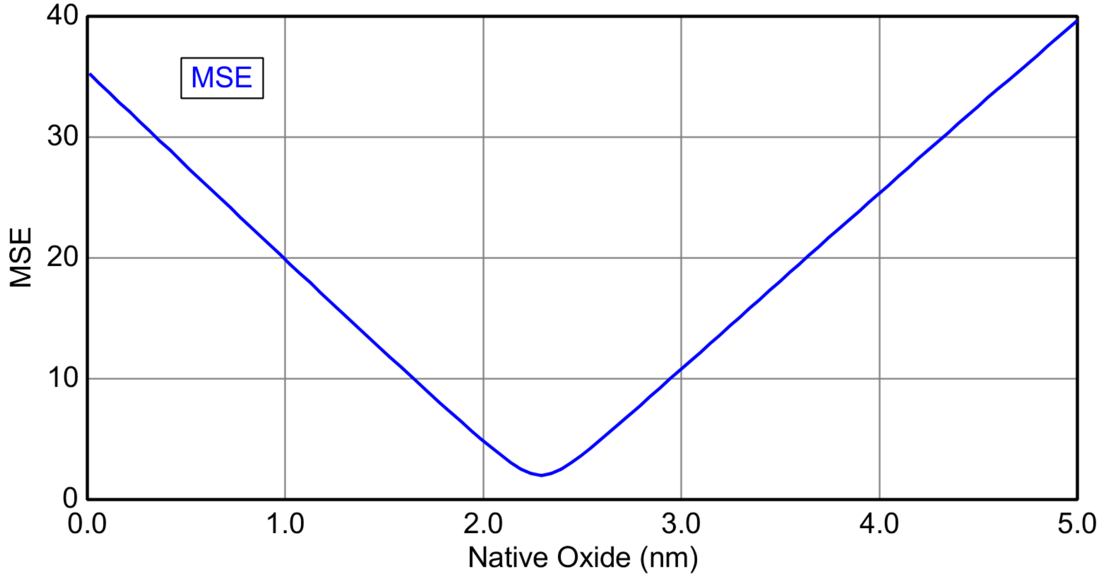

Figure 17. MSE versus native oxide thickness.

Mean squared error (MSE) is a quantity that provides to determine how experimental data and model agree with each other. Some cases may have a lot of unknown parameters such as the thickness of the layers and oscillator model parameters for dielectric function. If starting estimation values of these unknown parameters are not close enough to experimental values, then the iteration may finish at unreasonable values. Even if the MSE value is at local minimum for more reliable results it is necessary to estimate values well before starting to iterate so MSE will be at the global minimum (Figure 17). MSE can be expressed as follows to establish the error between experimental and model data in terms of polarization angles [13]:

$$MSE=\frac{1}{2n-m}\sum_{i=1}^{n}\left[\left(\frac{\psi_i^{mod}-\psi_i^{exp}}{\sigma_\psi}\right)^2+\left(\frac{\Delta_i^{mod}-\Delta_i^{exp}}{\sigma_\Delta}\right)^2\right] \qquad (2.24)$$

where n is the number of (ψ,Δ) data pairs versus photon energy, m is the number of unknown parameters determined in the data analysis, the subscript I indicates the given photon energy for $(\psi^{exp}, \Delta^{exp})$ and $(\psi^{mod}, \Delta^{mod})$ data pairs, σ_ψ and σ_Δ are standard deviations of experimental data for ψ and Δ, respectively.

In the Complete EASE software, which is provided with the system for the data analysis, MSE is described differently from previous equation. By this description, MSE does not directly depend on ψ and Δ, but it depends on N, C and S functions which are dependent on ψ and Δ parameters.

$$N = \cos(2\psi) \quad (2.25)$$

$$C = \sin(2\psi)\cos(\Delta) \quad (2.26)$$

$$S = \sin(2\psi)\sin(\Delta) \quad (2.27)$$

Therefore, MSE is written as follows where 'mod' and 'exp' indices for N,C and S functions refer to the dependency of experimental (ψ^{exp},Δ^{exp}) or model (ψ^{mod},Δ^{mod}) data. The subscript 'i' is used for the given photon energy.

$$MSE = \sqrt{\frac{1}{3n-m}\sum_{i=1}^{n}\left[\left(N_i^{mod}-N_i^{exp}\right)^2+\left(C_i^{mod}-C_i^{exp}\right)^2+\left(S_i^{mod}-S_i^{exp}\right)^2\right]} \times 1000 \quad (2.28)$$

where 'n' is the total number of different wavelength values of incident light and 'm' is the number of free fit parameters. The N, S and C parameters make the MSE value more suitable due to the fact that these parameters are always bounded between -1 and 1 for all values of ψ, Δ and the configuration of rotating compensator ellipsometer measures data with nearly the same accuracy in N, C and S. Thus N, C and S are elements of the isotropic Mueller Matrix.

The lower the MSE value, the better the agreement between model and experimental data is. The multiplicative factor 1000 in the MSE definition makes ideal MSE value as ~1 because accuracy is about 0.001 in experimental N, C and S parameters. For simple thin film structures MSE value is expected to be in 0.5-2 range, but for more complex film structures such as thick films or multiple layers, MSE values in the range of 10-20 may be acceptable.

Principally, MSE value is not enough for a reliable fit. It is necessary to test whether the model and the fit parameters have a physical meaning or not. For example, the optical constant fit results of $k<0$ or $n>10$ are unphysical and also zero or negative thickness values are not physically meaningful. Negative k values mean that light is not absorbed by material, but it is amplified so it is not physically possible. When k values are zero for a certain spectrum range, n values must increase smoothly with increasing photon energy.

2.7. Optical Model Construction

In the ellipsometric data analysis the dielectric function of layers of a sample is required. If dielectric function is not known for any of layers, it is necessary to model the dielectric function. There are many dielectric function models such as Lorentz model, Cauchy model, Sellmeier model, Tauc-Lorentz model, harmonic oscillator approximation (HOA), model dielectric function (MDF) and Drude model. In fact, all these models were derived from the Lorentz model.

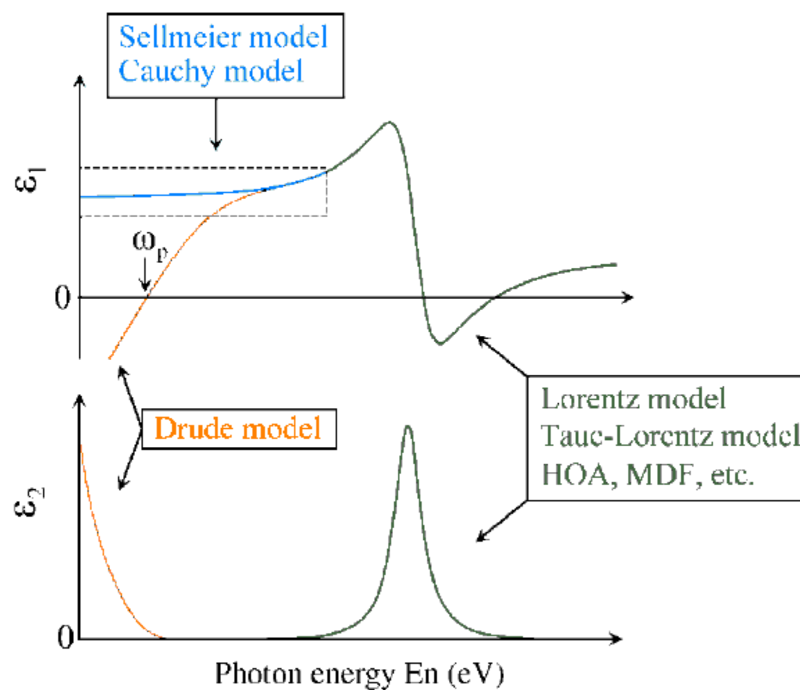

Figure 18. Dielectric function models used in ellipsometry [20].

If a material is transparent (k=0 or ε_2=0) for a certain region of the spectrum or for the all spectrum, Sellmeier or Cauchy models are used. If a material has free carriers such as free electrons in metals and free carriers in semiconductors due to free carrier absorption, Drude model is applied to determine the dielectric function of these materials. The general shape of dielectric functions of these models is demonstrated in Figure 18.

In the following sections Lorentz model, Cauchy model and other oscillator models will be explained.

2.7.1. Lorentz model

The Lorentz model assumes a classical model which includes the negatively charged electron oscillators in viscous fluid. The electron is bound to a positively charged nucleus with a spring and alternating electric field of the light is applied to the system and it causes a polarization.

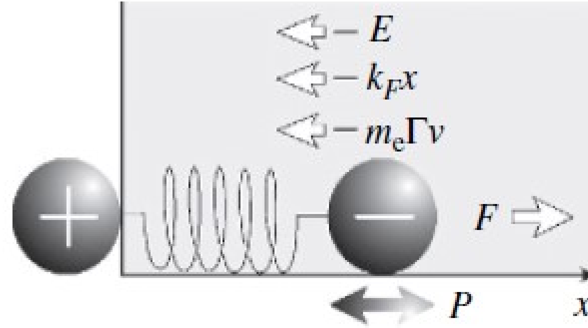

Figure 19. Classical Lorentz model [20].

According to Newton's second law the equation of the motion of the electron is written as

$$m_e \frac{d^2x}{dx^2} = -m_e\Gamma\frac{dx}{dt} - m_e\omega_o^2 x - eE_o \exp(i\omega t) \tag{2.29}$$

where $E_o\exp(i\omega t)$ is the alternative electric field of the light, m_e is the mass of the electron, e is the charge of the electron, ω_o is the resonant frequency of the spring ($\omega_o = \sqrt{k/m_e}$), Γ shows a proportional constant of the viscous force. The first term of the equation ($-m_e\Gamma\, dx/dt$) is viscous force of the viscous fluid. The term $-m_e\omega_o^2 x$ is comes from Hook's law (F=−kx), and the last term is electrostatic force (F=qE). The solution of this differential equation is,

$$x(t) = -\frac{eE_o}{m_e}\frac{1}{(\omega_o^2 - \omega^2) + i\Gamma\omega}\exp(i\omega t)\ . \tag{2.30}$$

Dielectric constant in terms of dielectric polarization written as,

$$\varepsilon = 1 + \frac{P}{\varepsilon_o E} \tag{2.31}$$

where P is the polarization term $P = -eN_e x(t)$ and E is the electric field $E = E_o \exp(i\omega t)$ so the equation rewritten as,

$$\varepsilon = 1 - \frac{eN_e x(t)}{\varepsilon_o E_o \exp(i\omega t)} \tag{2.32}$$

where N_e is the number of polarized electrons per unit volume so using the Lorentz model solution dielectric function becomes as,

$$\varepsilon = 1 + \frac{e^2 N_e}{\varepsilon_o m_e} \frac{1}{(\omega_o^2 - \omega^2) + i\Gamma\omega} . \tag{2.33}$$

As it is known that $\varepsilon = \varepsilon_1 - i\varepsilon_2$ so ε_1 and ε_2 are written as,

$$\varepsilon_1 = 1 + \frac{e^2 N_e}{\varepsilon_o m_e} \frac{(\omega_o^2 - \omega^2)}{(\omega_o^2 - \omega^2)^2 + \Gamma^2\omega^2}, \tag{2.34}$$

$$\varepsilon_2 = \frac{e^2 N_e}{\varepsilon_o m_e} \frac{\Gamma\omega}{(\omega_o^2 - \omega^2)^2 + \Gamma^2\omega^2}. \tag{2.35}$$

An example of dielectric function calculated from the Lorentz model is seen in Figure 20. The term Γ which is a proportional constant of the viscous force becomes the full width at half maximum (FWHM) for ε_2 and the term ω_o which is the resonant frequency of the spring in the Lorentz model becomes peak position value for ε_2 in other words ε_2 has a maximum value at ω_o. Essentially in ellipsometric measurements generally energy unit is used instead of frequency.

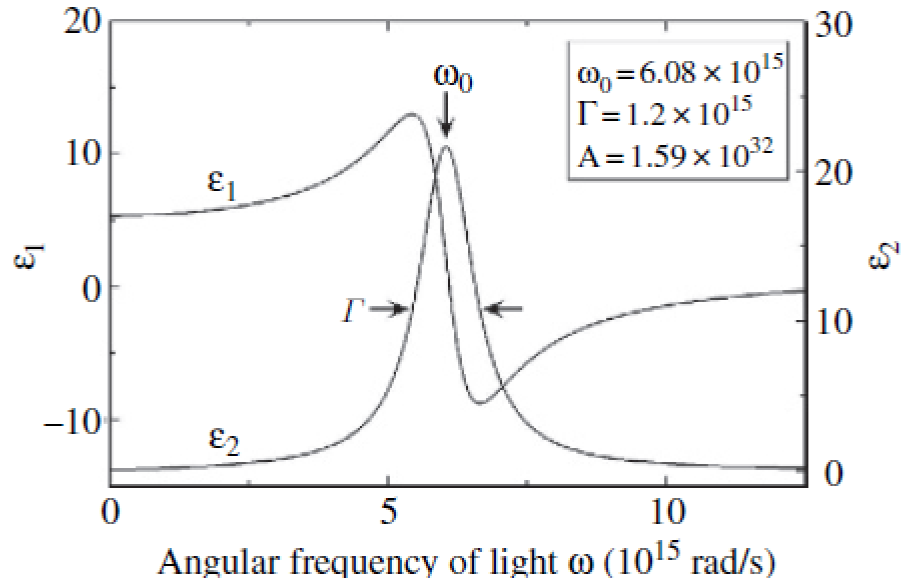

Figure 20. An example of dielectric function calculated from the Lorentz model [20].

In order to determine the dielectric function of sample it is required to use Lorentz oscillators more than one. If all oscillators that constitute dielectric function of the sample are Lorentz oscillators dielectric function of the sample in terms of photon energy is written as,

$$\varepsilon = 1 + \sum_{j} \frac{A_j}{E_{oj}^2 - E^2 + i\Gamma_j E} \tag{2.36}$$

where A is oscillator strength and j shows the jth oscillator that has the peak value at E_{oj} energy. The imaginary part of the dielectric function of GaAs in Woollam library used as reference material (black dashed line) and the new constructed GaAs model (green grayd line) with six Lorentz oscillators (grey solid curves) can be seen in Figure 21.

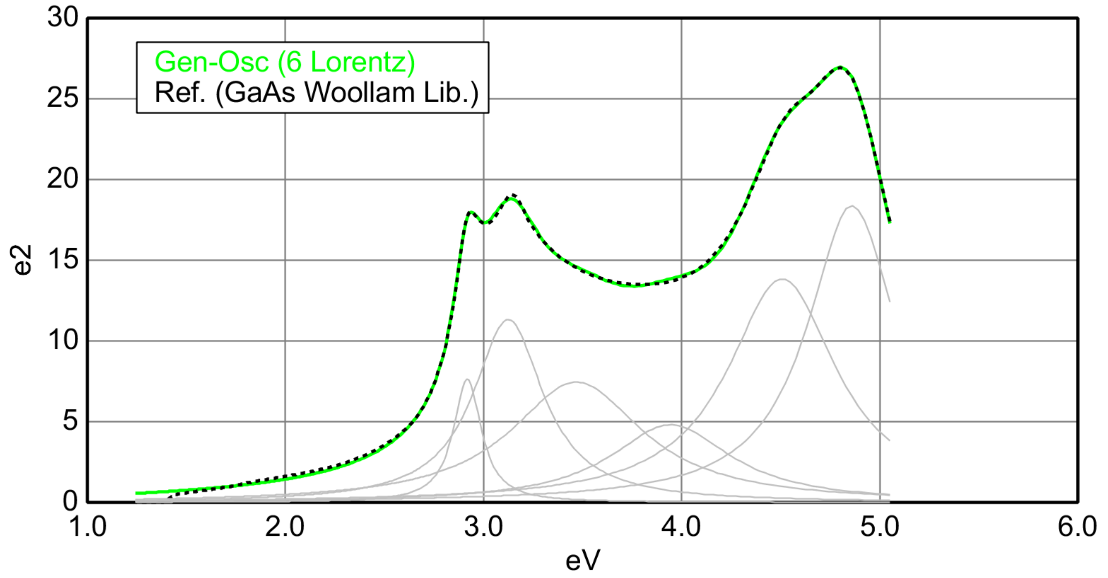

Figure 21. Imaginary part of the dielectric function of GaAs at Woollam library and Lorentz model with six oscillators.

2.7.2. Cauchy Model for Transparent Materials

For transparent materials $\varepsilon_2=0$ or k=0. In the Lorentz model when Γ goes to zero ($\Gamma\rightarrow 0$) and $\omega<<\omega_o$ so imaginary part of the dielectric function goes to zero ($\varepsilon_2=0$). By using $\omega=2\pi c/\lambda$ transformation equation (35) becomes $\varepsilon_2=0$ and equation (34) becomes,

$$\varepsilon_1 = n^2 = A + \sum_j \frac{B_j \lambda^2}{\lambda^2 - \lambda_{oj}^2} \tag{2.37}$$

This equation is called as the Sellmeier model. Cauchy model is derived from the series expansion of the Sellmeier model. Accordingly Cauchy model is,

$$\sqrt{\varepsilon_1} = n = A + \frac{B}{\lambda^2} + \frac{C}{\lambda^4} + \cdots \tag{2.38}$$

An example of the Cauchy model for transparent materials is shown in Figure 22.

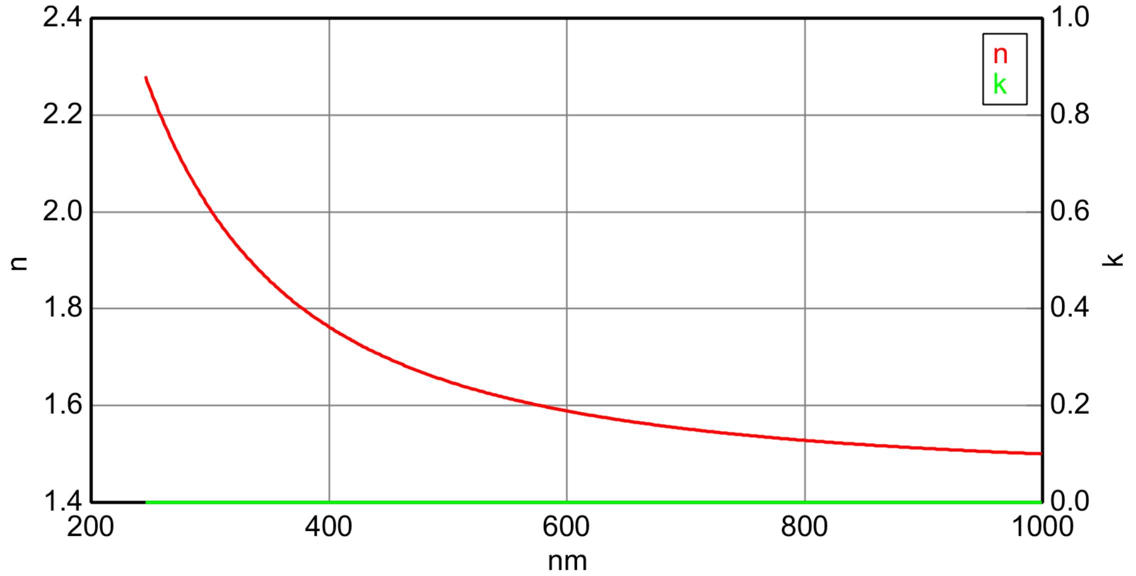

Figure 22. Optical constants versus wavelength according to Cauchy model with parameters A=1.45, B=0.05 and C=0.0.

2.7.3. General Oscillator Model for Semiconductors

In the software CompleteEASE that we used in the ellipsometric data analysis includes many oscillators for optical modeling called as general oscillators (Gen-Osc). In this chapter general information about these oscillators and their parameters will be given.

The classical Lorentz oscillator model has been given thoroughly in the previous section. Fit parameters for the Lorentz model are the amplitude of the oscillator (A_j) which is approximately equals to ε_2 at its peak value with no units, broadening parameter (Γ_j) which is the full width at half maximum value with energy unit, and peak position energy (E_{oj}). In CompleteEASE, Lorentz oscillators are given with $\varepsilon=\varepsilon_1+i\varepsilon_2$ description as,

$$\varepsilon_{Lorentz}=\frac{A_j\Gamma_j E_{oj}}{E_{oj}^2 - E^2 - i\Gamma_j E} \tag{2.39}$$

The harmonic oscillator function is also used in the determination of the dielectric function. Fit parameters for the harmonic oscillator model are the amplitude of the oscillator (A_j) which is approximately equals ε_2 at its peak value with no units, broadening parameter (Γ_j) which is the full width at half maximum with energy unit and

peak position energy (E_{oj}). Harmonic oscillator is equivalent to the Lorentz oscillator if the broadening parameter in harmonic oscillator is much less than the peak energy ($\Gamma_j \ll E_{oj}$). The comparison of harmonic and Lorentz equation is given in Figure 23. However, harmonic oscillator approximation (HOA) model is derived from quantum mechanical perturbation theory. Therefore the physical meaning of Γ becomes significant, and Γ corresponds to the average lifetime of electrons excited from the valance to the conduction band [27, 28]. The treatment of this model is similar to quantum mechanical single electron transitions. The equation of the harmonic oscillator is,

$$\varepsilon_{Harmonic} = \frac{A_j \Gamma_j}{2} \left(\frac{1}{E_{oj} - E - i\frac{\Gamma_j}{2}} + \frac{1}{E_{oj} + E - i\frac{\Gamma_j}{2}} \right) \tag{2.40}$$

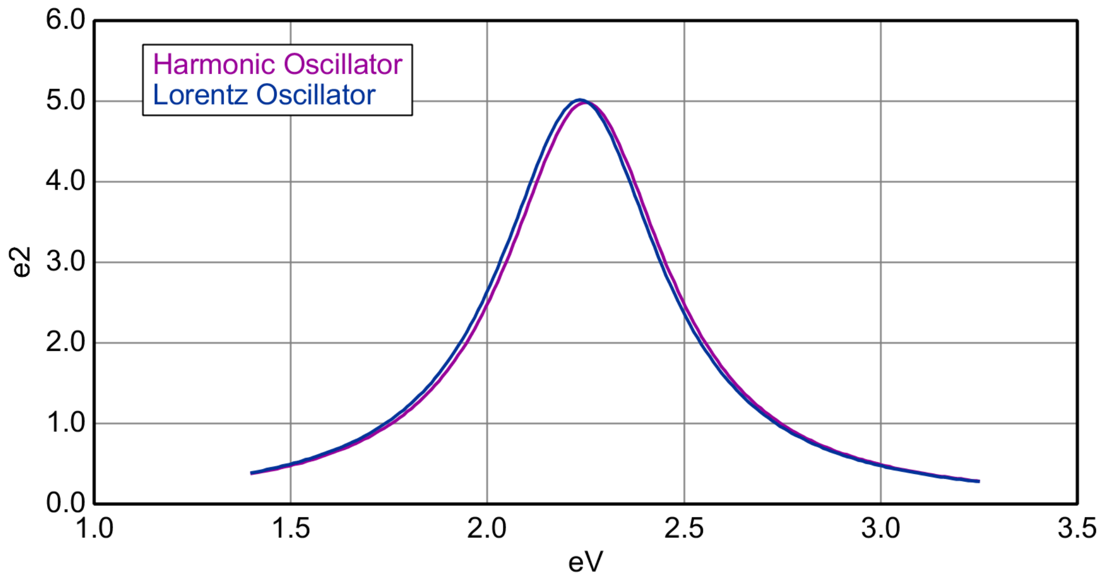

Figure 23. Harmonic and Lorentz oscillator model with same parameter values. (A_j=5, Γ_j=0.5 eV, E_{oj}=2.25 eV).

Gaussian oscillator is another type of oscillator which includes three fit parameters (Aj, Γj, Eoj) same as Lorentz and harmonic oscillator. In the Gaussian oscillator model Kramer-Kronig consistency between ε_1 and ε_2 is used. Real and imaginary parts of the dielectric function are interdependent via the Kramers-Kronig relations [29]. The comparison of Gaussian and Lorentz oscillator with the same parameter values is seen in Figure 24.

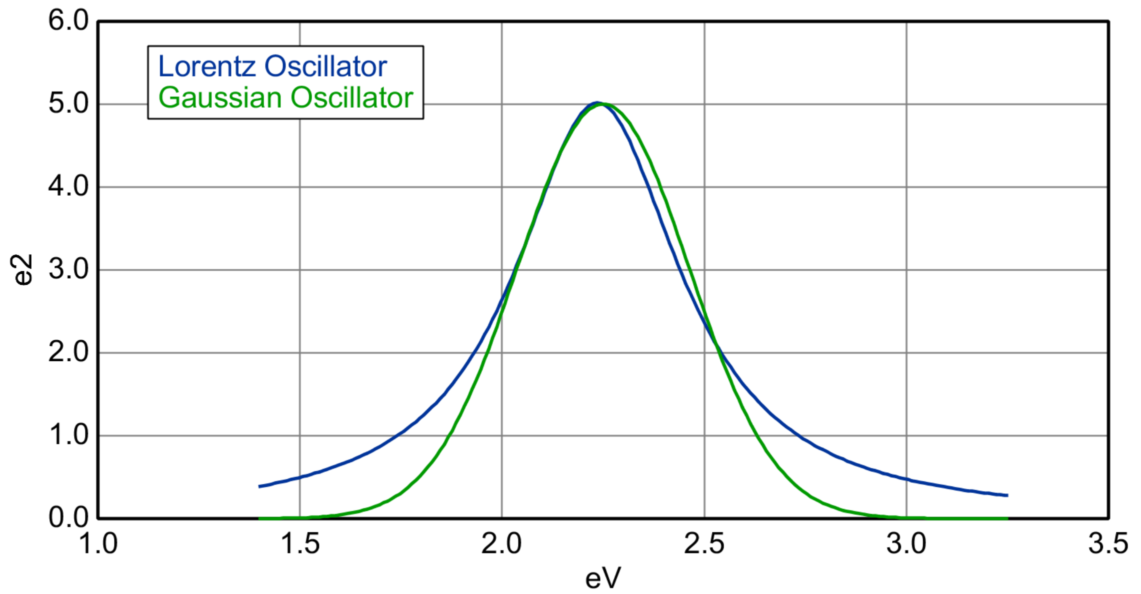

Figure 24. Gaussian and Lorentz oscillator model with same parameter values. (A_j=5, Γ_j=0.5 eV, E_{oj}=2.25 eV).

Psemi-tri oscillators are forms of the more general Herzinger-Johs Parametrized Semiconductor Oscillator [30] function. Psemi-tri oscillators have highly flexible shape and Kramers-Kronig consistency. As it is seen in Figure 25 seven parameters of the psemi-tri oscillator are A_j, AL_j, AR_j, Γ_j (or Br_j), Ec_j, WL_j and WR_j. Ec is the central energy parameter which is close to the energy of the peak position. For the different values of broadening parameter (Γ_j or Br_j) a comparison is seen in Figure 26 to demonstrate how the shape of the psemi-tri oscillator looks like.

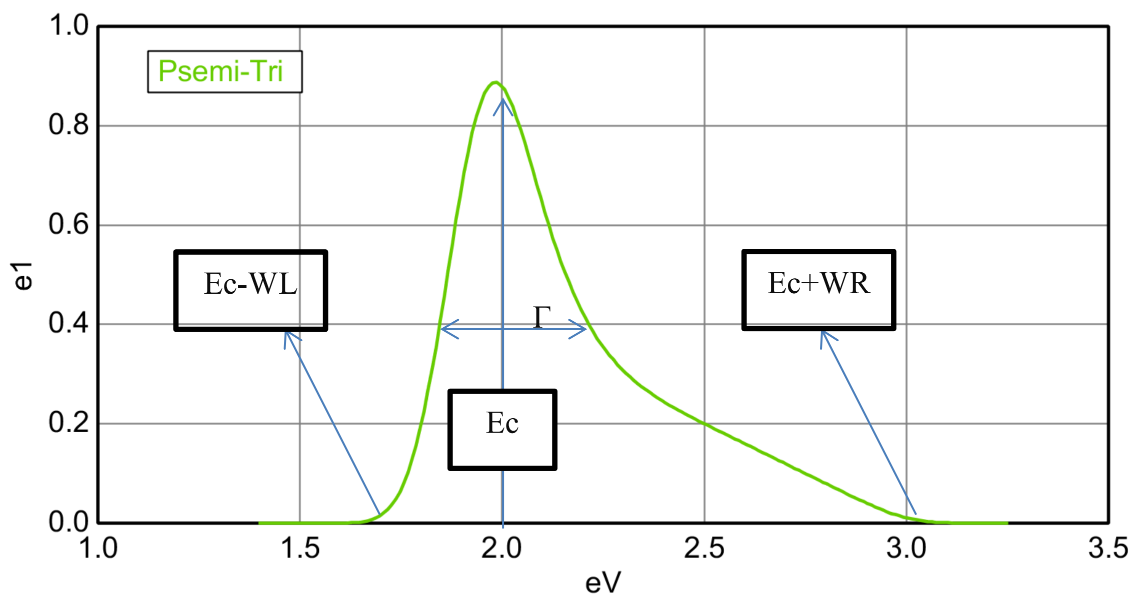

Figure 25. Psemi-tri oscillator.

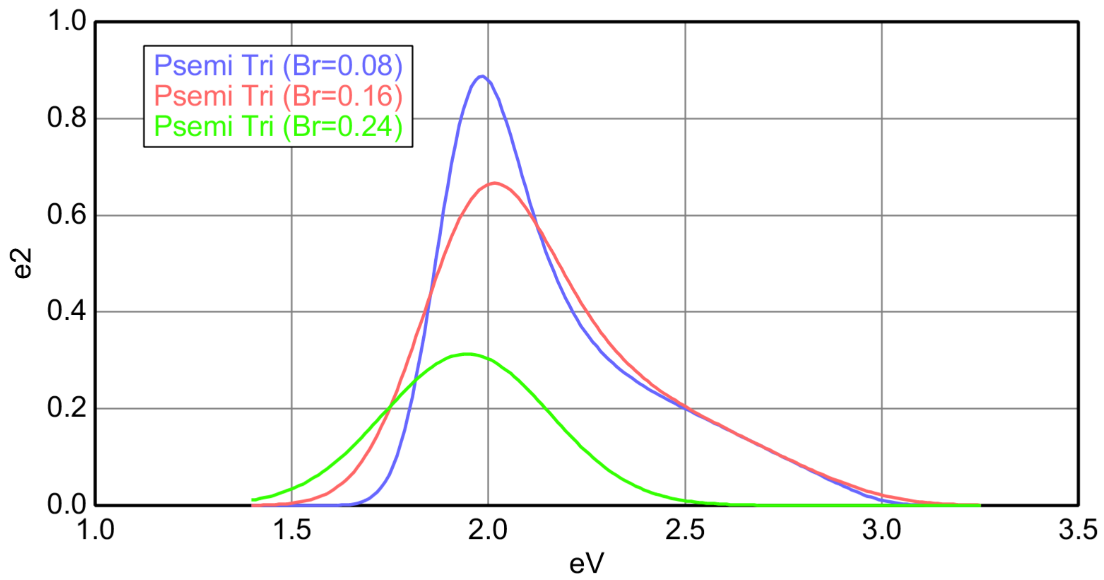

Figure 26. Psemi-Tri oscillators for three different values of broadening (Br or Γ) parameters. Other parameters are same for all oscillators (A_j=1, AL_j=0.75, AR_j=0.2, Ec_j=2 eV, WL_j=0.2 eV and WR_j=1 eV).

2.7.3.1. Band Structure and Critical Points

Spectroscopic ellipsometry (SE) is used to investigate the optical response of semiconductors and yields to find the spectral dependence of the dielectric function. Some critical points are seen in the real and imaginary parts of the dielectric function of the semiconductor. These critical points give information about the crystal structure and yield to determine composition of the ternary semiconductors (i.e. MCT, and CZT) or temperature of the crystal. In the Figure 27 imaginary part of the CdTe dielectric function and its critical points at 20 K, 208 K, and 294 K are demonstrated. Adachi *et al*. [31] studied the optical response of CdTe in the 1.1-5.6 eV photon-energy range at room temperature. The critical points for CdTe reveal at distinctive structures at the energies of the E_0, $E_{0+}\Delta$, E_l, $E_{1+}\Delta$, and E_2 in the spectral range of 1.1-5.6 eV [31] or at the energies of the E_0, $E_{0+}\Delta$, E_l, $E_{1+}\Delta$, E_2, and $E_2+\Delta$ in the spectral range of 1.5-6.0 eV [32]. Among these critical points E_0 corresponds to fundamental bandgap transition, E_l corresponds to strong transition due to quasi bound exciton, $E_{0+}\Delta$ and $E_{1+}\Delta$ correspond to weak transitions due to spin-orbit splitting, and E_2 corresponds to like a two dimensional transition at a saddle point [33]. The critical points for GaAs was also studied by Yao *et al* [34] in the range of 1.6-4.45 eV, the critical points of the GaAs

appears similarly as CdTe. Electronic band structure of CdTe at 0 K and critical band transitions are shown in Figure 28.

Figure 27. Imaginary part of the CdTe dielectric function at 20 K (solid line), 208 K (dot and dashed line), and 294 K (dashed line) [33].

Figure 28. Electronic band structure of CdTe at 0 K calculated with the empirical pseudo-potential method [35].

Dielectric function determination of GaAs by HOA was studied by Erman *et al.* with seven harmonic oscillator [36]. But it can be said that the harmonic oscillators do not correspond to the critical points of GaAs exactly [37]. It means that each critical point of harmonic oscillators used in the model cannot describe the joint density of states accurately. For this reason Adachi proposed model dielectric function (MDF) by using more distinct quantum calculations [38, 39]. Optical transitions of the band structure are calculated differently for each critical point. Another analysis to determine

the critical points is critical point (CP) analysis. CP analysis is performed by using the derivation of dielectric function [40, 41].

2.7.4. Effective Medium Approximation

The effective medium approximation (EMA) allows one to determine the dielectric response of heterogeneous microstructures (e.g. surface roughness, alloy, and segregated mixture). If the dielectric functions of each constituent of the structure are separately known, EMA can be easily applied to the optical model. EMA is employed to describe surface or interface properties of the film, especially during growth (*in-situ* process) [42-47] or rarely after growth (*ex-situ*) [48]. EMA layer thickness is also important to determine surface roughness of the sample (Figure 29).

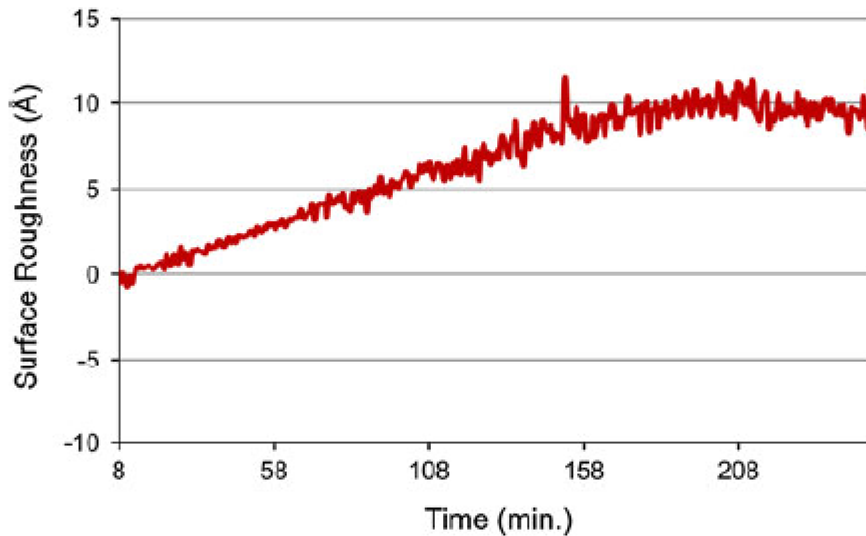

Figure 29. Evolution of EMA overlayer of CdTe during growth on GaAs [11].

Clausius-Mossotti relation [22] is the starting expression to derive EMA. The EMA model includes a spherical dielectric which consists of different dielectric materials (ε_1, ε_2...) and this spherical dielectric is surrounded by a host material (ε_h). But according to Bruggemen assumption ($\varepsilon=\varepsilon_h$) host material gives the desired dielectric properties of the effective medium. EMA for the material which has two material phases is written as,

$$f_1 \frac{\varepsilon_1-\varepsilon}{\varepsilon_1+2\varepsilon}+(1-f_1)\frac{\varepsilon_2-\varepsilon}{\varepsilon_2+2\varepsilon}=0 \tag{2.41}$$

where ε is the desired dielectric constant of the effective medium, ε_1, ε_2 are dielectric constant of different two materials which are required to be known and f_1 and f_2 are fractions of these two materials. Generally, these fractions are chosen as 50:50. But some cases different fractions are used. EMA is extended to describe a material consisting of many phases,

$$\sum_{i}^{n} f_i \frac{\varepsilon_i - \varepsilon}{\varepsilon_i + 2\varepsilon} = 0 \qquad (2.42)$$

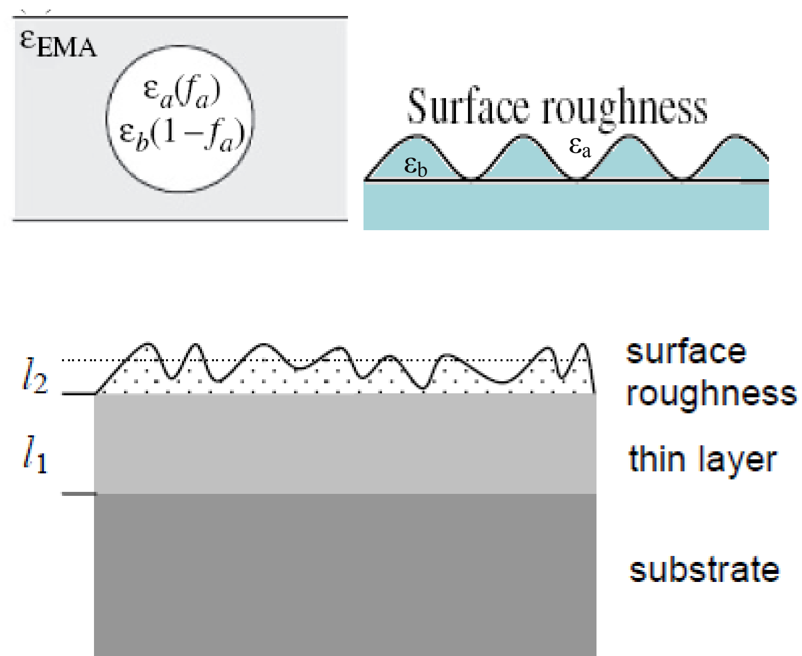

Figure 30. EMA and surface roughness.

CHAPTER 3

HGCDTE AND CDTE ON ALTERNATIVE SUBSTRATES

3.1. HgCdTe for IR detectors

CdTe is a semiconductor that formed from group II element cadmium and group VI element tellurium. In general, CdTe has a zinc-blend structure. CdTe is commonly used in infrared detectors or in solar cells [49-52]. CdTe can be alloyed with mercury to obtain the material HgCdTe for infrared (IR) detector applications. The composition of the Cd in $Hg_{1-x}Cd_xTe$ can be varied so as to adjust bandgap to intended IR spectral range.

In 1959, Lewson *et al.* [53] for the first time prepared the mixed crystals of HgTe-CdTe. HgCdTe (MCT) is an alloy of CdTe which is a semiconductor with bandgap of approximately 1.5 eV and HgTe which is a semi-metal with a negative bandgap of approximately -0.15 eV. Therefore the bandgap of HgCdTe is expected to be between these ranges (Figure 31). As the Cd content (x) increases in HgCdTe, the energy gap of HgCdTe increases almost linearly (Figure 32).

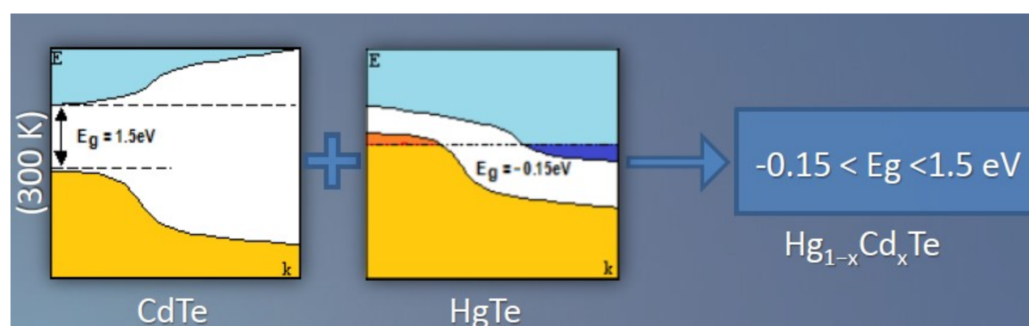

Figure 31. Energy band structures of CdTe and HgTe at room temperature and bandgap range for $Hg_{1-x}Cd_xTe$.

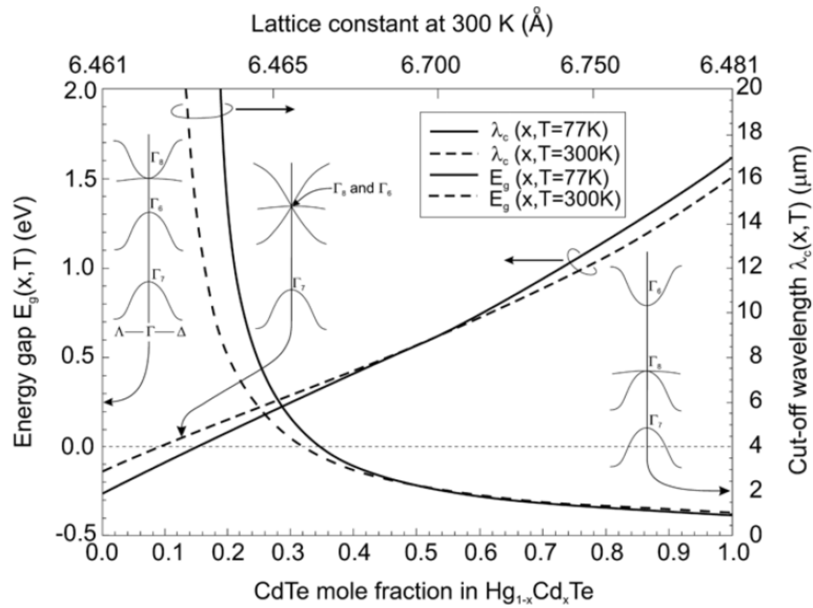

Figure 32. Energy gap of $Hg_{1-x}Cd_xTe$ versus Cd mole fraction near the Γ point.

The energy range between 0.0012-1.51eV corresponds to IR region. The wavelength range of the IR light spans from about 0.75 μm to 1000 μm or in energy unit IR spectrum spans from about 0.0012 eV to 1.7 eV. The Electromagnetic wave spectrum is seen in Figure 33.

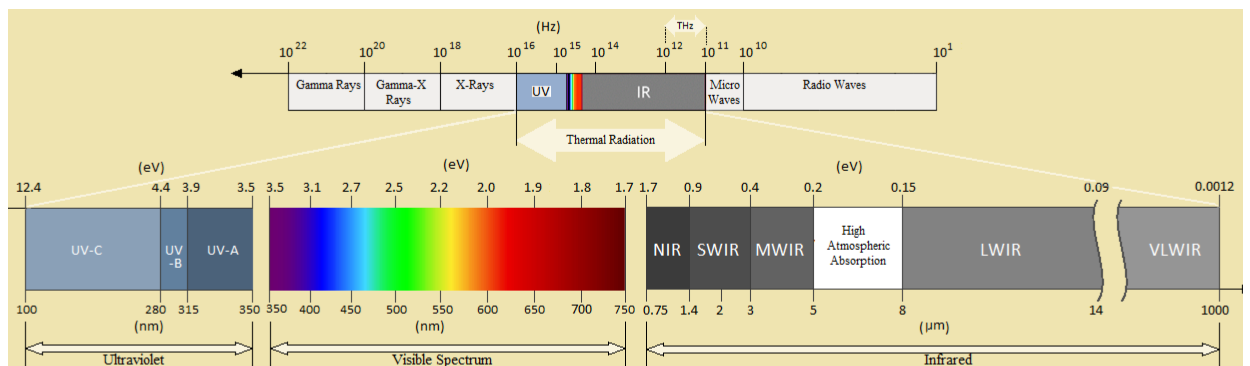

Figure 33. Electromagnetic wave spectrum.

Ternary alloy HgCdTe is a nearly ideal IR detector material that has an adjustable energy bandgap over the 1-30 μm range [54]. Because of the bandgap tunability of MCT, a detector which works in the intended range of IR region can be produced. In the IR detector applications detectors are classified as their detecting ranges which are small wavelength infrared (SWIR:1-2.7 μm), mid wavelength infrared (MWIR:3-5 μm), long wavelength infrared (LWIR:8-14 μm) and very long wavelength

infrared (VLWIR:14-30 μm). One can easily realize that there is a gap between 5 and 8 μm due to the atmospheric absorption. The molecules in the atmosphere such as H_2O and CO_2 absorb IR photons that have the same frequencies as vibration frequencies of these molecules. Therefore, these photons cannot reach to the detector so detection is failed. The transmission versus IR wavelength is seen in Figure 34.

HgCdTe crystals have a direct energy gap. High mobility of electrons and low dielectric constants that makes it preferable for photon detection. As the Cd composition changes the lattice constant of the HgCdTe remains nearly the same that makes HgCdTe to grow high quality layers and hetero-structures [1]. The disadvantage of HgCdTe is weak Hg-Te bond which results in surface and interface instabilities.

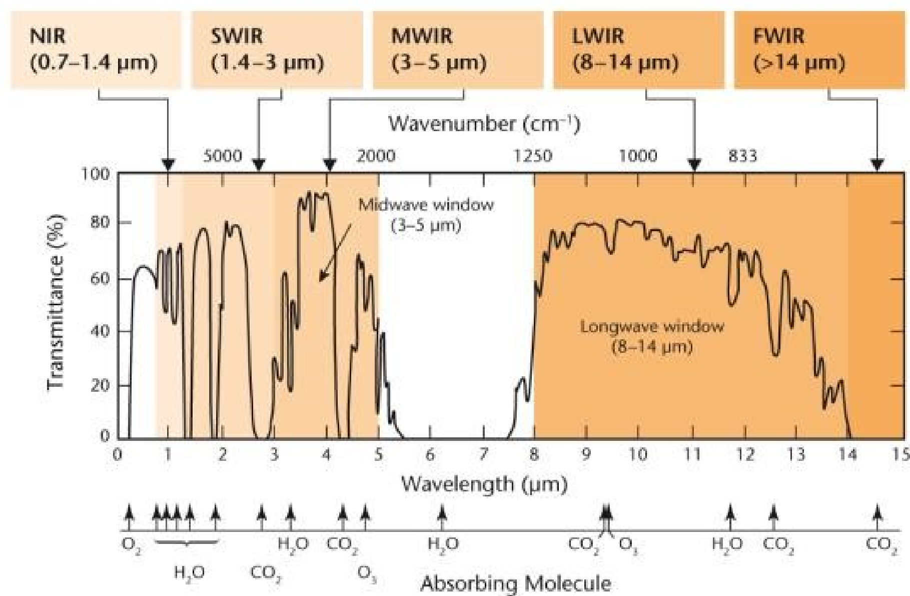

Figure 34. The atmospheric transmission versus IR wavelength.

Obtaining high crystal quality HgCdTe material on large area substrates, multi wavelength of IR detection, high resolution and more pixels per unit area are important issues for HgCdTe IR focal plane arrays (FPA). Some basic properties such as surface uniformity, reproducibility of some properties and detection efficiency are strongly affected by growth conditions. Therefore, optimal growth conditions are needed to be determined. One of the most important growth condition is the substrate temperature. In order to obtain optimal growth temperature, a temperature calibration using spectroscopic ellipsometry was studied by Vilela *et al* [55]. It is also important to grow high crystal quality CdTe buffer layer on a substrate such as GaAs or Si in order to obtain high crystal quality HgCdTe.

3.2. Alternative Substrates for HgCdTe Growth

HgCdTe growth over CdZnTe with 4% Zn composition substrates are preferred especially for LWIR window due to very low lattice mismatch and very low thermal expansion coefficient mismatch with HgCdTe. However, CdZnTe has some disadvantages like lack of uniformity in crystallinity and Zn distribution on large area substrates, high cost per unit area, and the low mechanical strength. Low cost and large area HgCdTe growth on CdZnTe is not possible because CdZnTe is very expensive and available only small size (49 cm^2) [56].

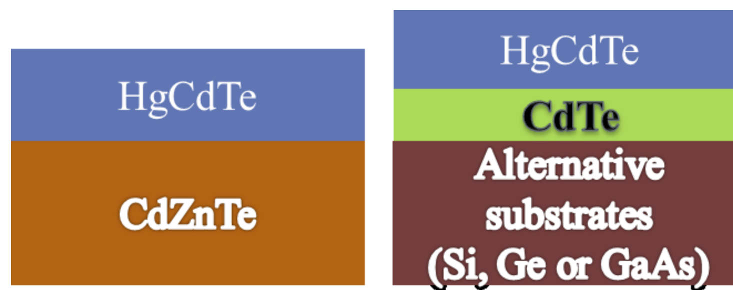

Figure 35. Substrates for HgCdTe growth

Fabrication of uniform defect free CdZnTe is not so successful, compared to substrates such as Si and Ge. For this reason, large area and lower cost alternative substrates have been used with CdTe buffer layer for the growth of HgCdTe (Figure 35). Nevertheless, the alternative substrates such as Si, Ge and GaAs have very large lattice mismatches with HgCdTe. Lattice mismatch between HgCdTe and Si, Ge and GaAs are 19%, 14.6% and 14.6% respectively (Table 1). Since lattice mismatch between CdTe and HgCdTe is lower than 1%, HgCdTe and alternative substrates can be compared for lattice mismatch and this lattice mismatch is primarily responsible for lattice defects on HgCdTe. These defects reduce device performance.

In Table 1, four substrate materials and their some properties for HgCdTe growth were given. The alternative substrates have more advantages over CdZnTe in terms of cost and available size. GaAs and Ge have lower lattice mismatch and thermal expansion mismatch with HgCdTe than Si does. Furthermore, the structure of GaAs is zinc blend which provides As rich polar surface (GaAs(211)B) on which the uniform CdTe(211)B (Te rich) surface may be directly accomplished [56].

Table 1. Comparison of substrates for HgCdTe/CdTe growth (Adapted from [56]).

Substrate	**Cost ($/cm^2)**	**Max available size (cm^2)**	**Lattice parameter (Å)**	**Lattice Mismatch with HgCdTe**	**Thermal misfit with HgCdTe**
CdZnTe	~350	~50	6.48	-	-
Si	~1	~700	5.43	19.3%	-92.3%
Ge	~8	~180	5.66	14.6%	13.8%
GaAs	~2.5	~180	5.65	14.6%	13.8%

InSb is another alternative substrate for growth of CdTe buffer layer. As it can be seen from the Figure 36 that lattice constant of InSb is very close to CdTe. However, InSb have low melting point (527 ^{o}C) [57] that causes some difficulties for the growth of HgCdTe layer [58]. Before growth, to remove surface oxide at high temperatures (usually higher than melting temperature of InSb) required, so the surface preparation process causes considerable damage on InSb surface that also negatively affects the growth of HgCdTe epilayer [59].

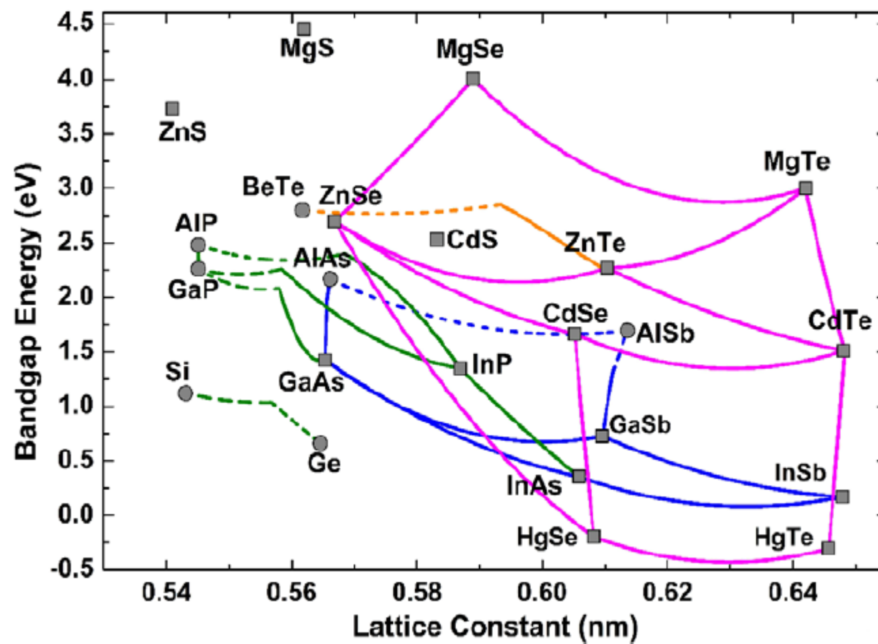

Figure 36. Energy gap versus lattice parameter for several materials [60].

3.3. HgCdTe and CdTe Growth

In order to grow high quality crystal HgCdTe or CdTe buffer layer, generally three methods are used: liquid phase epitaxy (LPE) [61], metalorganic chemical vapor deposition (MOCVD) [62] and molecular beam epitaxy (MBE) [63].The two methods LPE and MOCVD have higher growth rates than MBE and higher p-type doping levels can be obtained by LPE which is a challenge for MBE. But MBE technique has more primary advantages than the other techniques. Some of the most important advantages of MBE are ability to grow multiple layer structures such as p-n heterojunctions and superlattices, run to run flexibility, growth rates of about a few microns per hour allowing the atomically smooth surface, the ability to control the sample temperature and the process chamber under ultra-high vacuum (10^{-9}-10^{-11} Torr). The CdTe films given in this study were grown by a Gen-20MZ MBE system (Figure 37). The CdTe growth conditions will be discussed in chapter 5.

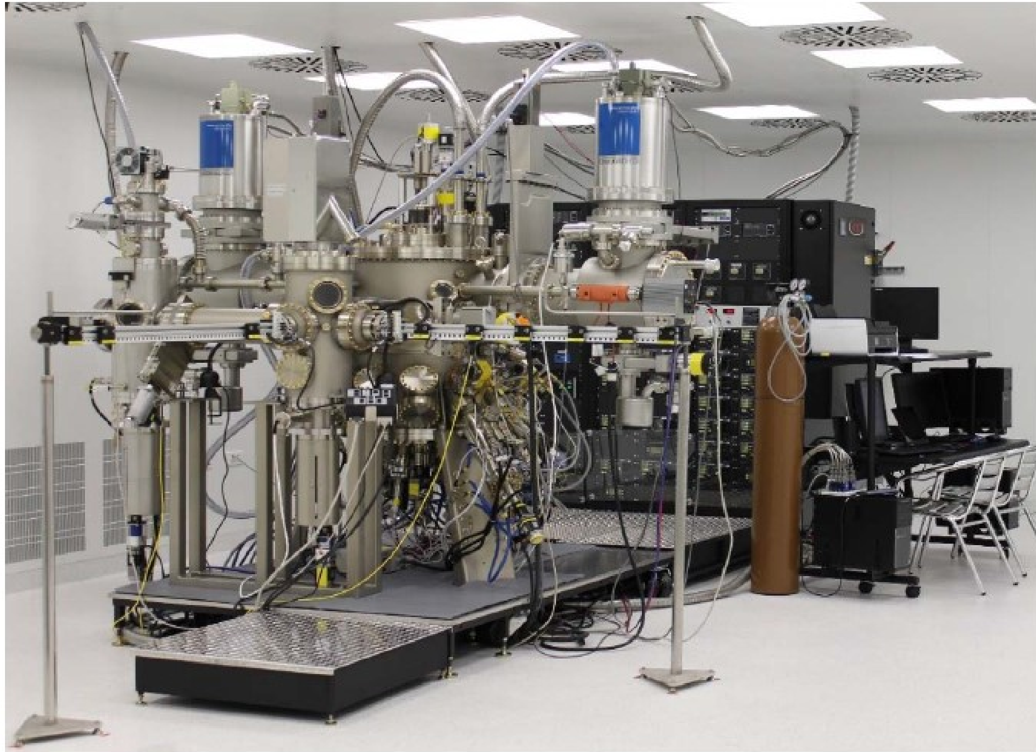

Figure 37. Gen-20MZ MBE system facility in the department of physics at Iztech.

CHAPTER 4

DIELECTRIC FUNCTION DETERMINATION

In order to analyze the SE data of the sample, it is required to construct an optical model. The optical model includes dielectric functions of each layer. In some cases the dielectric function of the known sample varies with the surface temperature, alloy composition or being crystal or amorphous. For this reason, it is also important to determine the dielectric function of the sample to obtain accurate results. In this section, dielectric function determination and selection of an optical model for a sample which was measured by spectroscopic ellipsometer will be demonstrated.

4.1. Woollam Library Model

The spectroscopic ellipsometry software library consists of the optical constants versus energy for various kinds of materials (i.e. dielectric materials, metals and semiconductors). Each material has certain properties and these properties may not be suitable for the sample under analysis which might have been produced by any method, especially due to the difference between the crystal qualities or surface roughnesses of the materials.

In this section, *ex-situ* SE characterization of a CdTe thin film on GaAs which was grown by MBE will be demonstrated by using only optical constant library available in the commercial software. The Cauchy material CdTe-oxide was used as a surface layer. The oxide layer is naturally formed over the CdTe film due to air exposure once it was taken out of the MBE chamber. If the ellipsometric characterization had been carried out during the growth process, which is called as *in situ* characterization process, EMA approximation for the surface layer would have been used [8]. However, in *ex-situ* SE data analysis, due to the formation of the oxide layer, EMA approximation becomes not useful, and in the analysis of the *ex-situ* SE data, generally oxide layer is used as the top layer. Because the dielectric function library provided with the software was used, the dielectric functions for each layer considered as known parameters and only the thickness values were obtained by this

model. In order to obtain the thickness, the ellipsometric data were fitted using a three-layer model; GaAs substrate, CdTe film, and a surface-oxide layer. Imaginary part and real part of the dielectric functions of these layers are seen in Figure 38, Figure 39 and Figure 40 for CdTe-oxide layer, CdTe layer and GaAs layer, respectively. Instead of using ε_1 and ε_2, e_1 and e_2 were used in the figures.

The Cauchy material parameters established in the library for CdTe-oxide are A=2.10, B=0.01 and C=0.00 (see chapter 2 for the assignment of these letters). The variation of the dielectric function of this material with energy is shown in Figure 38. As it is easily seen, CdTe-oxide material is a transparent material since e2 parameter is zero for all spectrum (e_2=2nk). It means that absorption coefficient is zero (hence, k=0) for all spectrum and there is no absorption.

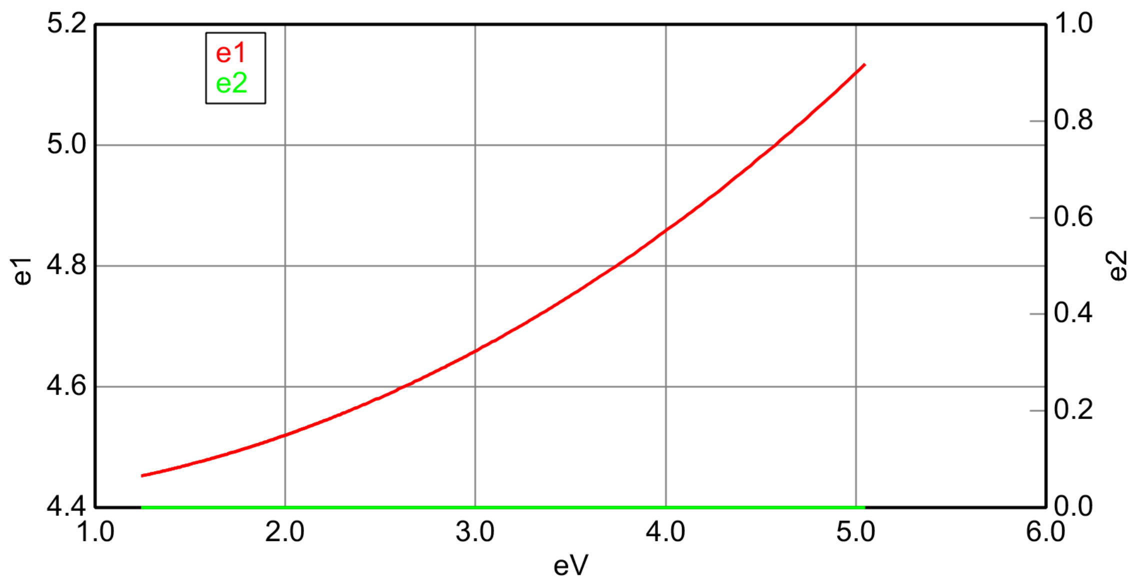

Figure 38. Imaginary (e2) and real (e1) part of the dielectric function of the CdTe Oxide Cauchy material in the Woollam library.

The dielectric function of the CdTe in the library is seen in Figure 39. This CdTe material was used in this model and has no adjustable fit parameters. The optical properties of this material may not fit to our molecular beam epitaxially grown sample, yet this model was used to find the approximate thickness of the CdTe and compare with the other models. The energy bandgap of the material in the library was easily determined by looking at the point where the imaginary part of the CdTe goes to zero or by looking at the real part where its first derivative becomes zero near the bandgap.

The energy bandgap of the CdTe in the library is 1.50 eV. The dielectric function behavior for the energies lower than the bandgap is like a Cauchy material.

Other critical points that were found by taking first derivatives of the imaginary part of the dielectric function are E_1=3.321 eV and $E_1+\Delta$ =3.866 eV. The two peaks of the imaginary part occur at these critical points.

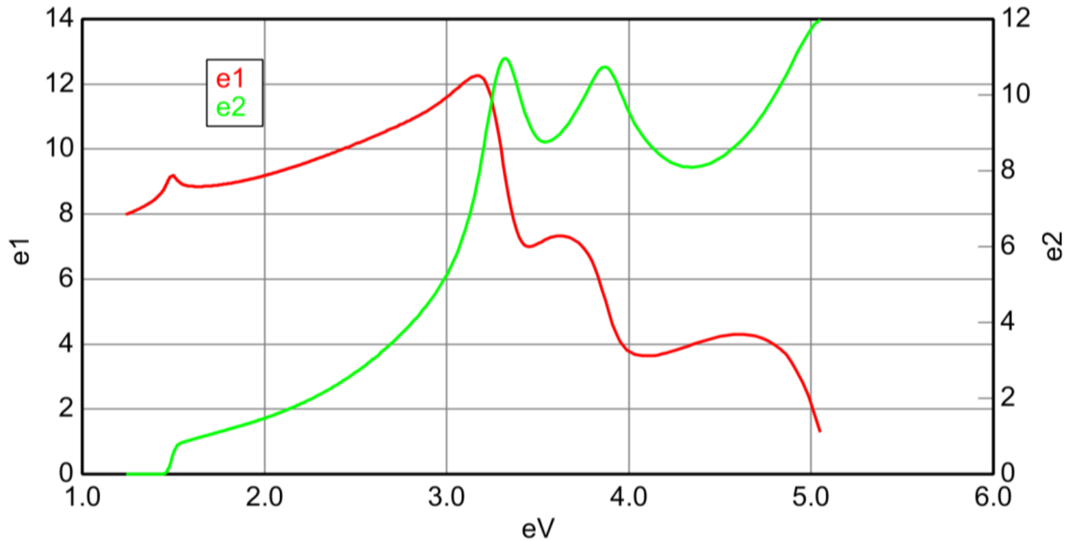

Figure 39. Imaginary and real part of the dielectric function of the CdTe material in Woollam library.

The dielectric function of the GaAs in the Woollam library is seen in Figure 40. The optical properties of this GaAs material are also fixed and do not have any fit parameter. The energy bandgap of the GaAs in the library is 1.422 eV. The critical points that were found by taking first derivatives of the imaginary part of the dielectric function are E_1=2.937 eV, $E_1+\Delta$ =3.143 eV, E'_0=3.801eV and E_2=4.797 eV.

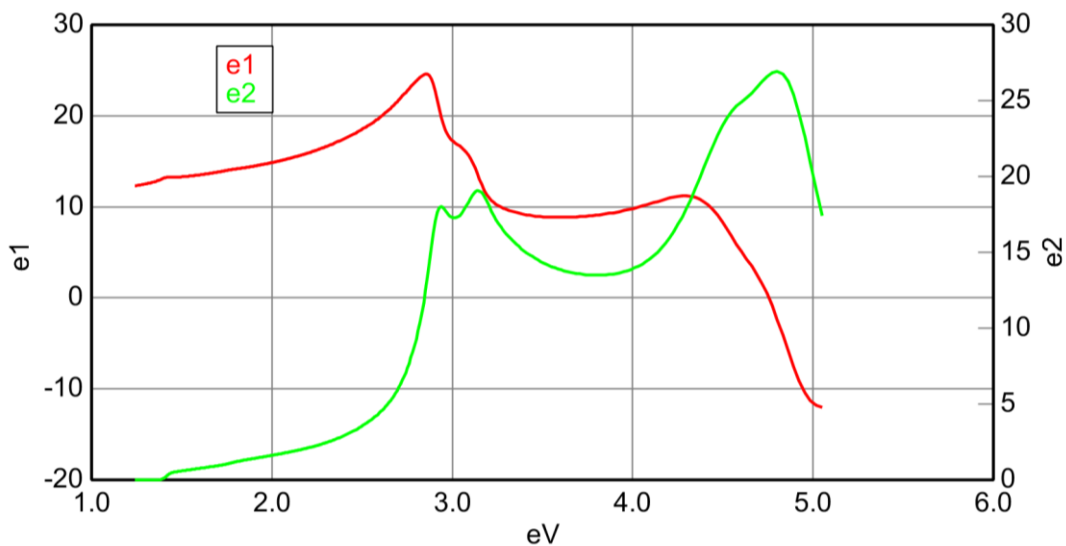

Figure 40. Imaginary and real part of the dielectric function of the GaAs material in Woollam library.

These critical points are important for semiconductors since these points give information about the band structure of the material. However, using fixed parameters in the optical model does not allow proper fitting of the measured samples as seen in Figure 41.

Experimental and model data of the pseudo-dielectric function of the CdTe on GaAs (sample CT7) are shown in Figure 41. Experimental real part of the pseudo-dielectric function is the red solid line and experimental imaginary part of the pseudo-dielectric function is the green solid line. Model data for pseudo-dielectric function is seen as the dashed black lines. MSE value was obtained from this analysis as 27,898. The fit parameters of this model, the CdTe thickness and the surface oxide thickness, were obtained as 1086.93 nm and 1.73 nm respectively (Figure 42). But these results are not precise since MSE value is very high.

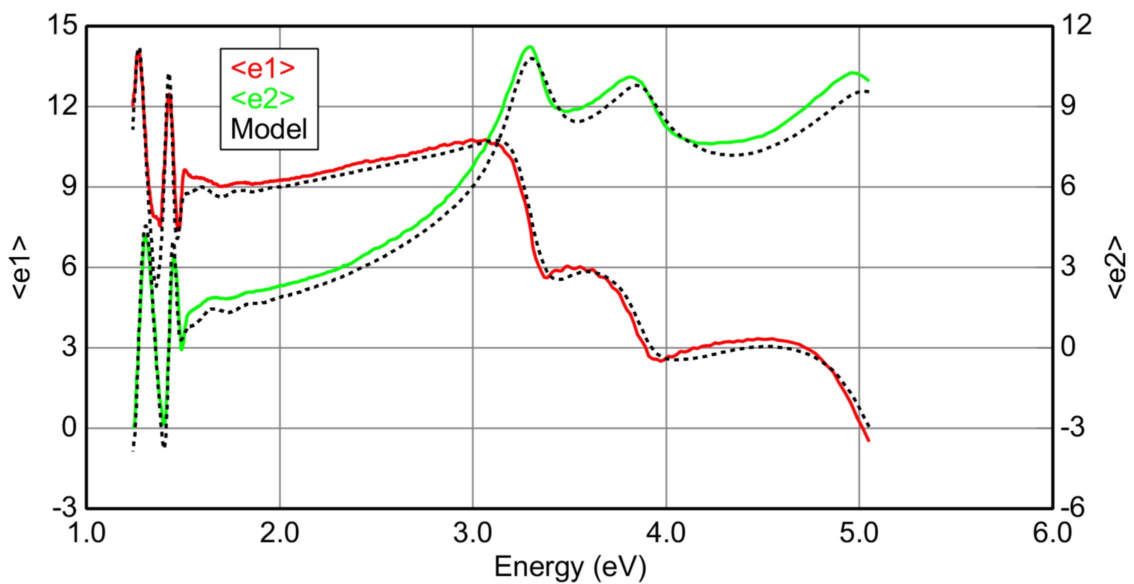

Figure 41. Experimental and Woollam model fit data of pseudo-dielectric function of the CdTe film on GaAs (Sample CT7).

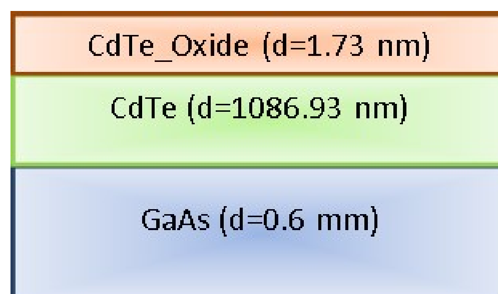

Figure 42. The optical model for CdTe on GaAs film by using Woollam library for each layer.

On the other hand, depolarization was also considered before fitting the experimental data. Depolarization generally occurs when the polarization of light deteriorates because of non-uniform film thickness, rough surface, inhomogeneous film or backside reflection from the substrate. These factors depolarizes the incident polarized light and the rate of depolarized light affects the ellipsometric data fitting [20, 64]. In a measurement high depolarization rate was seen in the low energy spectral region (Figure 43). The GaAs wafer that we used as substrate for CdTe growth was double side polished. It means that the backside reflection effects may cause high depolarization. The photons which have lower energy than the bandgap of GaAs can penetrate without being absorbed through the GaAs substrate. When these photons reach the backside of the GaAs wafer the photons are reflected due to the polished surface. For this reason, substrate backside correction was included to eliminate depolarization effects. By including this effect to the model, it was required to specify the thickness of the substrate. The thickness of GaAs wafer that we used was about 0.6 mm. This thickness was included in the model but was not a fit parameter. As it is seen in Figure 43 depolarization was fitted particularly by including backside reflection.

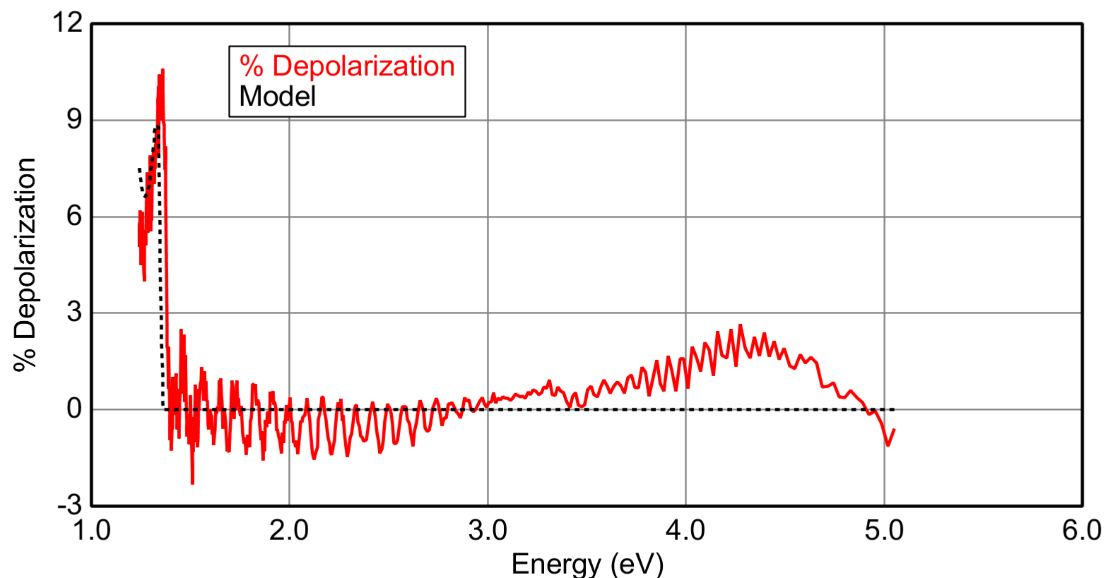

Figure 43. Depolarization data and model fit.

This modeling and fitting procedure only give us approximate thickness values of the film and surface oxide. Therefore, more reliable and useful modeling is required. In the following section, more reliable fitting results with acceptable MSE values will be given.

4.2. General Oscillator Model

In this section, the general oscillator model was used for the same sample (CT7). Woollam library was used for all layers in the previous section. In this model, general oscillator model was used for CdTe layer. The optical properties of the GaAs substrate and oxide layer were assumed to be known and acquired from Woollam dielectric function library. The CdTe film thickness, the oxide layer thickness and the optical properties of CdTe layer were unknown parameters in this model.

Three different oscillator models (five oscillator model, seven oscillator model and nine oscillator model) were used for sample CT7 in order to test the effects of oscillator amount on fitting results and MSE value. These oscillator models include three kinds of oscillators; psemi-tri oscillators, Gaussian oscillators and harmonic oscillators. As a reference material the imaginary part of the dielectric function of CdTe in the Woollam library was used and fitted by using these oscillators. The software uses Kramers-Kronig relation to find the real part of the dielectric function. Oscillator parameters labeled as fit parameters and then they were used in the construction of CdTe layer. Surface optical properties of the oxide layer and GaAs layer were chosen from Woollam library material in these models without using oscillators or without any fit parameters. Only thickness was a fit parameter for these layers.

In the five oscillator model, five psemi-tri oscillators were used to construct the dielectric function of the CdTe layer for molecular beam epitaxially grown CT7 sample. These oscillators can be seen in Figure 44. These selected psemi-tri oscillators nearly symmetric according to their central energy parameters (E_{ci}) even so E_c parameters does not exactly coincide with the peak values of the imaginary part of the dielectric function. For this reason critical points (or peak energies) were found by using first or second derivative of the e1 and e2 functions.

The critical points for the five oscillator model were found as, E_1=3.316 eV and $E_1+\Delta$ =3.826 eV by using first derivative of e2. But the critical point E_2 was outside the range of measurement which covered from 1.24 eV to 5.05 eV. The interesting point about determining the bandgap energy was that by using first derivative of e1 energy bandgap found as Eg=1.5092 eV and by using second derivative of e2 energy bandgap found as Eg=1.5074 eV. The arithmetic mean of two different values was also found as, Eg=1. 5083 eV.

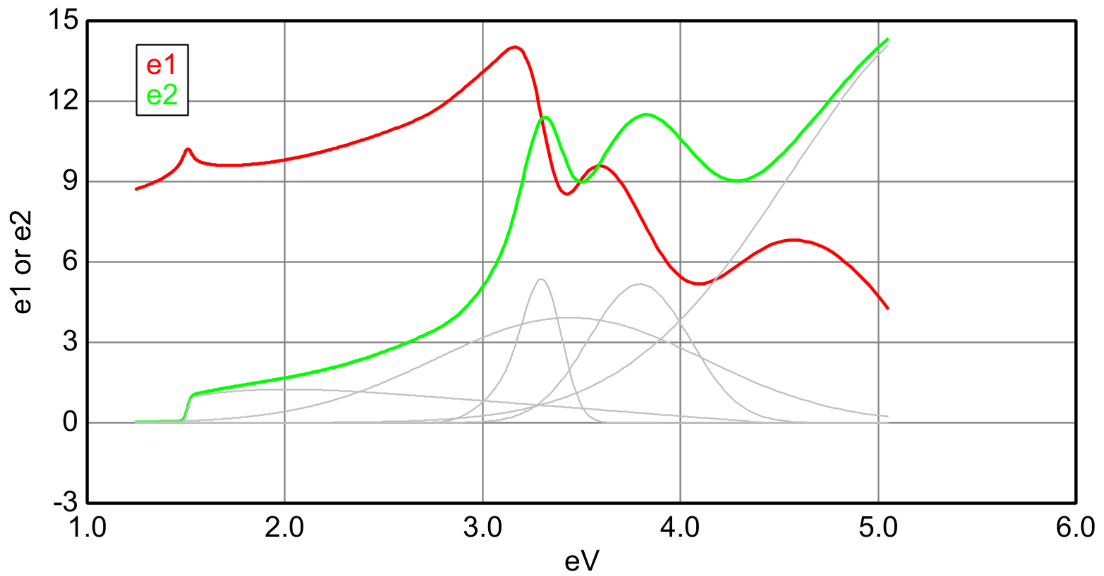

Figure 44. Imaginary and real part of the dielectric function of the CdTe material (Sample CT7) which was formed using 5 general oscillators

Fitting result of the experimental and model data of pseudo-dielectric function of the CT7 is seen in Figure 45. The values obtained from this model are MSE = 13.513, the thickness of CdTe layer = 1032.77 nm, and the thickness of the surface oxide layer = 3.25 nm (Figure 46). The MSE value was obtained lower than the previous model. The previous MSE was 27.898.

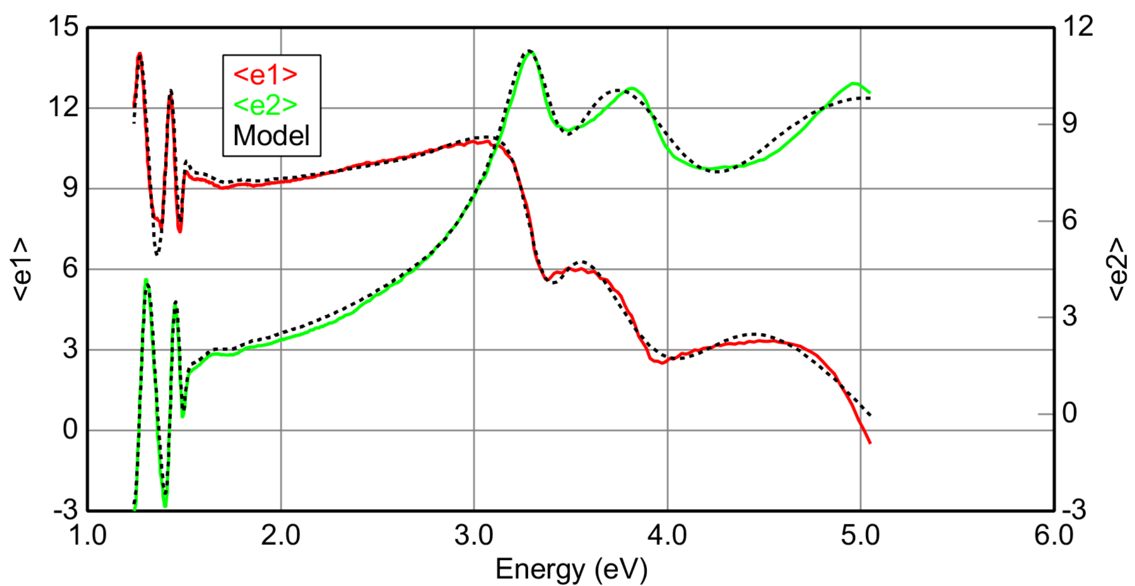

Figure 45. Experimental and 5 gen-osc model data of pseudo-dielectric function of the CdTe on GaAs film (Sample CT7).

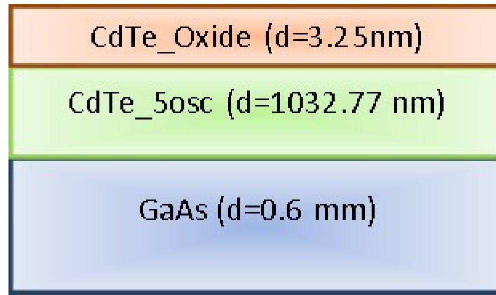

Figure 46. The optical model for CdTe on GaAs film by using 5 general oscillators for CdTe layer.

In the seven oscillator model four psemi-tri oscillators and three Gaussian oscillators were used to construct the dielectric function of the CdTe layer for the CT7 sample. These oscillators can be seen in Figure 47 except one of the Gaussian oscillator. This Gaussian oscillator that was used in the model cannot be seen and it is of no use. Some oscillator may disappear in the model such as this vanishing oscillator. Even if one may want to use more oscillator may not succeed. The selected psemi-tri oscillators are not symmetric according to their central energy parameters (E_{ci}) so Ec parameters cannot give the peak values of the imaginary part of the dielectric function. For this reason critical points (or peak energies) were found by using first or second derivative of the e1 and e2 functions.

The critical points for the seven oscillator model by using first derivative of e2 were found as, E_1=3.329 eV and $E_1+\Delta$ =3.819 eV. But the critical point E_2 could not found also due to the spectrum limitation. The central parameters of psemi-tri oscillators near these critical points were also found as Ec_1=3.338 eV and Ec_1 =3.961 eV.

The bandgap energy was found by using the first derivation of e1 and second derivation of e2 as E_g=1.5074 eV and E_g=1.5080 eV respectively. The arithmetic mean of the two different values was also found as, Eg=1.5077 eV. One of the Gaussian oscillators that has a peak value at 2.305 eV represents another critical of band transition $E_g+\Delta$. This value was also found as 2.312 eV by calculating the second derivative of e2.

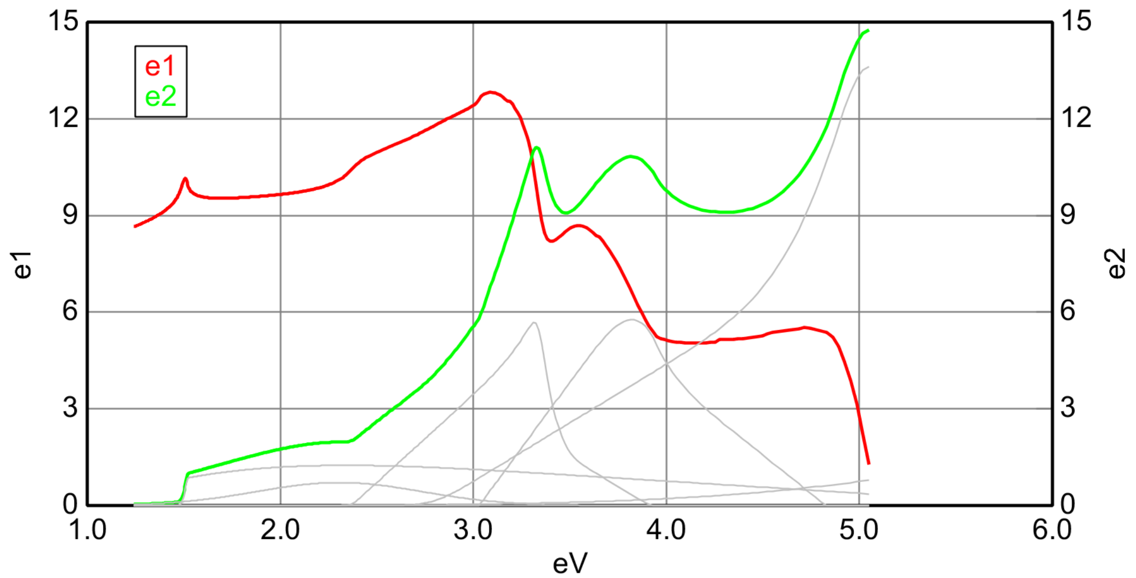

Figure 47. Imaginary and real part of the dielectric function of the CdTe material (Sample CT7) which was formed using 7 general oscillators.

Fitting result of the experimental and model data of pseudo-dielectric function of the CT7 is seen in Figure 48. The obtained MSE value of this model is 11.577 the thickness of CdTe layer is 1040.80 nm the thickness of the surface oxide layer is 2.64 nm (Figure 49). The MSE value obtained better than previous five oscillator model. The previous MSE was 13.513.

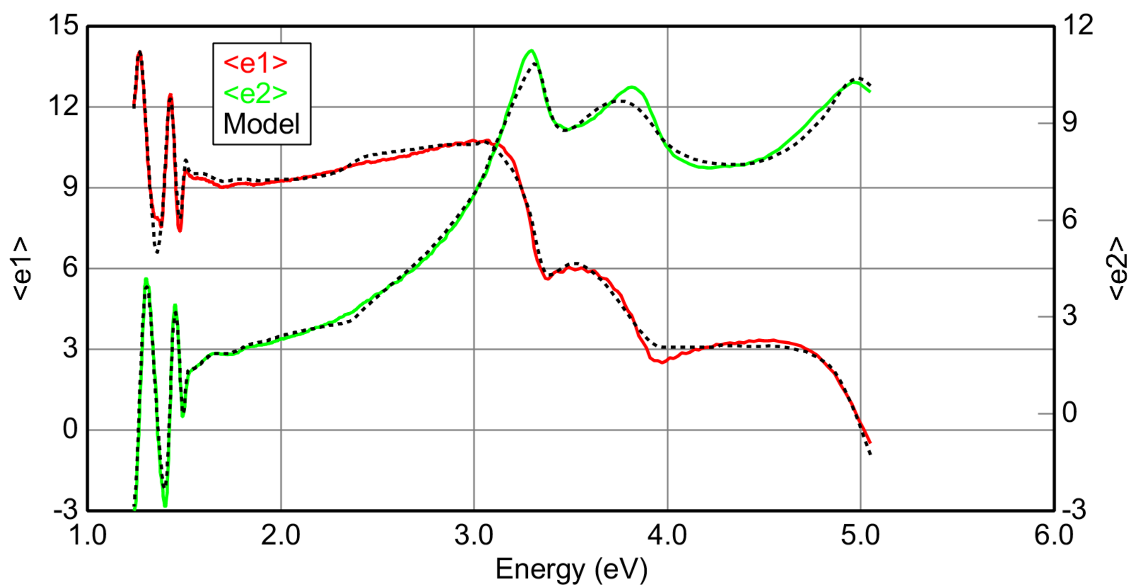

Figure 48. Experimental and 7 gen-osc model data of pseudo-dielectric function of the CdTe on GaAs film (Sample CT7).

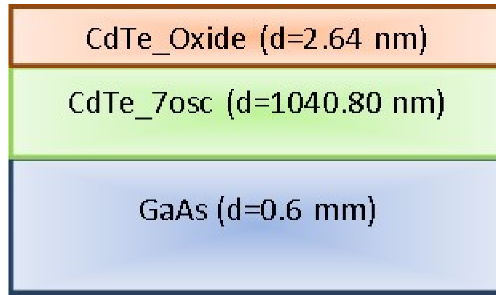

Figure 49. The optical model for CdTe on GaAs film by using 7 general oscillators for CdTe layer.

In the nine oscillator model six psemi-tri oscillators and three harmonic oscillators were used to construct the dielectric function of the CdTe layer for the CT7 sample. These oscillators can be seen in Figure 50. The selected psemi-tri oscillators have peak very close to their central energy parameters (E_{ci}). The critical points (or peak energies) were found by using first or second derivative of the e1 and e2 functions and they compared with the psemi-tri central energy points.

The critical points for the nine oscillator model by using first derivative of e2 were found as, E_1=3.312 eV, E_1+Δ =3.804 eV and E_2=5.015 eV. The central parameters of psemi-tri oscillators near these critical points were also found as Ec_1=3.338 eV and Ec_1 =3.961 eV.

The bandgap energy found by using the first derivation of e1 and second derivation of e2 as E_g=1.5073 eV and E_g=1.5056 eV respectively. The arithmetic mean of the two different values was also found as, Eg=1.5064 eV. One of the psemi-tri oscillators has a peak value at 2.460 eV that represents another critical point for band transition E_g+Δ. This oscillator indeed has central energy value at 2.484 eV but this value is not exactly at peak point.

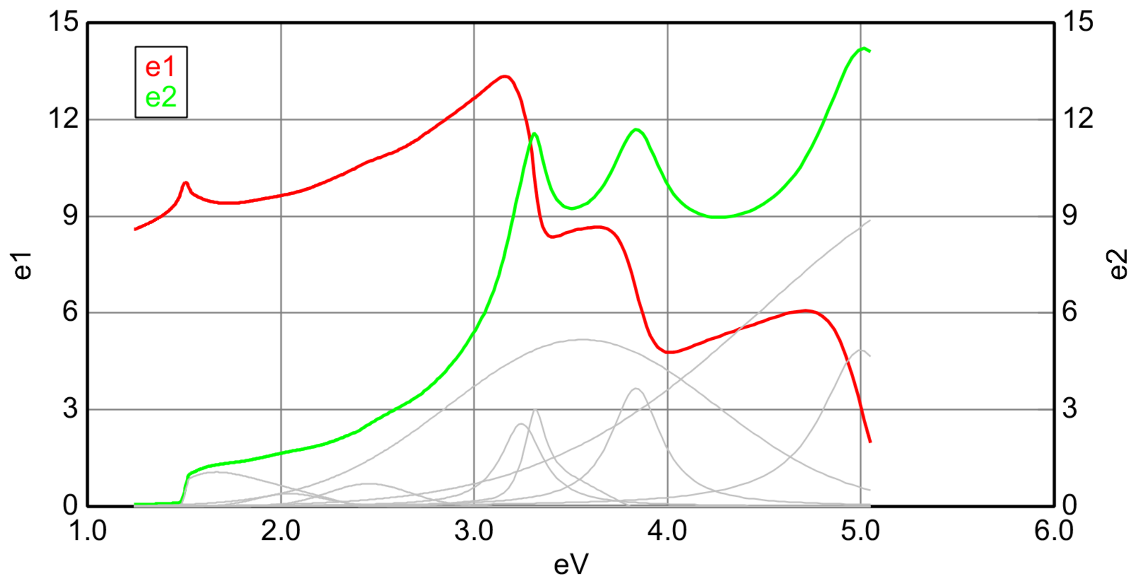

Figure 50. Imaginary and real part of the dielectric function of the CdTe material (Sample CT7) which was formed using 9 general oscillators.

Fitting result of the experimental and model data of pseudo-dielectric function of the CT7 is seen in Figure 51. The obtained MSE value of this model is 8.919, the thickness of CdTe layer is 1045.52 nm and the thickness of the surface oxide layer is 2.77 nm (Figure 52). The MSE value was obtained as better than previous seven oscillator model. The previous MSE was 11.577.

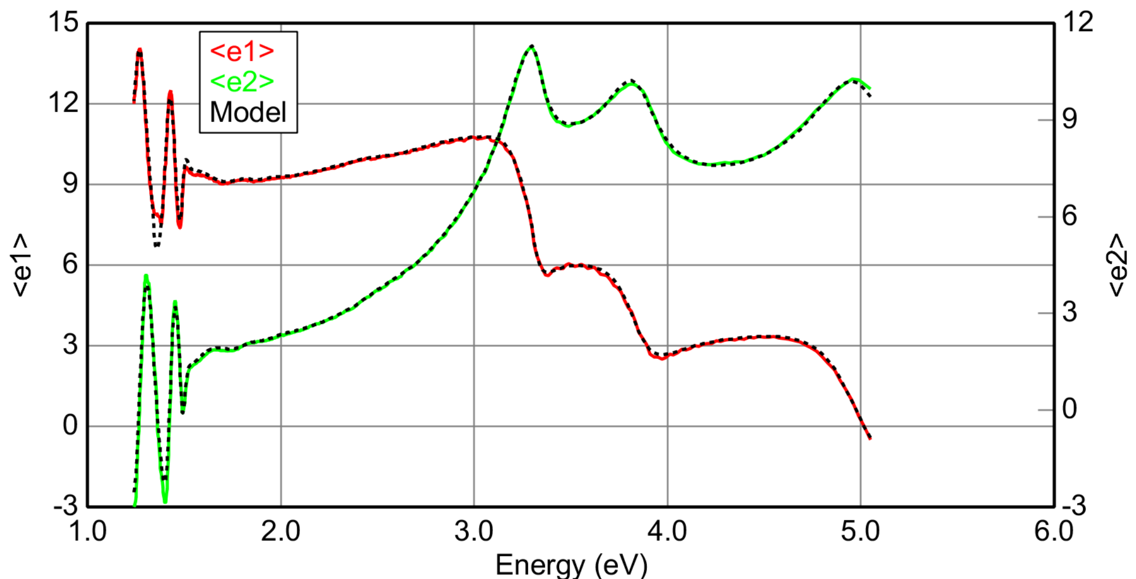

Figure 51. Experimental and 9 gen-osc model data of pseudo-dielectric function of the CdTe on GaAs film (Sample CT7).

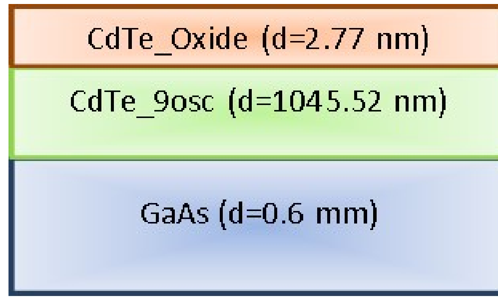

Figure 52. The optical model for CdTe on GaAs film by using 9 general oscillators for CdTe layer.

As it is seen in Figure 51 experimental and model data were in excellent agreement. In order to further improve this model, some additions were made. These three modified models were compared to the original 9 Gen-Osc Model in Table 2. The model with roughness did not yield an acceptable fitting due to the negative value of the surface roughness. Grading addition to the original model did not sufficiently decrease the MSE value. Roughness and grading addition to the model also did not provide any further improvement to the original model.

Table 2. Comparison of the three alternate models and 9 Gen-Osc model.

Parameter	**9 Gen-Osc Model**	**Roughness Addition**	**Grading Addition**	**Roughness &Grading Addition**
MSE	8.919	8.837	8.921	8.858
Roughness	N/A	-0.67 ± 0.430 nm	N/A	-0.54 ± 0.459 nm
Oxide Thickness	2.78 ± 0.115 nm	3.06 ± 0.254 nm	2.77 ± 0.159 nm	2.95 ± 0.282 nm
% Inhomogeneity	N/A	N/A	-0.02 ± 0.783	0.04 ± 0.785
CdTe Thickness	1045.52 ± 1.423 nm	1044.12 ± 1.659 nm	1045.49 ± 5.505 nm	1044.77 ± 5.526 nm

4.2.1. CdTe Band Structure and Critical Points

In this section, band structure properties and critical transitions of the CdTe (for sample CT7) will be analyzed by using the nine general oscillator model which yielded the best fit to the experimental measurements.

One of the psemi-tri oscillators and imaginary part of the dielectric function for the bandgap energy region is shown in Figure 53. The psemi-tri central parameter Ec and Ec-WL were demonstrated in the same figure. These points did not exactly give the correct value for the bandgap energy. Therefore, the real part of the dielectric function which has Kramers-Kronig consistency was examined. The peak position value of the real part of the dielectric function near the bandgap energy region can be seen in Figure 54. By taking the first derivative of e1, bandgap energy was found as 1.507 eV. On the other hand the bandgap energy determination was also performed by taking the second derivative of e2 spectrum and the bandgap energy was found as 1.506 eV. The difference between these two values for bandgap is not significant. Nevertheless only one of the derivation methods must be chosen to determine bandgap energy consistently.

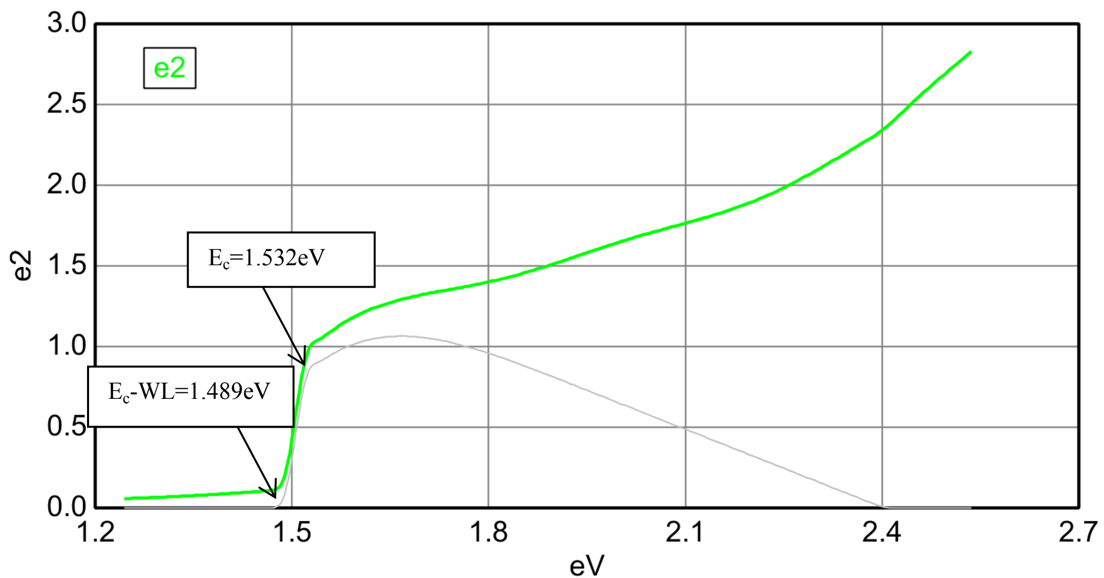

Figure 53. Imaginary part of dielectric function of CdTe near the bandgap and the psemi-tri oscillator (Sample CT7).

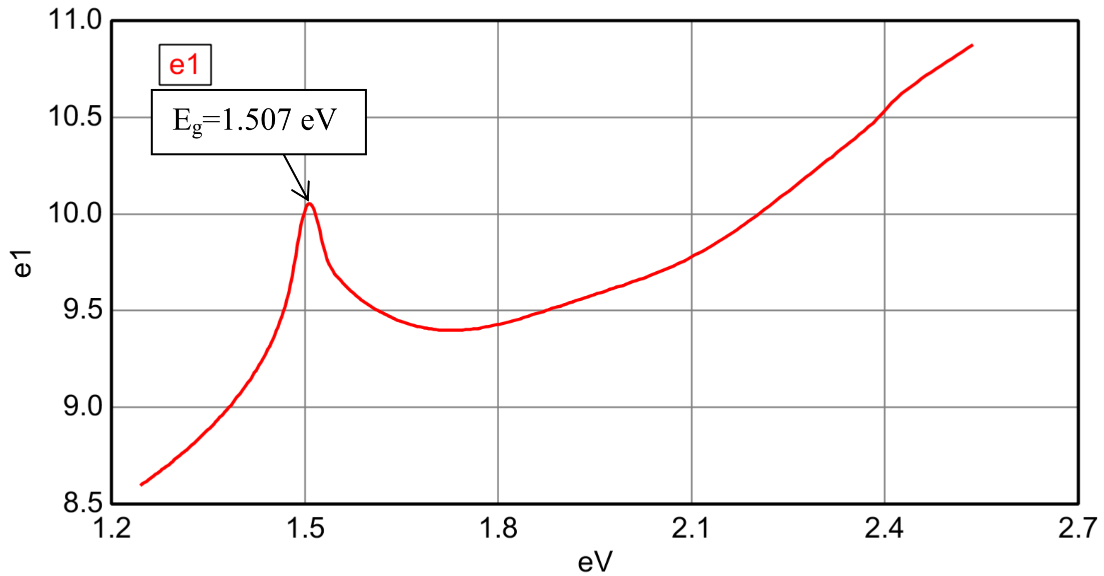

Figure 54. Real part of dielectric function of CdTe near the bandgap (Sample CT7).

In the previous section, four different models to fit experimental measurements of CT7 sample was demonstrated. The critical points and thickness values of CdTe obtained by these models were compared in Table 3. Principally, the critical points of Woollam model were not suitable to CdTe layer of the sample CT7. These critical points were related to the CdTe provided with the software library. Even so, it can be said that the critical points of this sample were very close to the CdTe layer that we grew.

Table 3. Comparison of some CdTe parameters obtained from four different models.

Parameter	**Woollam Model**	**5 Gen-Osc Model**	**7 Gen-Osc Model**	**9 Gen-Osc Model**
MSE	27.898	13.513	11.577	8.919
CdTe-Oxide Thickness (nm)	1.73	3.25	2.64	2.78
CdTe Thickness (nm)	1086.93	1032.77	1040.80	1045.52
Ec (eV) near bandgap	-	1.508	1.515	1.532
Eg (eV) (Using $d\varepsilon_1/dE$)	1.50	1.509	1.507	1.507
Eg (eV) (Using $d^2\varepsilon_2/dE^2$)	-	1.507	1.508	1.506
E_g+Δ (eV) (Using $d\varepsilon_2/dE$)	-	-	2.308	2.460
E_1 (eV) (Using $d\varepsilon_2/dE$)	3.321	3.316	3.329	3.312
E_1+Δ (eV) (Using $d\varepsilon_2/dE$)	3.866	3.826	3.819	3.804
E_2 (eV) (Using $d\varepsilon_2/dE$)	-	-	-	5.015

The position of the critical points E_g, $E_g+\Delta$, E_1, $E_1+\Delta$ and E_2 and four oscillators in the 9 general oscillator model corresponding to these points are demonstrated in Figure 55. The critical point values in the Table 3 were obtained by using the derivations of real and imaginary parts of the dielectric function which constructed by three different general oscillator models. The peak energy parameters of the oscillators corresponding to these values were slightingly different from each other. For example in Figure 55 the peak energy parameter of the yellow colored psemi-tri oscillator is Ec=2.484 eV and corresponding critical transition point is $E_g+\Delta$= 2.460 eV, the peak energy parameter of the blue colored psemi-tri oscillator is E_c=3.315 eV and corresponding critical transition point is E_1= 3.312 eV. The peak energy parameter of the red colored harmonic oscillator is E_o=3.837 eV and corresponding critical transition point is $E_1+\Delta$= 3.804 eV. The peak energy parameter of the purple colored harmonic oscillator is E_o=5.000 eV and corresponding critical transition point is E_2= 5.015 eV. Comparision of the critical points obtained by 9 general oscillator model and the ones obtained by the first derivative of e2 are shown in Figure 56.

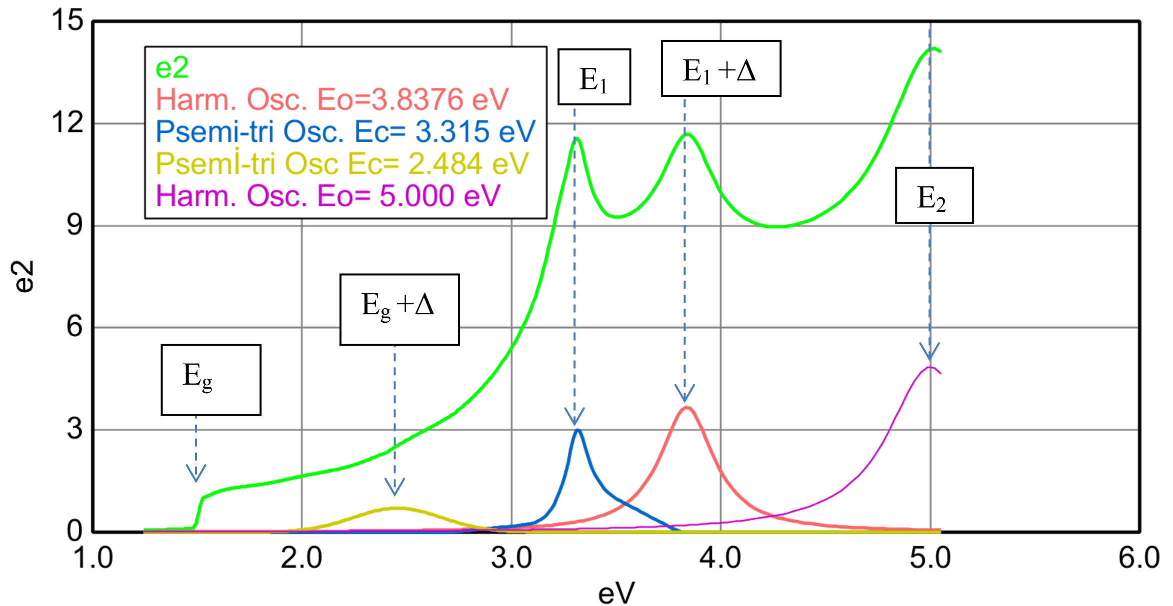

Figure 55. Imaginary part of the CdTe dielectric function and some critical points for the band structure of CdTe using 9 Gen-Osc model.

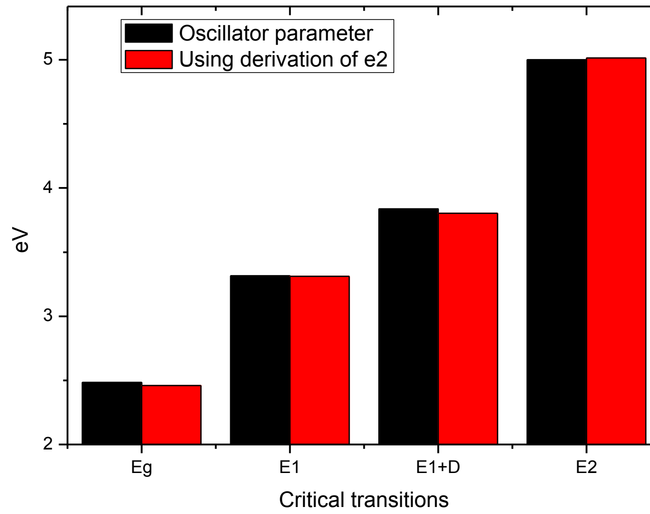

Figure 56. Comparison of critical points obtained from oscillator parameters and derivation of e2.

Table 4. Comparison of critical points of CdTe at room temperature from different studies.

Critical points (eV)	**7Gen-Osc Model**	**9Gen-Osc Model**	**CC.Kim *et al.* [65]**	**Benhlal *et al.* [33]**	**Adachi *et al.* [31]**	**Cardona *et al.* [66]**	**Arwin *et al.* [67]**	**L.Vina *et al.* [68]**
$\mathbf{E_g}$	1.507	1.507	1.500	1.504	1.50	-	-	-
$\mathbf{E_g + \Delta}$	2.308	2.460	2.422	2.432	-	2.4	-	-
$\mathbf{E_1}$	3.329	3.312	3.372	3.347	3.32	3.32	3.363	3.287
$\mathbf{E_1 + \Delta}$	3.819	3.804	3.989	3.924	3.87	3.88	3.968	3.848
$\mathbf{E_2}$	-	5.015	5.070	5.042	5.07	-	4.99	5.068

The critical points of CdTe obtained in this study at room temperature are compared to those reported in the literature in Table 4. In order to easily see the comparison of critical points of CdTe at room temperature obtained from [65], [33] and 9 oscillator model Figure 57 was also plotted. This figure shows that obtained critical point parameters were in very good agreement with other reported values.

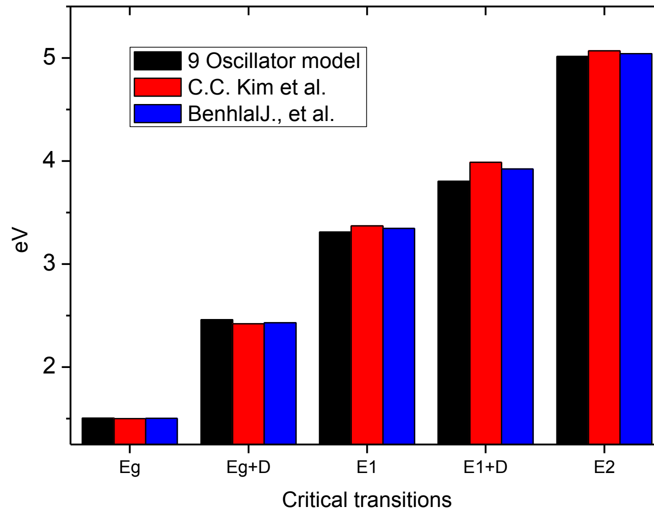

Figure 57. Comparison of critical points of CdTe at room temperature obtained from [65], [33] and 9 oscillator model.

The broadening parameters corresponding to these critical points were also tried to determine from the oscillator models. However, using the oscillator models the broadening parameters which are actually inversely proportional to the lifetime of an excited electron could not be accurately determined. Because the oscillators that are near to the critical transition points do not represent individually these transitions. In other words the broadening parameters of the oscillators which were used in this study were compared to those reported in the literature in Table 5 and Figure 58. It can be concluded that the obtained broadening parameters of general oscillator models are not reliable. The literature reported broadening parameters are also not very close to each other.

Table 5. Comparison of broadening parameters of CdTe at room temperature from different studies.

Broadening Parameters (eV)	**7 GenOsc Model**	**9GenOsc Model**	**C.C.Kim, *et al.* [65]**	**Benhlal, *et al.* [33]**	**Adachi, *et al.* [31]**	**Arwin *et al.* [67]**	**L.Vina *et al.* [68]**
$\Gamma(E_g)$	0.0062	0.0098	0.005	0.008	0.01	-	-
$\Gamma(E_g+\Delta)$	1.0096	0.2379	0.032	0.020	-	-	-
$\Gamma(E_1)$	0.0264	0.0220	0.078	0.051	0.07	0.055	0.025
$\Gamma(E_1+\Delta)$	0.0026	0.3181	0.091	0.088	0.12	0.077	0.100
$\Gamma(E_2)$	0.1167	0.4962	0.156	0.167	0.33	-	0.240

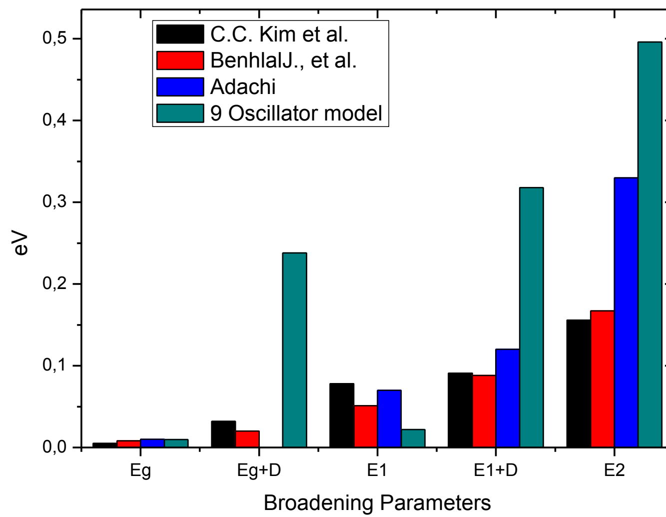

Figure 58. Comparison of broadening parameters of CdTe at room temperature from different studies.

In order to obtain the critical points E_1, $E_1 +\Delta$ and E_2, first derivative of e2 (Figure 59) can be used or in order to obtain bandgap, second derivative of e2 (Figure 60) or the first derivative of e1can be used.

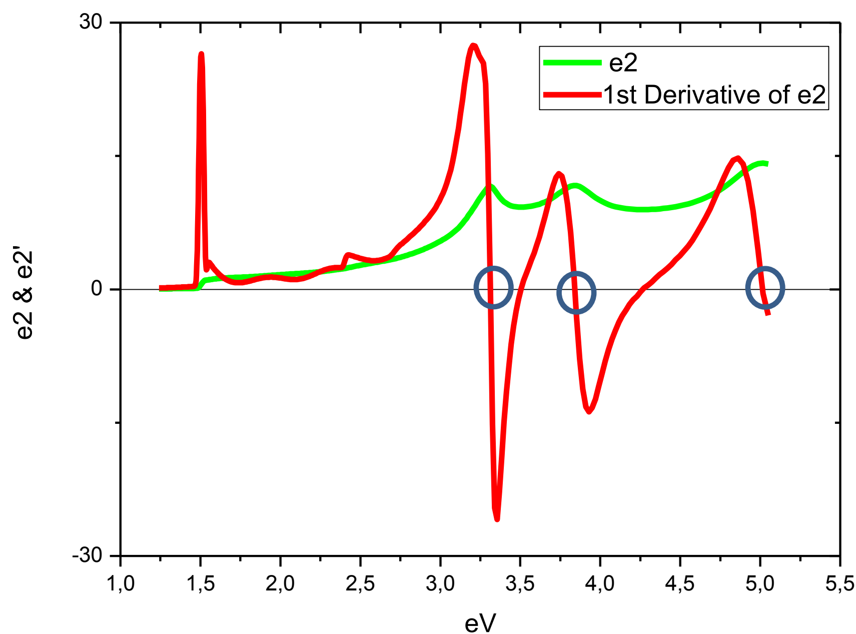

Figure 59. Imaginary part and first derivative of imaginary part of the CdTe dielectric function.

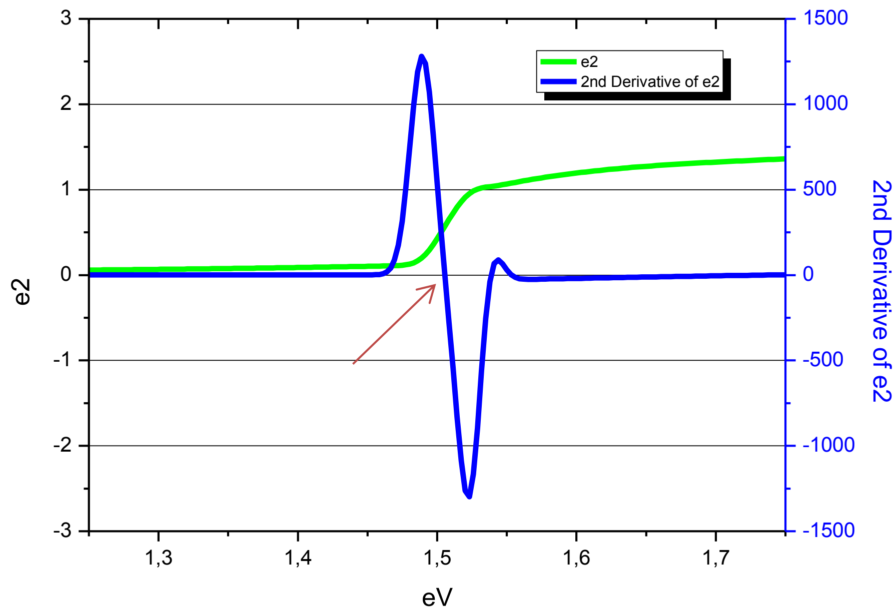

Figure 60. Imaginary part and second derivative of the imaginary part of the CdTe dielectric function. Arrow indicates the bandgap value of 1.506 eV.

4.2.1.1. Temperature Dependency of Critical Points of CdTe

In this section, temperature dependency of dielectric function and its critical points of CdTe for sample CT7 were studied. The surface temperature of the sample changed gradually with equal intervals using a heat gun. *Ex situ* ellipsometric measurements were taken from room temperature to higher temperatures. The temperature of the heat gun was arranged from 60°C to 420°C with 40°C interval and each temperature was applied to the sample for 3 minutes. However, these values did not correspond to actual surface temperature of the sample which were measured by IR thermometer. Heat gun temperatures between 60-420°C corresponded to the temperatures between 40-118°C as measured by IR thermometer.

The imaginary parts of the dielectric function of CdTe for 11 different temperatures are given in Figure 61. As temperature increased the critical point values and corresponding e2 values decreased. In Figure 62 the imaginary parts of the dielectric function of CdTe for 11 different temperatures were also given for 2.7 -4.2 eV spectral range. As temperature increased critical points E_1 and $E_1+\Delta$ decreased, but corresponding e2 values did not seem to decrease very regularly.

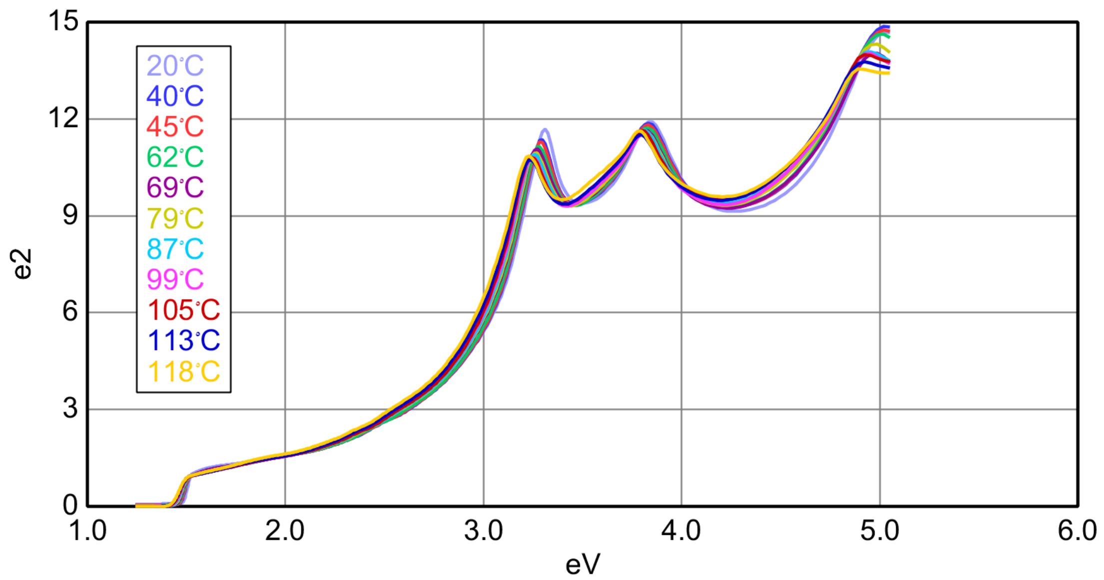

Figure 61. Temperature dependency of CdTe imaginary part dielectric function of sample CT7.

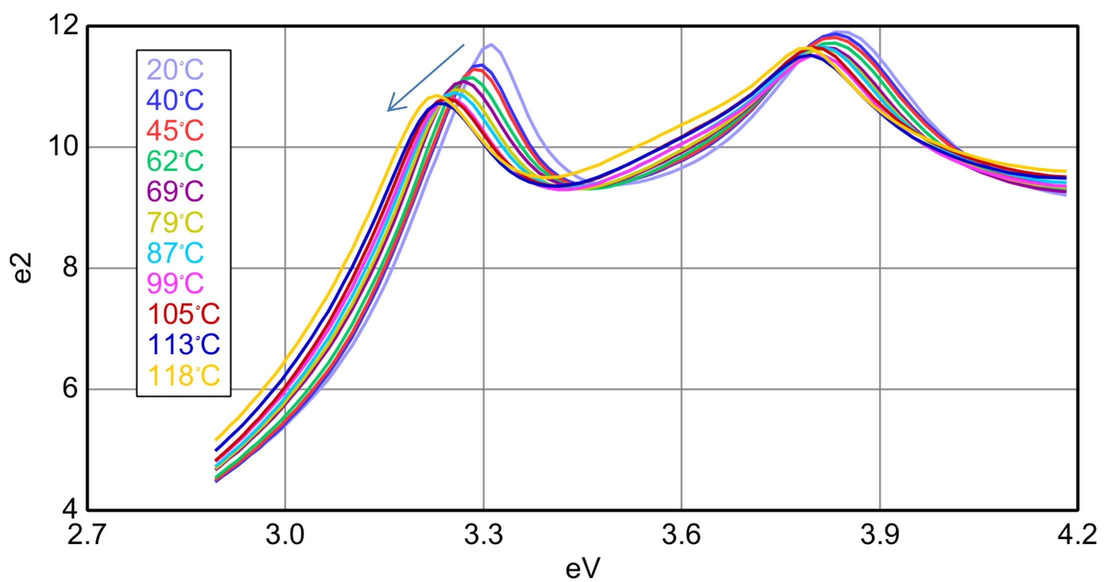

Figure 62. Temperature dependency of CdTe imaginary part dielectric function from 2.7 eV to 4.2 eV for sample CT7.

Temperature dependencies of these two critical points are given in Figure 63. The obtained results were fitted with linear functions. The adjustment R-square values of these linear functions were obtained as 0.993 and 0.972 for critical points E_1 and $E_1+\Delta$, respectively. By looking at the fitting results it can be said that E_1 is more appropriate than $E_1+\Delta$ for determining the temperature of CdTe sample according to R-square values.

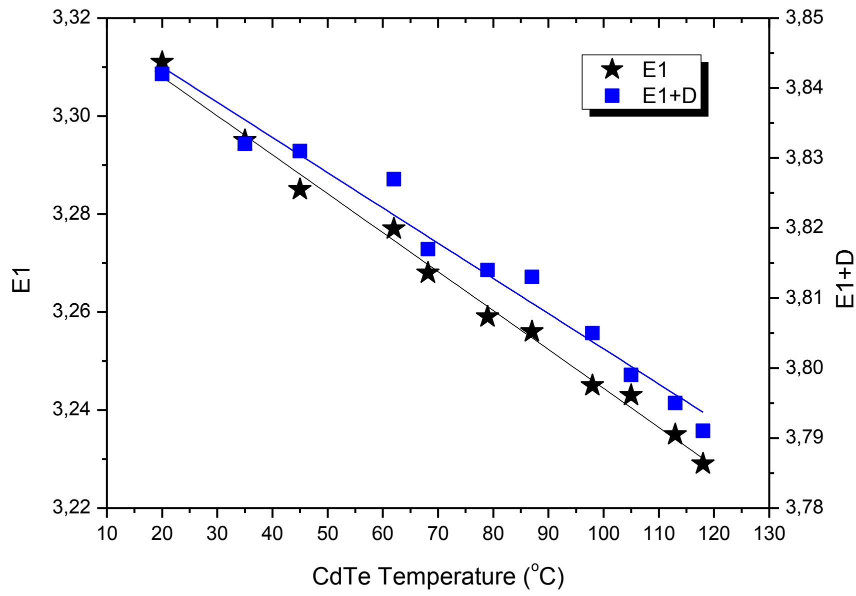

Figure 63. Temperature dependency of critical points E_1 and $E_1+\Delta$ of CdTe.

Temperature dependency of E_1 critical point of CdTe for the interval 20-118°C was found as,

$$E_1=3.324-(7.95\times10^{-4})\,T.$$

The temperature dependency of E_1 of CdTe for the interval 20-270°C was also reported by Li *at al.* [69] (Figure 64). The slope of this linear dependency is -7.30×10^{-4} eV/°C which is very close to the value obtained in this study.

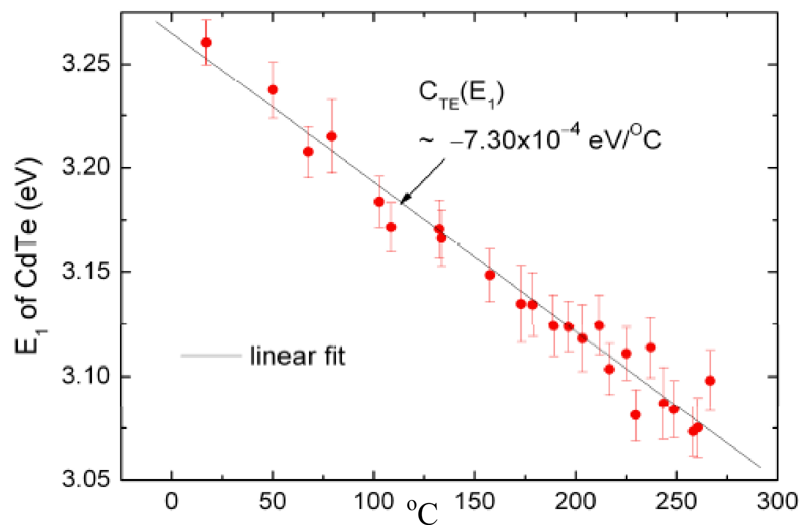

Figure 64 Temperature dependency of $E_1$of CdTe obtained from Li *et al.* [69]

The temperature dependency of $E_1+\Delta$ critical point of CdTe for the interval 20-118°C was found as,

$$E_1+\Delta=3.853-(5.033\times10^{-4})T.$$

In Figure 65 temperature dependency of critical points E_g and E_1 of CdTe can be seen. Temperature dependency of E_1 was given again in this figure. The temperature values and corresponding E_g values were fitted linearly with 0.981 adjustment R-square value as,

$$E_g=1.511-(3.6572\times10^{-4})T$$

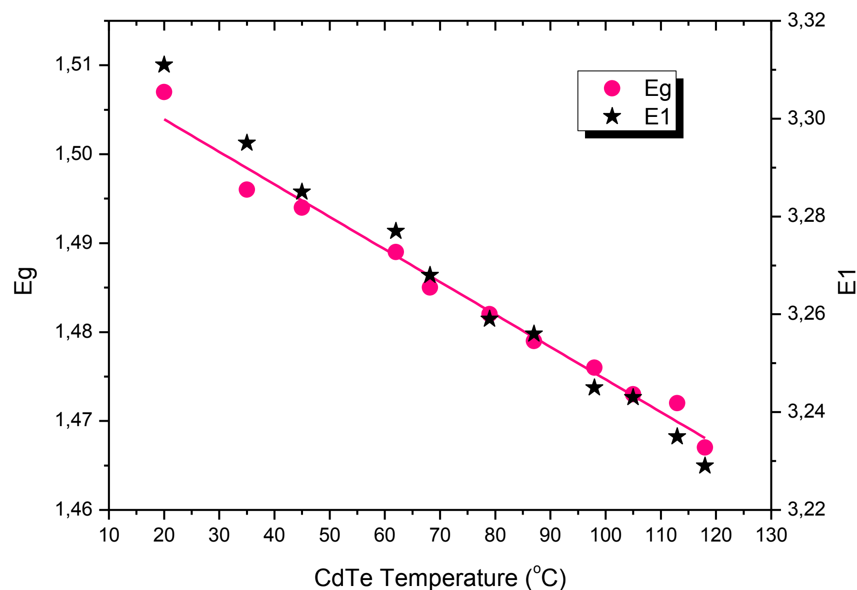

Figure 65. Temperature dependency of critical points E_g and E_1 of CdTe.

As a conclusion, to determine the temperature of the CdTe, temperature dependencies of the critical points E_g, E_1 and $E_1+\Delta$ can be used.

4.2.2. CdZnTe Band Structure and Critical Points

Optical properties of bulk grown ternary alloy CdZnTe was also measured by SE and its dielectric function was constructed. It was known that the composition of $Cd_{1-x}Zn_xTe$ was x=0.04.The obtained experimental data and model fit of the real and imaginary parts of the pseudo dielectric function of the CdZnTe are given in Figure 66.

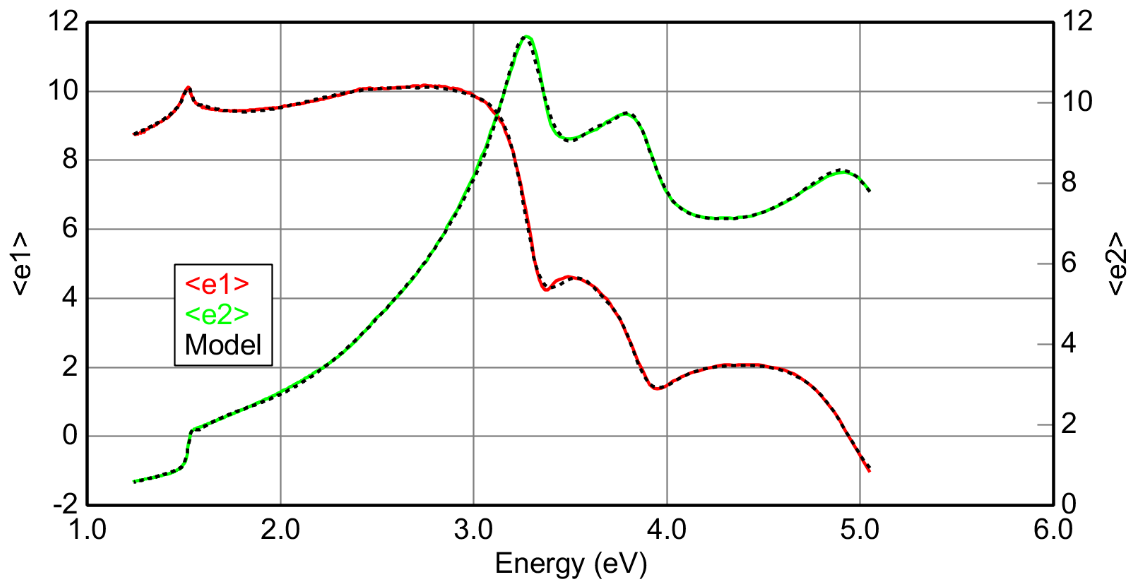

Figure 66. Real and imaginary parts of the pseudo dielectric function of the CdZnTe bulk with native oxide.

The agreement between the model and experimental data was excellent. The constructed model included oxide on CdZnTe surface. For the oxide layer CdTe oxide which was in the software library was used. For the CdZnTe general oscillators were used. Imaginary part of the dielectric function of CdTe in the software library was used as a reference material and this function fitted with nine general oscillators and then these oscillators for the CdZnTe layer was used in the model. All variables of the oscillators were the fit parameters. Consequently the dielectric function of the CdZnTe (Zn rate 4%) was constructed as in Figure 67.

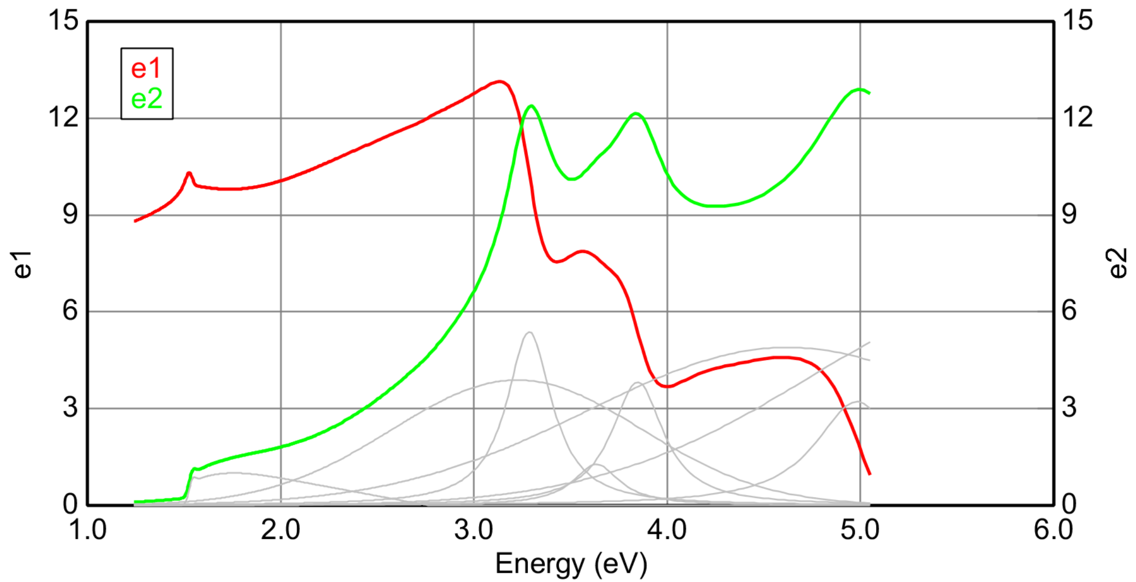

Figure 67. Real and imaginary parts of the dielectric function of the CdZnTe bulk that was modeled with 9 general oscillators.

Bandgap of the CdTe is about 1.508 eV and bandgap of the ZnTe is about 2.24 eV at room temperature [70]. The bandgap increases almost linearly from value for CdTe to that for ZnTe. Therefore, the bandgap of the CdZnTe is expected be slightly more than CdTe. The bandgap of the CdZnTe was found as 1.526 eV by using first derivative of the real part of the dielectric function of the CdZnTe. The comparison of the real parts of the dielectric function of CdTe and CdZnTe for the 1.2-2.2 eV range is given in Figure 68.

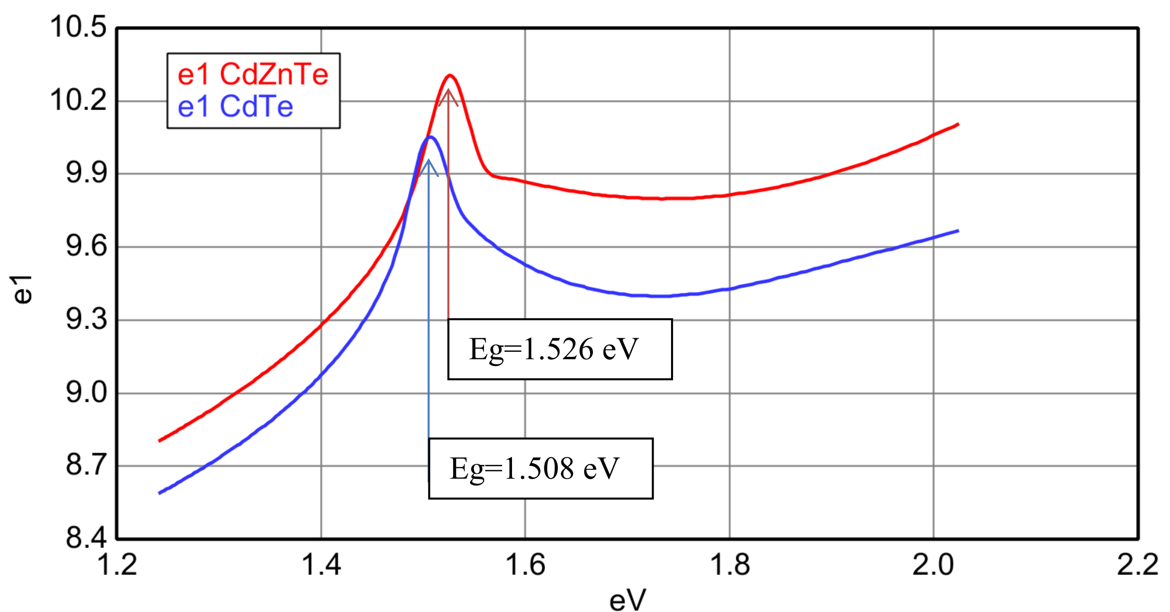

Figure 68. Real part of the dielectric functions of the CdZnTe (4 % Zn) and CdTe near the bandgap.

In Table 6, critical transition energies of CdZnTe (Zn, 4%) obtained from 6 general oscillator model and 9 general oscillator model and published values were compared. As a result, obtained parameters in this study were close to the reported values.

Table 6. Critical transition energies of CdZnTe (Zn, 4%) obtained from different methods and their comparison.

Critical transitions of CdZnTe (x=0.04)	**6 Gen-Osc Model** MSE=2.720		**9 Gen-Osc Model** MSE=1.528		**Sridhara M., *et al.* [71]**
	Oscillator Parameter	CP	Oscillator Parameter	CP	
E_g (eV)	1.533	1.527	1.553	1.526	-
$E_g+\Delta$ (eV)	2.328	-	-	-	-
E_1 (eV)	3.293	3.299	3.286	3.298	3.20
$E_1+\Delta$ (eV)	3.848	3.849	3.846	3.833	3.99
E_2 (eV)	-	-	4.988	4.989	4.96

4.2.3. GaAs Band Structure and Critical Points

The pseudo dielectric function of epi-ready GaAs wafer for the spectral range from 1.24 to 5.05 eV is given in Figure 69. This experimental data was fitted for the spectral range from 1.4 to 5.05 eV. The model was composed of surface oxide layer and GaAs substrate. For the oxide layer 'GaAs oxide' which was in the software library was used. For the fitting of measurement general oscillators were used. The obtained dielectric function and oscillators used for the GaAs can be seen in Figure 71.

The thickness of the oxide layer was obtained as about 1 nm from this analysis. Because of the high depolarization effect below the bandgap energies, model data were constructed from 1.4 to 5.05 eV. For this reason the bandgap energy could not be found

from the model since no peak in the real part of the dielectric function was found near the bandgap.

The expected bandgap value of GaAs is 1.425 eV at room temperature [72]. However, a valley point near the bandgap occurred in the second derivative of real part of the GaAs (Figure 72). This valley point found as 1.396 eV which may have correspond to bandgap energy.

The band structure and critical transition points for the GaAs can be seen in Figure 70. The critical points of the GaAs sample were found by imaginary part of the dielectric function which was construced from this analysis. Some of the critical energy values of GaAs were obtained as E_1=2.909 eV, $E_1+\Delta$= 3.095 eV, $E_o^{'}$=4.424 eV and E_2=4.701 eV (Figure 71). Reported critical transition values for GaAs at room temperatures were given as E_1=2.9 eV, $E_1+\Delta$= 3.15 eV, $E_o^{'}$=4.6 eV and E_2=4.8 eV [73].

The comparison of the three different GaAs samples at room temperature can be seen in Figure 73. In this figure dotted lines are GaAs materials in Woollam library and solid lines are our modeled GaAs sample.

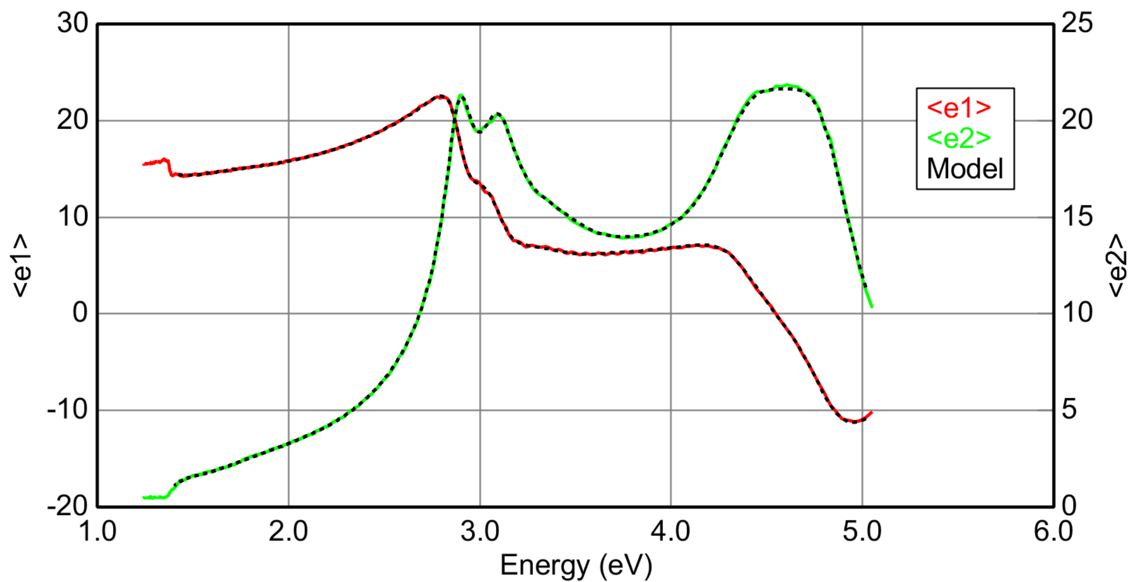

Figure 69. Real and imaginary parts of the pseudo dielectric function of the GaAs substrate with oxide.

Figure 70. Band structure of GaAs and its main inter-band transitions [35].

Figure 71. Imaginary parts of the dielectric function of the GaAs that was modeled with 6 general oscillators. E_1=2.909 eV, $E_1+\Delta$= 3.095 eV, $E_o^{'}$=4.424 eV and $E_2+\Delta$=4.701 eV.

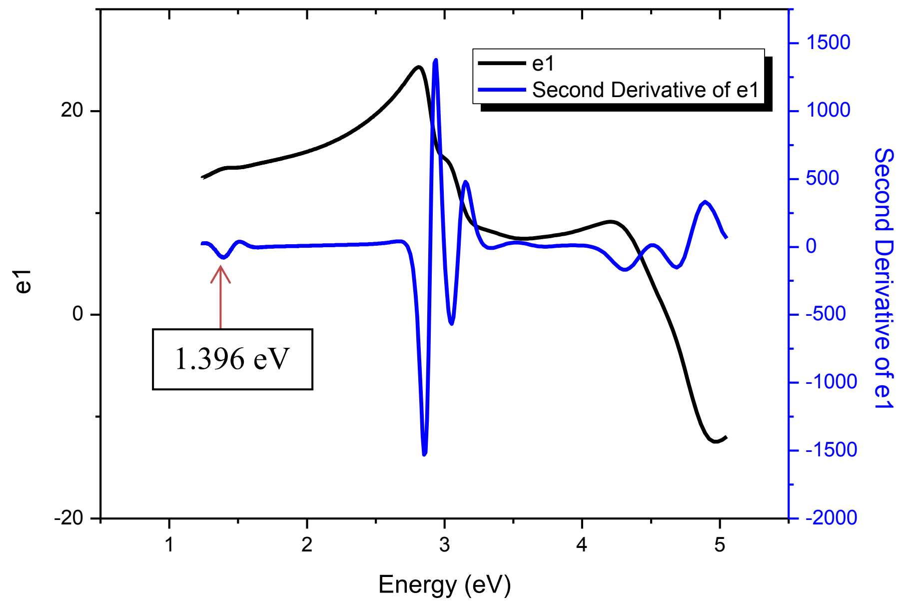

Figure 72. Real part and second derivative of real part of the dielectric function of the GaAs sample.

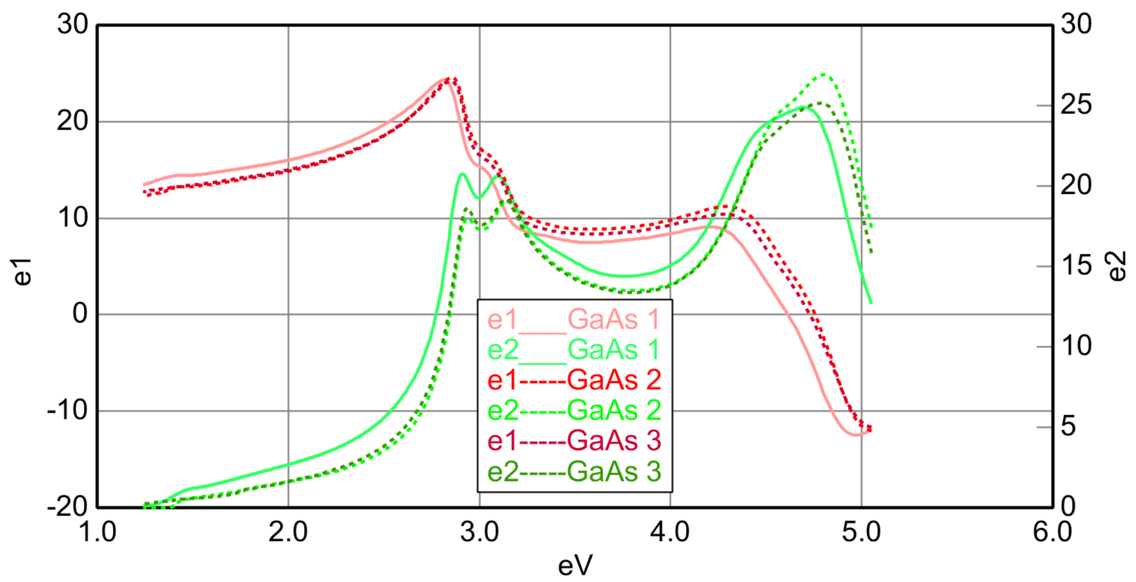

Figure 73. Comparison of the three different GaAs samples at room temperature. Dotted lines are GaAs materials in Woollam library and solid lines are our modeled GaAs sample.

CHAPTER 5

EXPERIMENTAL RESULTS FOR CDTE GROWN ON GAAS

In this chapter, experimental results and discussions for molecular beam epitaxially grown CdTe thin film samples were given. The CdTe films were grown by the Gen-20MZ MBE system facility at the Department of Physics at IZTECH. Fifteen samples were grown under different growth conditions and different thicknesses. The sample numbers were given according to the growth order from CT1 to CT15 for all these fifteen CdTe samples which were examined in this study.

5.1. MBE Grown CdTe Buffer Layers

CdTe growth on GaAs(211)B substrates were carried out in the MBE reactor. The growth chamber was equipped with CdTe and Te corrosive valved cracker cells. A standard cracker cell was used to provide As_4 flux during substrate surface preparation. Substrate temperature was controlled by a non-contact thermocouple (TC). Substrate temperature was also measured by a pyrometer and bandedge measurement system (BandiT) [74] which were more accurate than TC [75]. There was 100^oC to 200^oC offset between BandiT and TC reading. Prior to growth, protective oxide on the epiready GaAs was thermally desorbed for all samples. These deoxidation processes were carried out at high temperatures. Deoxidation temperatures were between 550-600^oC. These temperature values were read by BandiT which is also called as band edge thermometer that uses the inverse relationship of semiconductor bandgap (E_g) with substrate temperature. During deoxidation, As_4 flux was supplied in order to stabilize surface of the GaAs. Complete desorption of the protective oxide was verified by reflection high energy electron diffraction (RHEED) patterns (Figure 74). The CdTe nucleation layer was grown at about 250^oC after deoxidation. CdTe was grown after the nucleation layer process at about 350^oC.

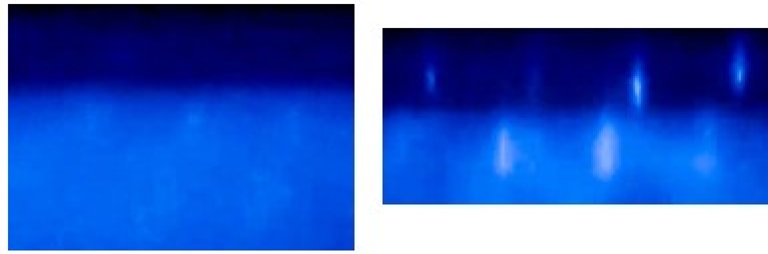

Figure 74. RHEED patterns before (left) and after deoxidation of GaAs.

Some characterization results and growth parameters for all these CdTe films grown on GaAs are given in Table 7. All of the SE analyses after the growth were done by using 9 oscillator model for CdTe layers. This model was discussed in chapter 4 (Figure 52).

Bandgap values were determined from real parts of the dielectric functions by calculating the first derivative of e1 near the bandgap as it was demonstrated in chapter 4. Refractive indexes (n) of the CdTe layers were also determined at 632.8 nm which is the Helium-Neon laser [57] operation wavelength corresponds to 1.96 eV. The thicknesses of CdTe layers were determined by using both SE and Fourier transformation infrared (FTIR) spectroscopy. Crystal quality of the CdTe layers were determined by using X ray diffraction (XRD) measurements and by analyzing full width at half maximum (FWHM) of the rocking curves (RC). The FWHM values for CT4, CT6 and CT7 could not be determined because the crystal orientations of the samples could not be found. Surface roughness values of the samples were determined by atomic force microcopy (AFM) and oxide thicknesses were determined by SE analysis.

In Table 7, two growth conditions (growth rate and VI/II rate) are also given. VI/II rate means that the rate of the total amount of group VI element Te and the amount of the group II element Cd in the MBE chamber during growth. These amounts measured by determining the beam equivalent pressures (BEP) of theTe_2 flux and CdTe flux. The VI/II rate was kept at about 3 by adjusting the Te_2 flux and CdTe flux to obtain stoichiometric CdTe growth. VI/II rate versus bandgap of CdTe can be seen in Figure 75.

Other growth parameters such as growth temperature, growth rate, oxide removal time and temperature and nucleation time and temperature should be also taken into account in order to correlate with characterization results.

Table 7. CdTe films grown on GaAs and some characterization results and growth parameters.

Sample No	Band gap	n (632.8 nm)	CdTe Thickness		FWHM	Surface		Growth	
	SE (eV)	SE	SE (µm)	FTIR (µm)	XRD RC (arcsec)	Oxide SE (nm)	Rough-ness AFM (nm)	VI/II Rate	Growth rate (µm /hour)
CT1	1.510	3.19	0.33	0.39	393	1.97	3.01	2.61	0.44
CT2	1.449	3.69	0.20	1.01	630	17.77	26.28	4.5	0.605
CT3	1.515	3.17	1.30	1.31	780	4.95	8.4	2	0.87
CT4	1.508	3.1	1.36	1.45	–	2.6	21.12	3	0.916
CT5	1.506	3.14	1.32	1.42	412	2.3	7.03	3	0.913
CT6	1.508	3.12	1.92	2.06	–	2.96	10.63	3	0.996
CT7	1.508	3.11	1.05	1.12	–	2.77	22.5	3	0.722
CT8	1.506	3.1	1.92	2.24	252	0.77	9.18	–	1.18
CT9	1.506	3.13	1.63	1.73	280	2.5	13.58	3.1	1.19
CT10	1.506	3.06	5.05	4.91	116	3.03	22.08	2.78	1.137
CT11	1.508	2.95	2.13	2.08	284	10.43	8.07	2.88	1.052
CT12	1.500	3.01	2.49	2.46	292	6.02	15.8	2.88	1.10
CT13	1.494	2.8	2.15	2.06	238	5.47	40.19	2.82	0.931
CT14	1.495	2.97	1.60	1.60	476	3.64	35.53	3	0.707
CT15	1.500	2.98	2.00	1.88	472	6.73	25.44	3	0.86

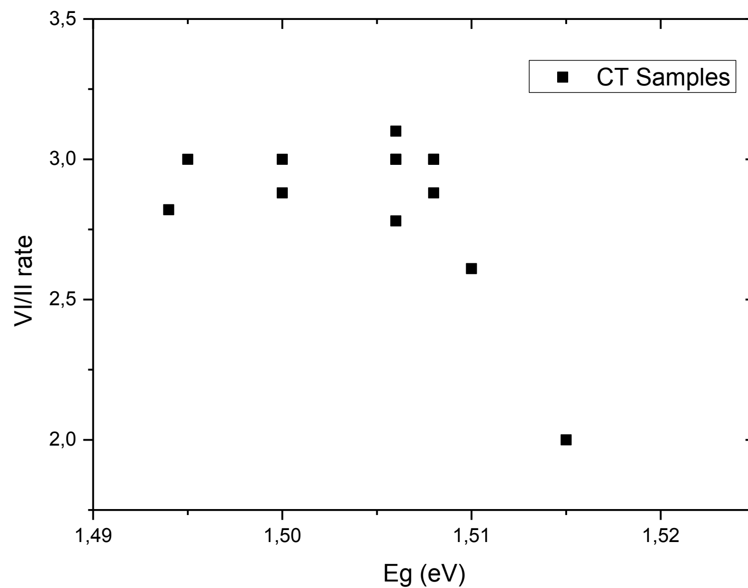

Figure 75. VI/II rate versus bandgap of CdTe.

5.1.1. CdTe Thickness Determination

In this section, we discuss how the thicknesses of CdTe layers were obtained. Ellipsometric data and model fit for three samples CT10, CT13 and CT7 that have different thickness values can be seen in Figure 76, Figure 77and Figure 78. Thickness values of CT10, CT13 and CT7 was found as 5054.17 nm, 2147.63 nm and 1045.52 nm, respectively. These figures of pseudo dielectric functions selected as wavelength dependent in order to see oscillations, which are formed between 820 nm and 100 nm, easily. As the thickness of the CdTe is increased these oscillations becomes more frequents.

The thickness results were found to be compatible with growth rate and growth time. For all samples, except CT2, the thickness values of CdTe were obtained from both SE and FTIR measurements. SE and FTIR thickness measurement comparison can be seen in Figure 79. A positive Pearson correlation coefficient of 0.988 was obtained between the two techniques and the slope of the linear fit was obtained as 1.044. These fit results showed that our thickness values obtained from SE analysis were consistent and well-matched with FTIR results.

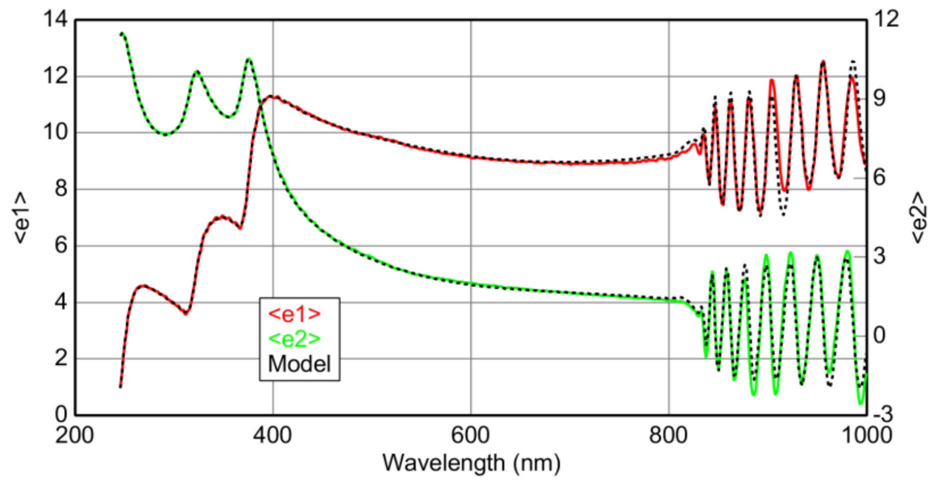

Figure 76. <e1> and <e2> versus wavelength for CT10 (5054.17 nm).

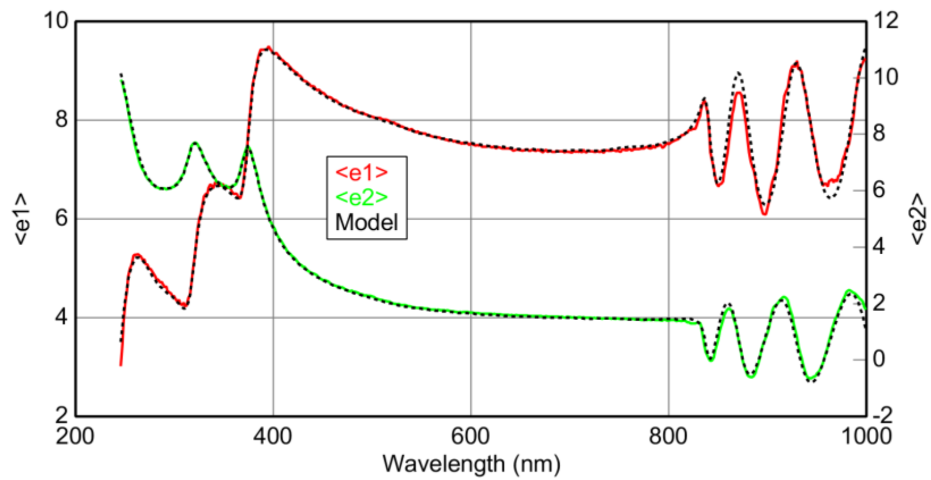

Figure 77. <e1> and <e2> versus wavelength for CT13 (2147.63 nm).

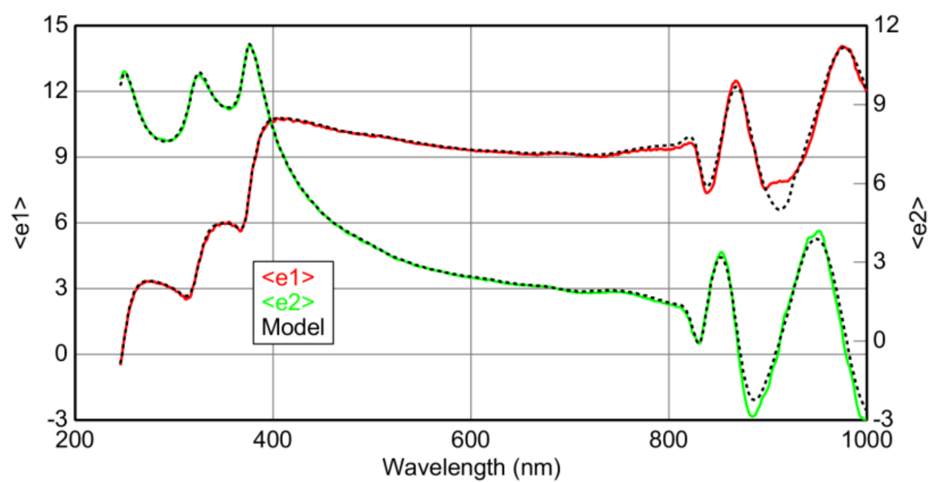

Figure 78. <e1> and <e2> versus wavelength for CT7 (1045.52 nm).

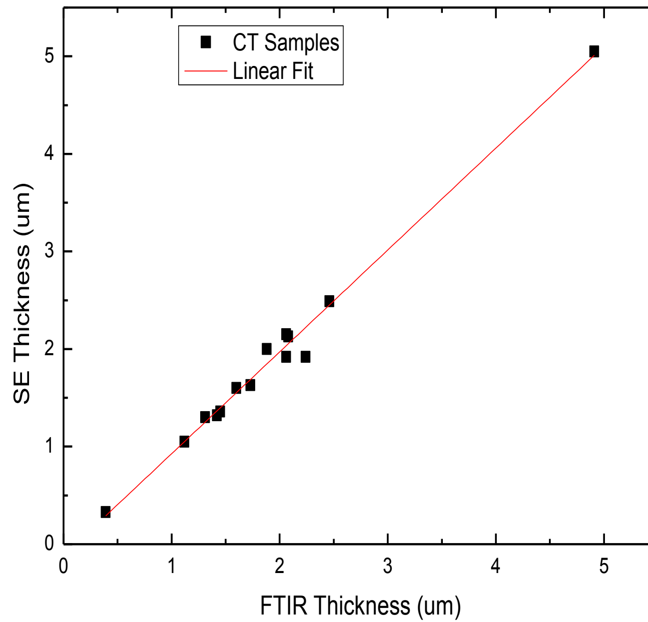

Figure 79. CdTe thickness obtained from SE measurements and FTIR measurements.

It is known that as the thickness of CdTe layers are increasing, FWHM value obtained from XRD is expected to decrease [76]. In Figure 80 this tendency can observed even though all samples were grown under different growth conditions. In order to obtain low FWHM value or in other words high crystallinity, it is necessary to optimize growth parameters and grow sufficiently thick CdTe layer.

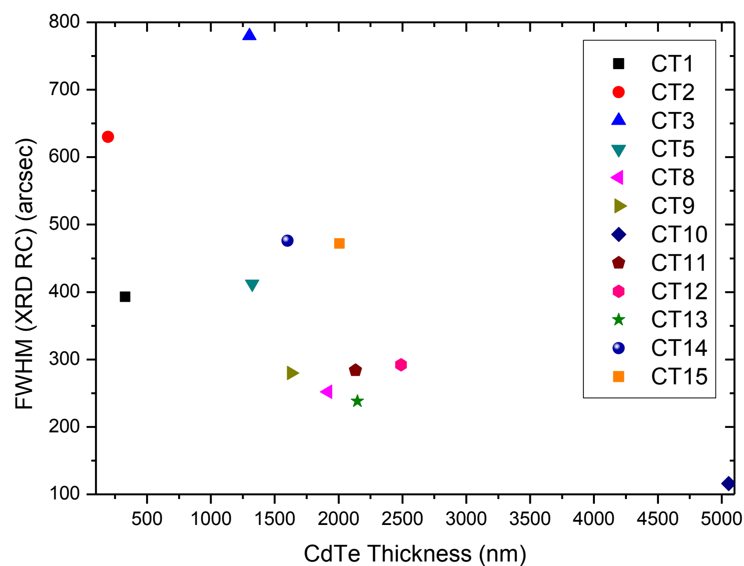

Figure 80. CdTe thicknesses versus FWHM values.

5.1.2. Growth Uniformity of CdTe

In this section growth uniformity of CT9, CT10 and CT13 were demonstrated by SE measurements. Thickness maps, refractive index maps at 632.8 nm and <e2> maps were drawn for these samples.

CT9 was grown on 4 inch GaAs(211)B full wafer. Before the growth, MBE chamber base pressure was $4.7\text{x}10^{-10}$ Torr. The sample was rotated with 2 rpm frequency during surface preparation and during growth. Oxide desorption was carried out at 650°C under $5.16\text{x}10^{-6}$ Torr As_4 flux. After deoxidation CdTe nucleation layer was grown under $7.06\text{x}10^{-7}$ Torr Te_2 flux at 250°C in 30 seconds. CdTe buffer layer growth was also performed for 80 minutes under $7.06\text{x}10^{-7}$ Torr Te_2 flux at 310°C. CdTe flux was $6.7\text{x}10^{-7}$ Torr.

Ellipsometric measurements were taken manually for 4-inch CT9 sample from 51 points (Figure 82). Thickness map for CdTe layer is given in Figure 81. It can be seen that the thickness was highly uniform over the surface for this 4-inch sample.

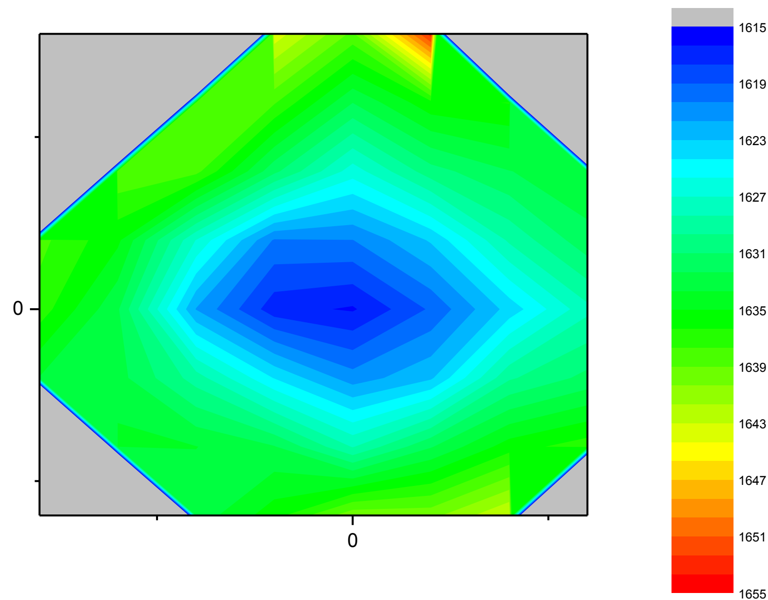

Figure 81. CT9 thickness map.

Thickness of the center, which is blue colored in the figure is about 1615 nm and green region is about 1639 nm. The difference between these values is about 25nm which corresponds to about 2% variation.

Although the thickness varied over the whole surface, there were four different regions on the surface of the sample CT9 (Figure 82). These areas labeled as a, b, c and d. The area (c) was mirror-like and other areas were milky. It can be inferred from the CdTe thickness map (Figure 81) that these different areas were not related to the CdTe thickness variation.

AFM images of CT9 surface for four regions can be seen In Figure 83. For roughness of the region (a), (b), (c) and (d) RMS values were found as 18.7 nm, 15.5 nm, 7.6 nm and 16.4 nm, respectively. Region (b) and (d) have very close surface roughness values and AFM images of these two regions were obtained as similarly.

These four regions were also obtained similarly by mapping imaginary part of the pseudo dielectric function of these 51 points at 3.31 eV (Figure 84) and also by mapping refractive index (Figure 85). The relation between RMS roughness and <e2> at 3.31eV was demonstrated for different samples in section 5.1.3. In Figure 85 blue region is region (a) and its <e2> values were found lower but its RMS roughness value was higher. Green regions that are region (b) and region (d) their <e2> values were found similar and higher than blue region (or region a) and RMS values of these two regions were also similar. Red region is region (c) and its <e2> values were found highest but its RMS was lowest. It can be inferred that surface roughness are inversely proportional to <e2> values.

A similar image was obtained by mapping refractive index of the CdTe as shown in Figure 85. This was already expected since imaginary part of the dielectric function is proportional to the refractive index.

Since it was not possible to obtain surface roughness of the sample accurately, by adding the EMA roughness layer on the optical model, the <e2> parameters at 3.31eV were considered as convenient way to estimate surface roughness.

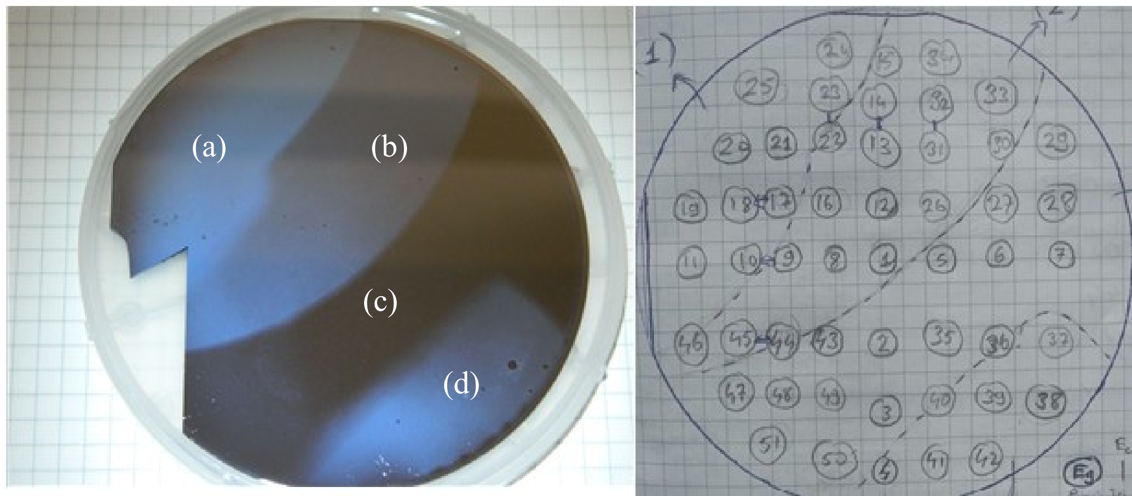

Figure 82. CT9 optical image and 51 points that measurements were taken.

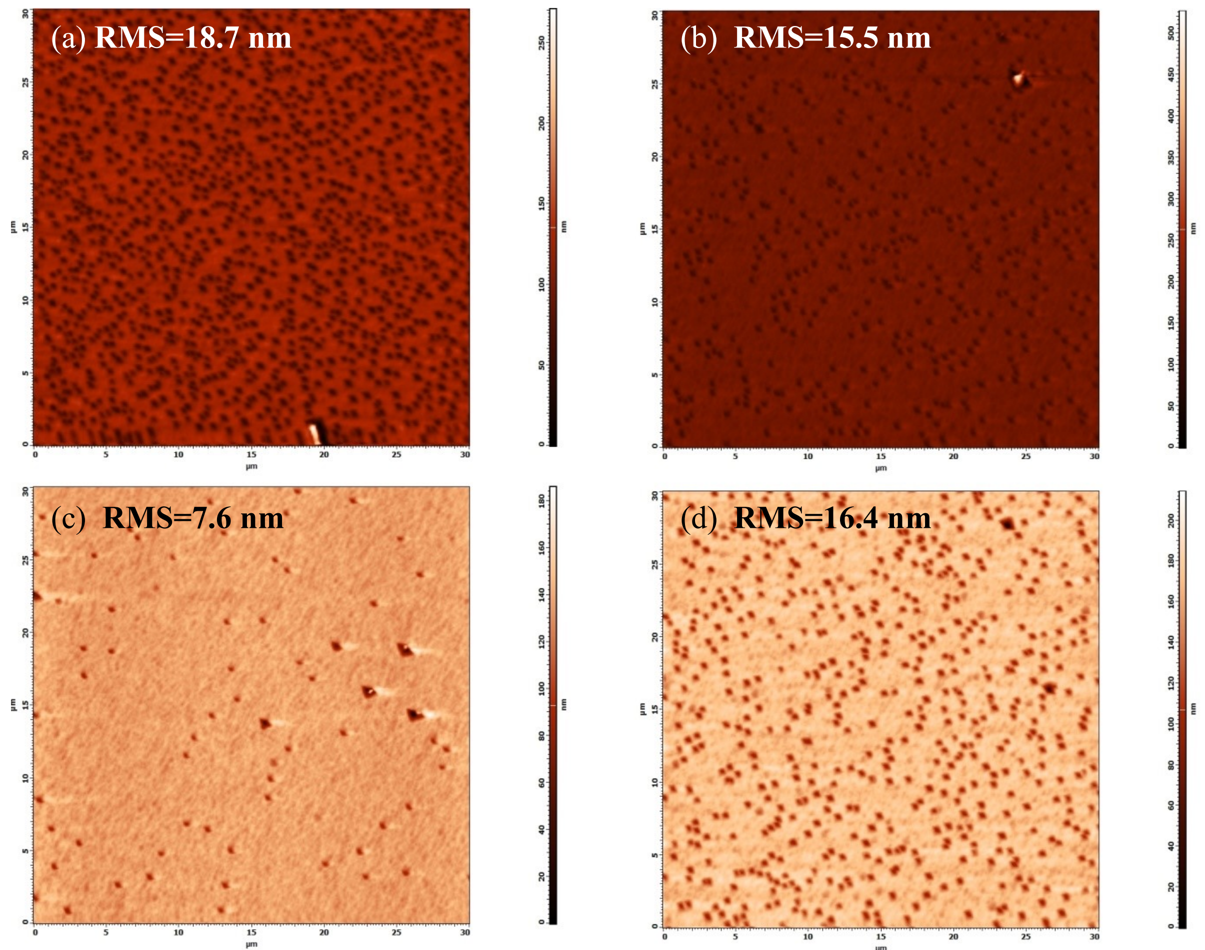

Figure 83. 30x30 μm^2 AFM images of CT9 for four regions. (a) RMS=18.7 nm, (b) RMS=15.5 nm, (c) RMS= 7.6 nm, (d) RMS= 16.4 nm.

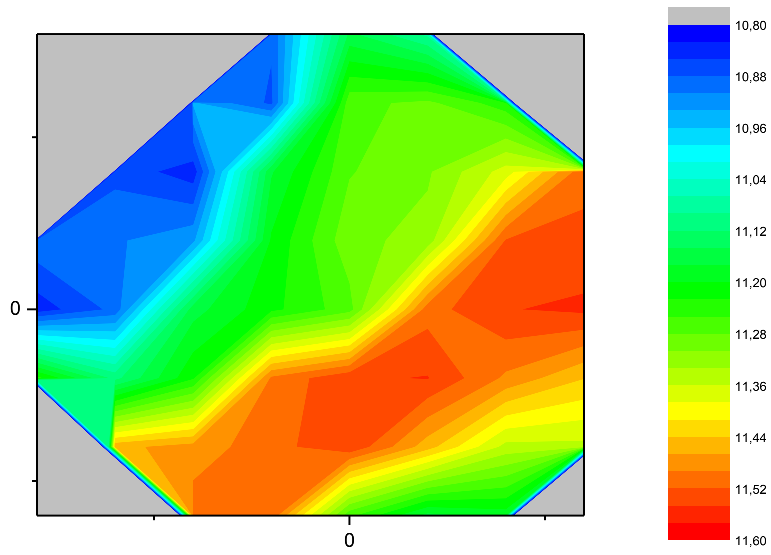

Figure 84. CT9 <e2> (3.31 eV) map.

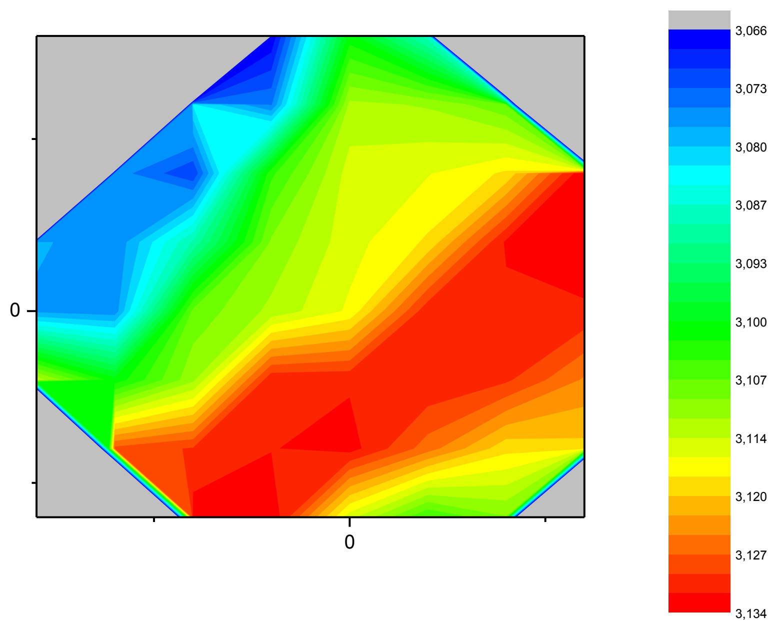

Figure 85. CT9 refractive index map (n values at 632.8 nm).

The sample CT10 was grown on a quarter of 3-inch GaAs(211)B wafer. Before the growth, MBE chamber base pressure was $4.7x10^{-10}$ Torr. The sample was rotated with 2 rpm frequancy during surface preparation and during growth. Oxide desorption was carried out at 600^oC under $5.15x10^{-6}$ Torr As_4 flux. After deoxidation CdTe nucleation layer was grown under $7.04x10^{-7}$ Torr Te_2 flux at 250^oC in 30 seconds. CdTe buffer layer growth was also performed in 4.38 hours under $7.04x10^{-7}$ Torr Te_2 flux at 310^oC. CdTe flux was $6.27x10^{-7}$ Torr.

Ellipsometric measurements were also taken manually for this quarter 3-inch CT10 sample from 43 points over the whole surface. Thickness map for CdTe layer is given in Figure 86. It can be seen that thickness values varying from 4930 nm to 5161 nm. Dark blue regions represent thicker areas. The thickness difference between dark blue and white region was found as 231 nm. This value corresponds to about 5% variation.

Refractive index map of the CdTe for CT10 was also obtained (Figure 87). Unlike previous sample, thickness map and refractive index map had some resemblances between them.

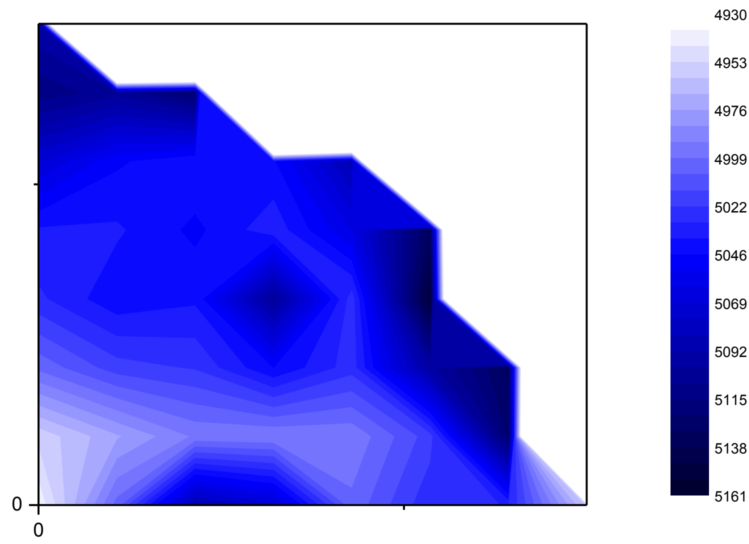

Figure 86. CT10 thickness map.

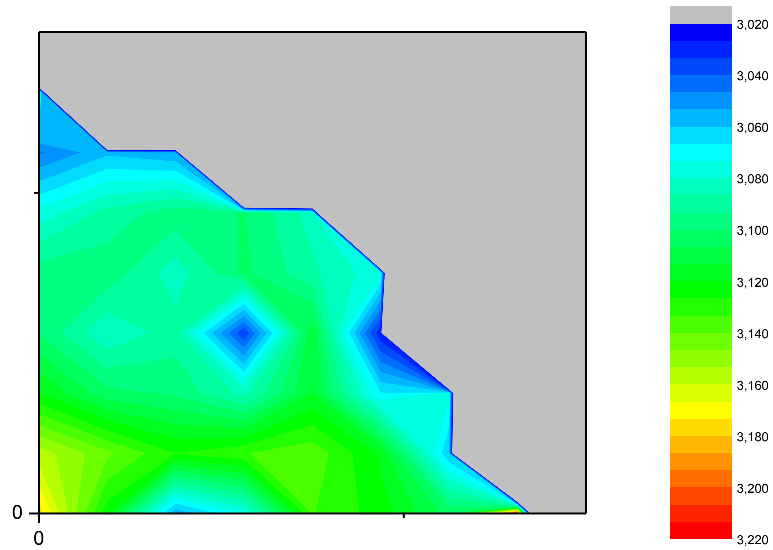

Figure 87. CT10 refractive index map (n values at 632.8 nm).

CT13 was grown on 20x20 mm^2 GaAs(211)B square wafer. Before growth, MBE chamber base pressure was $7.79x10^{-10}$ Torr. The sample was rotated with 2 rpm frequancy during surface preparation and during growth. Oxide desorption was carried out at 580^oC under $4.75x10^{-6}$ Torr As_4 flux. After deoxidation CdTe nucleation layer was grown under $7x10^{-7}$ Torr Te_2 flux at 270^oC in 30 seconds. CdTe buffer layer growth was also performed in 120 minutes under $7x10^{-7}$ Torr Te_2 flux at 333^oC. CdTe flux was $5.99x10^{-7}$ Torr.

Ellipsometric measurements were also taken manually for this 20x20 mm^2 CT10 sample from 9 points. Thickness map for CdTe layer is given in Figure 88. It can be seen that thickness values varying roughly from 2100 nm to 2220 nm and red regions represent thickest regions. Difference between blue and red regions found as 120 nm. For the sample CT13, <e2> map at 3.31 eV is also given in Figure 89.

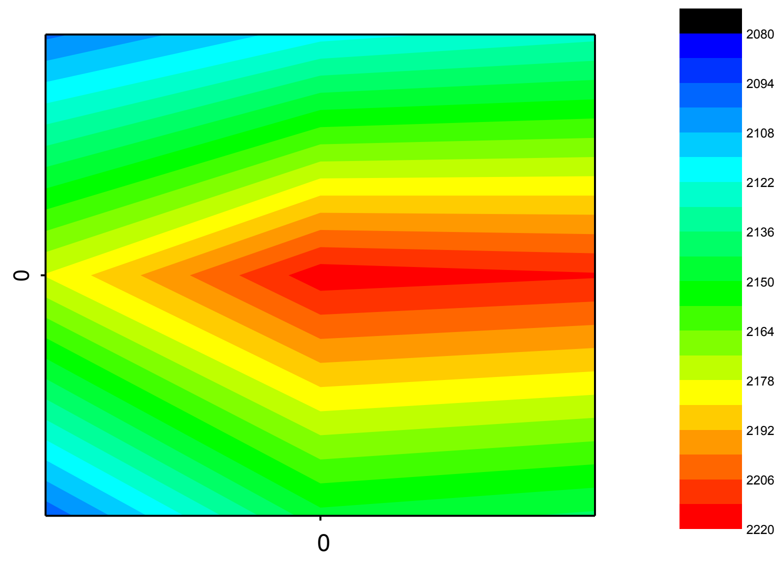

Figure 88. CT13 thickness map.

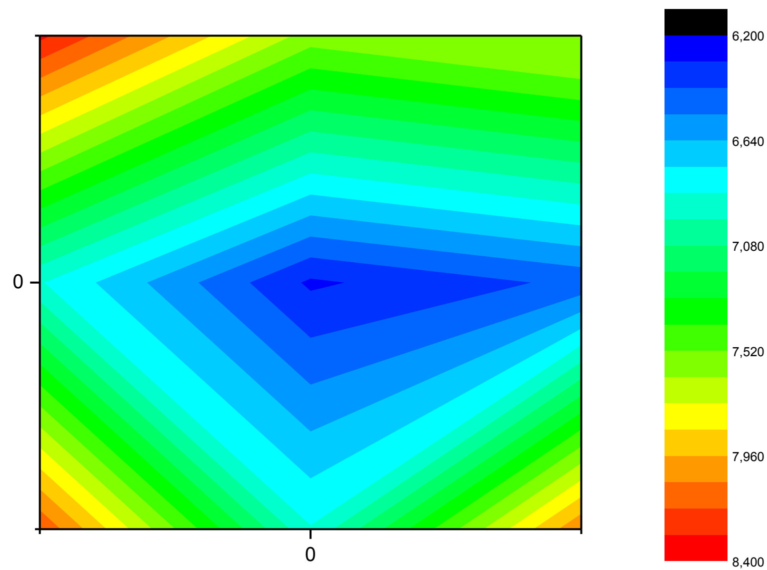

Figure 89. CT13 <e2> (3.31 eV) map

5.1.3. CdTe Surface Roughness Obtained From SE and AFM

In this section, the relation between imaginary part of the pseudo dielectric function of the CdTe epilayers and surface roughness values obtained from AFM was examined. If we look at the comparison of imaginary parts of the pseudo dielectric functions of CT1, CT3, CT4, CT5, CT6, CT10, CT14 and CT15 especially at 3.31 eV, which corresponds to the optical transition critical point E_1 of CdTe, the <e2> values indicate variation with the growth parameters (Figure 90).

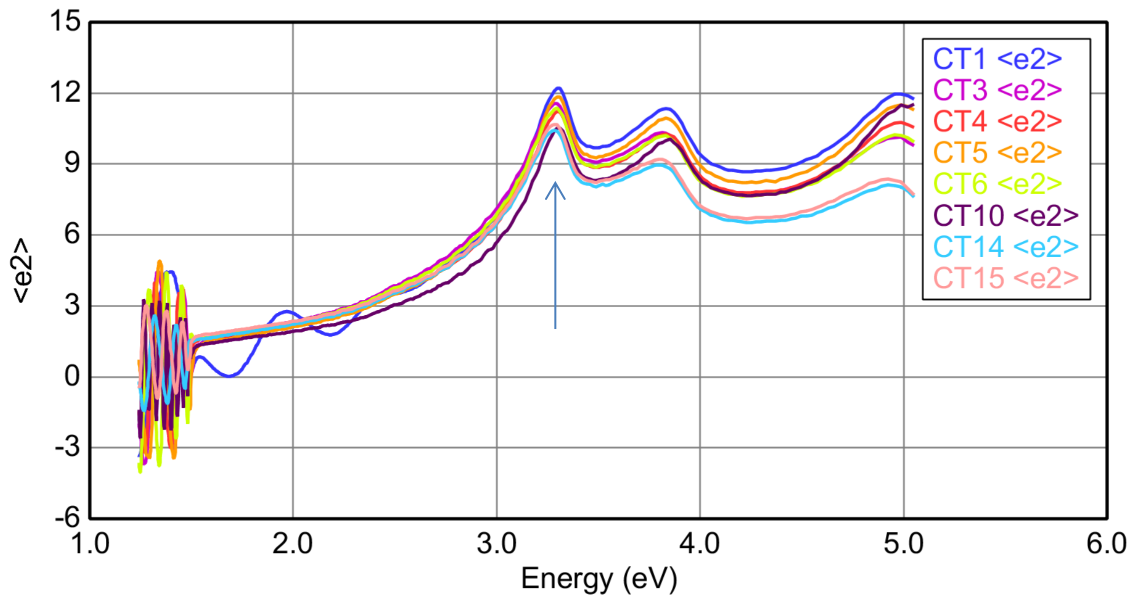

Figure 90. Comparison of imaginary parts of the pseudo dielectric functions of CT1, CT3, CT4, CT5, CT6, CT10, CT14 and CT15.

RMS roughness values of these eight samples (CT1, CT3, CT4, CT5, CT6, CT10, CT14 and CT15) versus <e2> values at 3.31 eV graphed in Figure 91 in order to examine the correlation between the peak values of <e2> to surface roughness. It can be seen that, as RMS roughness values decrease, <e2> values increase. This result was similar to those for CT9 maps given in the previous section.

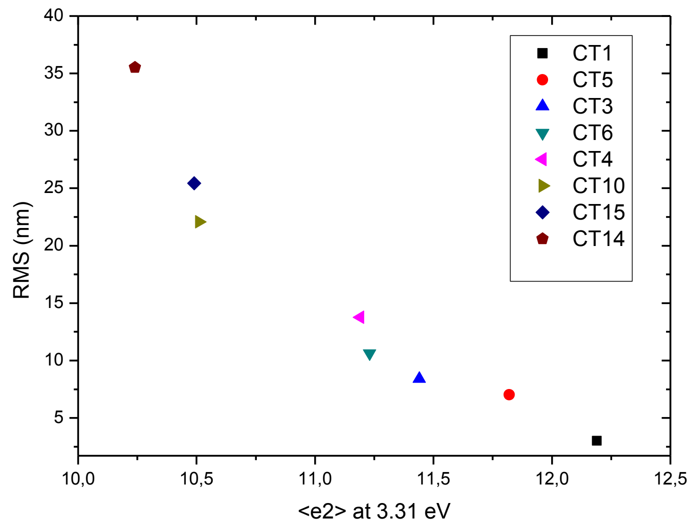

Figure 91. RMS roughness values versus <e2> values at 3.31 eV for CT1, CT3, CT4, CT5, CT6, CT10, CT14 and CT15.

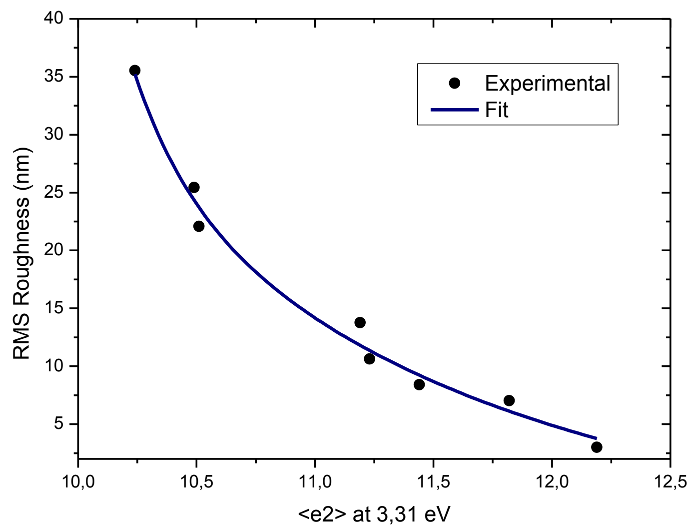

Figure 92. Exponantially fitted RMS roughness values versus <e2> values at 3.31 eV for CT1, CT3, CT4, CT5, CT6, CT10, CT14 and CT15.

This tendency was exponentially fitted (Figure 92) and <e2> dependent experimental roughness function was obtained. However in this function <e2> is taken as a single value only at 3.31 eV. This exponential function fitted the experimental results with the 97.1 % agreement.

$$\text{Rougness} = 4.52\times10^{20}\exp\left(-\frac{<e2>}{0,225}\right) + 2.43\times10^{3}\exp\left(-\frac{<e2>}{1,534}\right) + 7.64$$

The obtained function can be used for CdTe on GaAs samples to estimate roughness of the surface without actual measurements. As it was previously mentioned, E_1 value for CdTe at room temperature was about 3.31 eV, and it was the reason why we used this value for the analysis. In order to use such a relationship at different temperatures, it is required to establish a temperature dependent library of E_1 for <e2> values and corresponding AFM values whether similar relation would exists or not.

AFM images of these eight samples (CT1, CT3, CT4, CT5, CT6, CT10, CT14 and CT15) were given in Figure 93. Surface roughness conditions can also be seen in this figure.

Other surface images for four samples (CT5, CT6, CT15 and CT14) at 100x magnification were obtained by a Nomarski microscope (Figure 94).

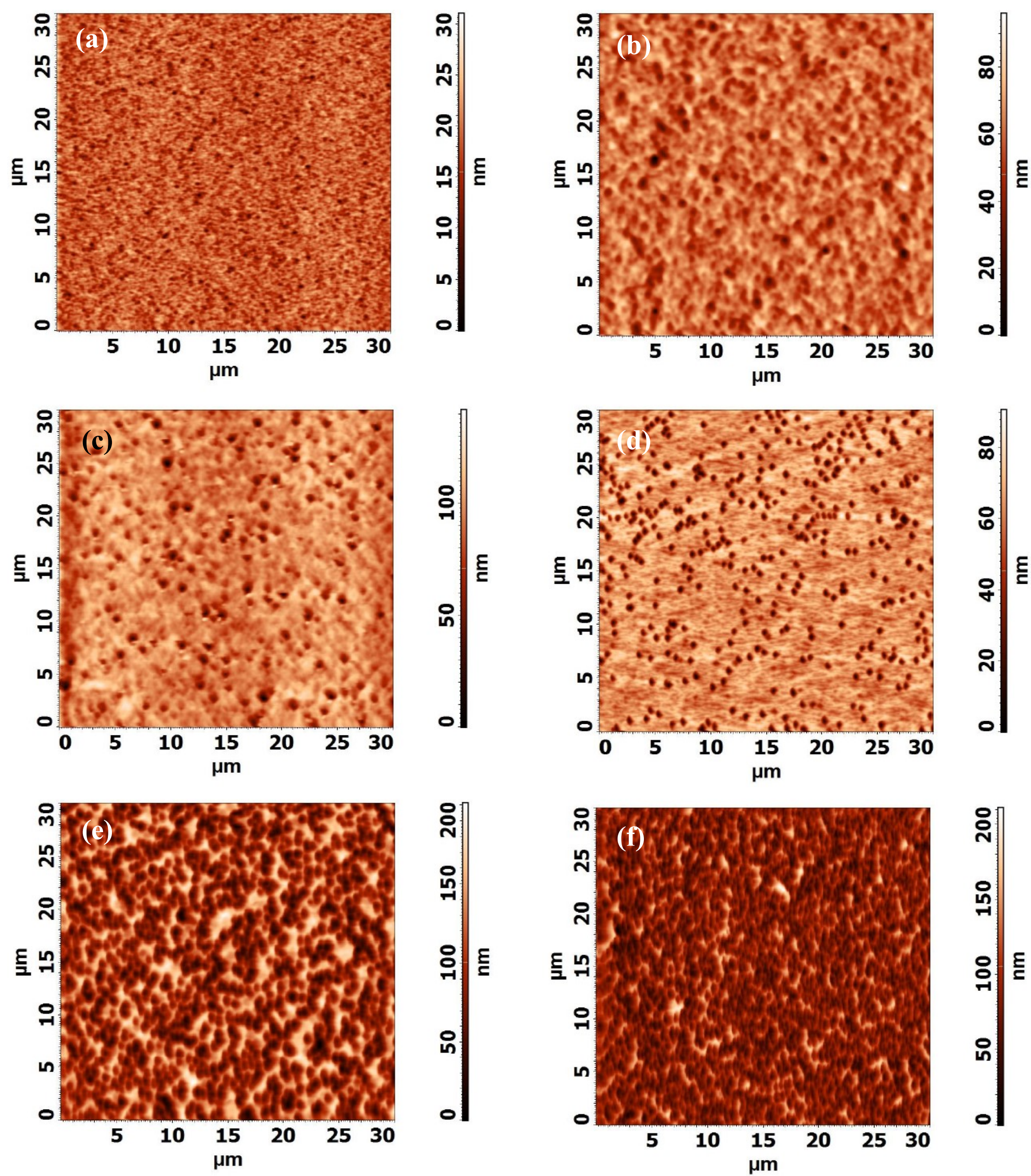

Figure 93. AFM images of (a) CT1 (rms=3.01 nm), (b) CT3 (rms=8.4 nm), (c) CT6 (rms=10.63 nm), (d) CT4 (rms=21.12 nm), (e) CT15 (rms=25.44 nm), (f) CT14 (rms=35.53 nm).

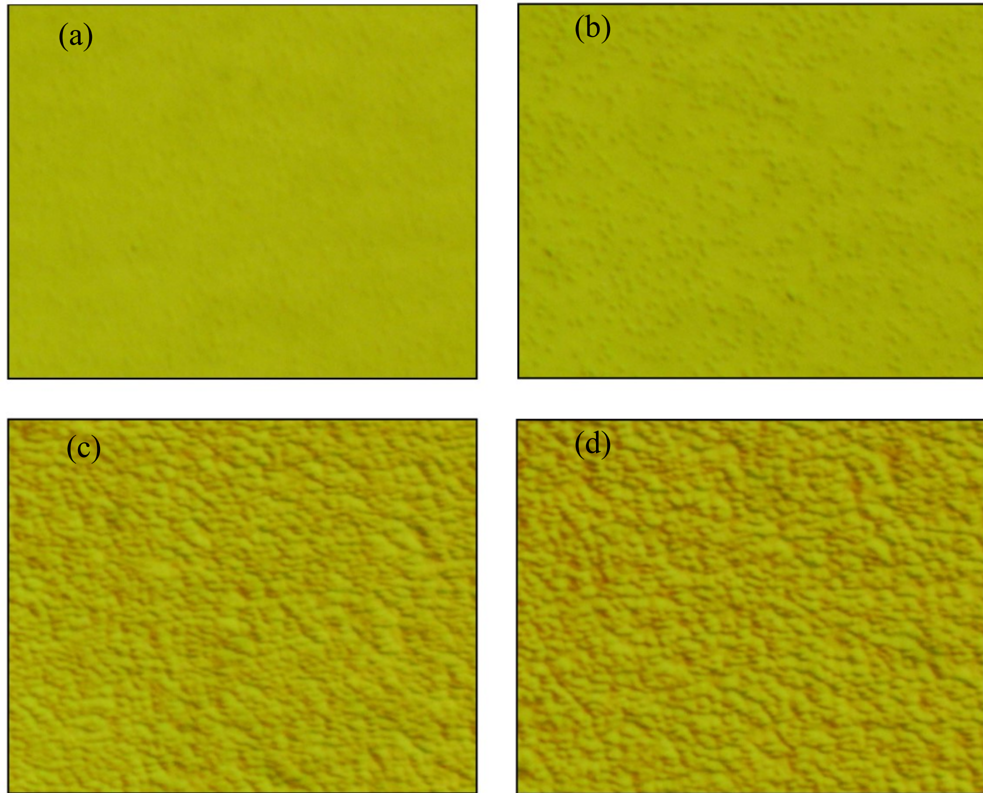

Figure 94. Surface images of (a) CT5, (b) CT6, (c) CT15, (d) CT14 samples obtained by Nomarski microscope (100x zoom).

5.2. MBE Grown CdTe Nucleation Layers

A nucleation layer is grown after oxide desorption of the substrate in order to have improved B-face nucleation and better crystallinity for the growth of the epitaxial CdTe layer [77]. The nucleation may occur in 2D or 3D islands [78]. A thin nucleation layer (~50 nm) results in reasonably good-quality surface morphology [79]. In some studies [80-83] ZnTe was also used as a nucleation layer in order to lessen lattice mismatch between CdTe and GaAs.

In this study, after oxide desorption of GaAs, we grew a CdTe nucleation layer in lower temperatures than CdTe nominal growth temperature for the samples from CT1 to CT15. In order to analyze the nucleation layers, we produced six samples that have only CdTe nucleation layer. For these six samples (CT16, CT17, CT18, CT19, CT20 and CT21) growth conditions were similar but annealing times and temperatures were different. Deoxidation processes were applied in 15 minutes at 629°C under 4.01x10^{-6} Torr As_4 flux. Nucleation layers were grown at 270°C in 1 minute under 6.84x10^{-7} Torr Te_2 flux. Beam equivalent pressure (BEP) of CdTe was 6.07x10^{-7} Torr. After the

growth of CdTe nucleation layer, the samples were annealed as a last process in MBE chamber. For CT16, CT17, CT18, CT19, CT20 and CT21 annealing time and temperatures were 5 min at 350°C, 5 min at 345°C, 10 min at 360°C, 3 min 320°C, 5 min 330°C and 5 min 335°C, respectively. CdTe growth was performed after annealing of nucleation layer only for sample CT21. The growth conditions can be seen in Table 8.

Table 8. The growth conditions of CT16, CT17, CT18, CT19, CT20 and CT21.

	CT16	**CT17**	**CT18**	**CT19**	**CT20**	**CT21**
Annealing Time	5 min	5 min	10 min	3 min	5 min	5 min
Annealing temperature	350°C	345 ^{o}C	360 ^{o}C	320 ^{o}C	330 ^{o}C	335 ^{o}C
CdTe Growth	-	-	-	-	-	22.5 min at 350 ^{o}C
CdTe Thickness	5.67nm	5.70nm	1.80nm	11.10nm	5.83nm	159.94nm

The *ex situ* ellipsometric measurements were carried out for these 6 samples and different ellipsometric models were tried. First model was CdTe on Oxide on GaAs that was tried to determine whether oxide on GaAs could be completely removed in the deoxidation process or not. The second model was Oxide on CdTe on GaAs which was also tried to test whether a better fit would be obtained or not. For these two models MSE values and thickness values of CdTe nucleation layers and oxide layers were given in Table 9. Alternately, Oxide/CdTe/Oxide/GaAs model was also tried, but the data fitting was failed and physically meaningful CdTe dielectric function could not be found.

Table 9. SE data analysis results according to two different models.

Sample	**CdTe/Oxide/ GaAs Model**				**Oxide/ CdTe/ GaAs Model**			
	MSE	**CdTe Thickness (nm)**	**Oxide Thickness (nm)**	**Total Thickness (nm)**	**MSE**	**CdTe Thickness (nm)**	**Oxide Thickness (nm)**	**Total Thickness (nm)**
CT16	1.806	5.67	8.57	**14.24**	1.871	8.02	7.38	**15.40**
CT17	2.012	5.70	8.56	**14.26**	3.625	8.45	7.08	**15.53**
CT18	1.944	1.80	8.27	**10.07**	1.752	4.17	4.25	**8.42**
CT19	3.077	11.10	10.33	**21.43**	1.634	25.21	3.28	**28.49**
CT20	1.944	5.83	8.83	**14.66**	3.136	8.89	7.07	**15.96**
CT21	1.737	159.94	-0.24	**159.7**	1.650	150.80	2.79	**152.45**

The obtained oxide thickness values in Table 9 especially in CdTe/Oxide/GaAs model are not reasonable because epiready GaAs wafer includes already about 3 nm thermal oxide. It means that the ellipsometric data analysis of very thin films may not be utilized reliably. However, these results give information about the thickness of samples relatively. For example, we can compare CT16, CT17 and CT20 for which their similar behavior of the real part of the pseudo dielectric function data and model fit can be seen in Figure 95. Their thickness values were also obtained very close to each other. According to these results, CT18 had thinnest CdTe nucleation layer and CT 21 had thickest CdTe layer. In order to compare CT18 and CT21 ellipsometric data for bare GaAs and a CdTe on GaAs sample CT7 were also given in Figure 96. As it can be easily seen in this figure that CT18 is very close to GaAs that the peak values corresponding to E_1 and $E_1+\Delta$ transition of GaAs are more dominant for CT18. Those values of the sample CT21 was very close to those of the sample CT7.

If we return to the Figure 95, CT16, CT17 and CT20 include peaks both for GaAs and for CdTe. The critical points for GaAs were indicated with blue arrows and the critical points for CdTe were indicated with green arrows. If two material CdTe and GaAs appear in the ellipsometric <e2> data from which it can be inferred that CdTe nucleation layer were very thin that the substrate was interfering with the measurements.

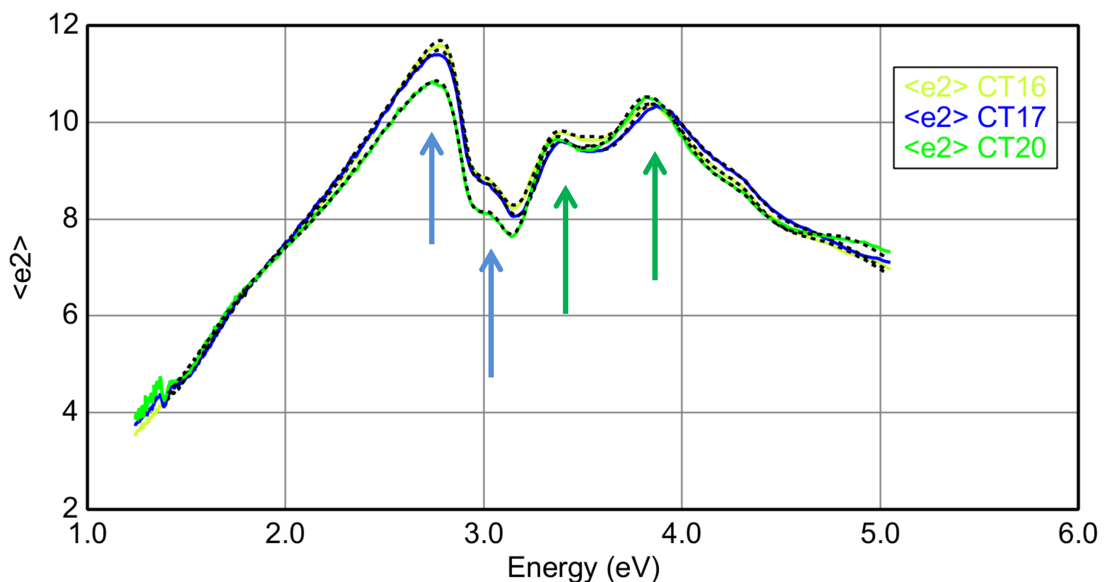

Figure 95. Comparison of imaginary parts of the pseudo dielectric functions of CT16 (8.02 nm), CT17 (8.45 nm) and CT20 (8.89 nm) nucleation layer samples.

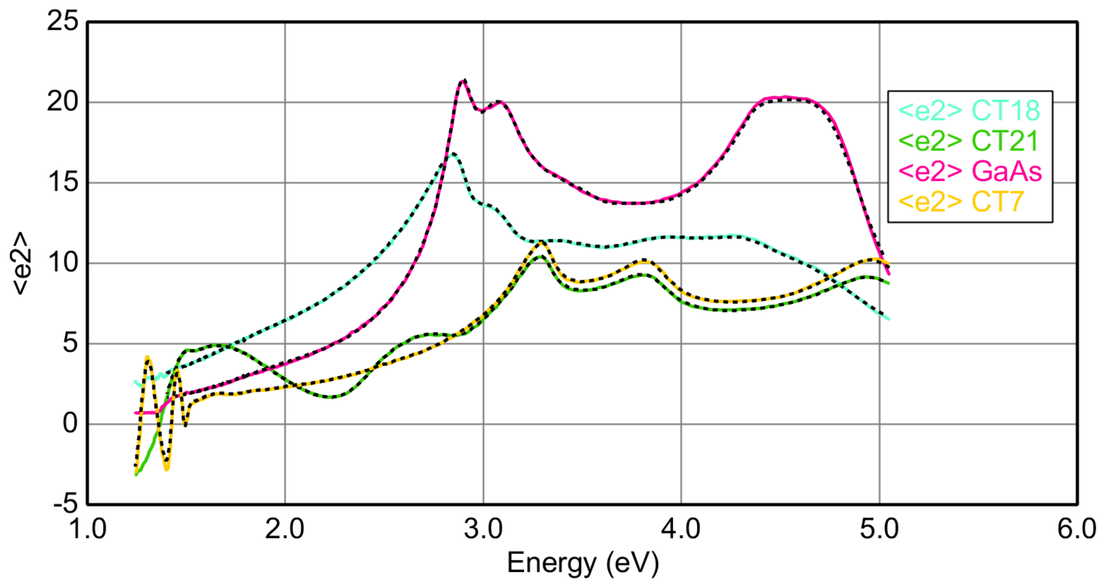

Figure 96. Comparison of imaginary parts of the pseudo dielectric functions of CT18 (~4 nm) and CT21 (~150 nm), nucleation layer samples and GaAs and CT7 (~1000 nm).

In Figure 97, comparison of the imaginary parts of the pseudo dielectric functions of CT18 (~4 nm), CT17 (~8 nm), CT19 (~25 nm) and CT21 (~150 nm) samples was given. It can be seen that, as the thickness of the CdTe nucleation layer increase the shape of the graphs change dramatically and the peaks for CdTe dominate. These thickness values were obtained from Oxide/CdTe/GaAs model.

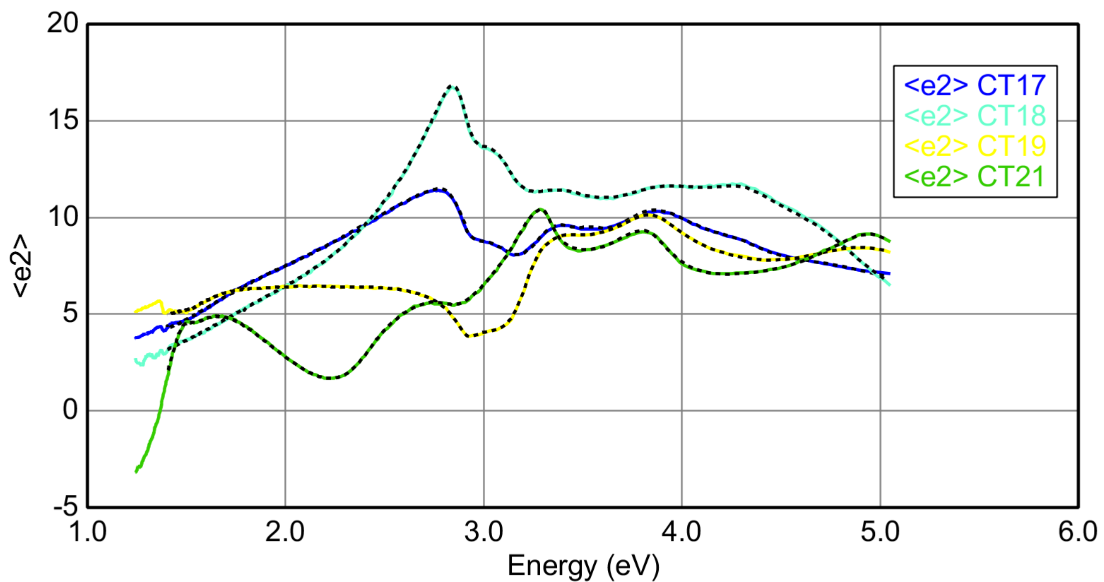

Figure 97. Comparison of imaginary parts of the pseudo dielectric functions of CT18 (~4 nm), CT17 (~8 nm), CT19 (~25 nm) and CT21 (~150 nm) nucleation layer samples.

In order to determine which model have physically more meaningful result, the comparison of imaginary parts of the dielectric functions of CdTe layer of CT17 which were obtained from two different models (CdTe/Oxide/GaAs and Oxide/CdTe/GaAs) and the dielectric functions of CdTe in the software library is given in Figure 98. It can be easily inferred from this comparison that the dielectric function of CdTe obtained from CdTe/Oxide/GaAs model had similar behavior with CdTe in the software library than those obtained from Oxide/CdTe/GaAs model.

Another comparison is given in Figure 99 which includes imaginary parts of the dielectric functions which were obtained from CdTe/Oxide/GaAs model for CT16, CT17, CT20 and CT21 and imaginary part of the dielectric function of CdTe in the software library. The dielectric function behavior of CT21 found as closer to that of CdTe in the library.

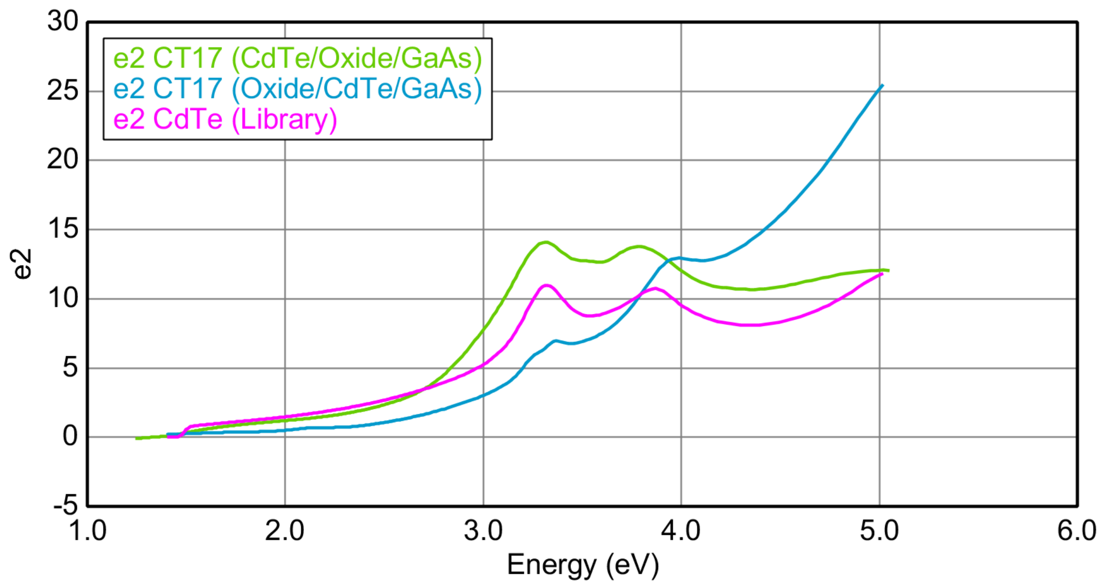

Figure 98. Comparison of imaginary parts of the dielectric functions which were obtained from two different layer model (CdTe/Oxide/GaAs and Oxide/CdTe/GaAs) for CT17 and CdTe in the software library.

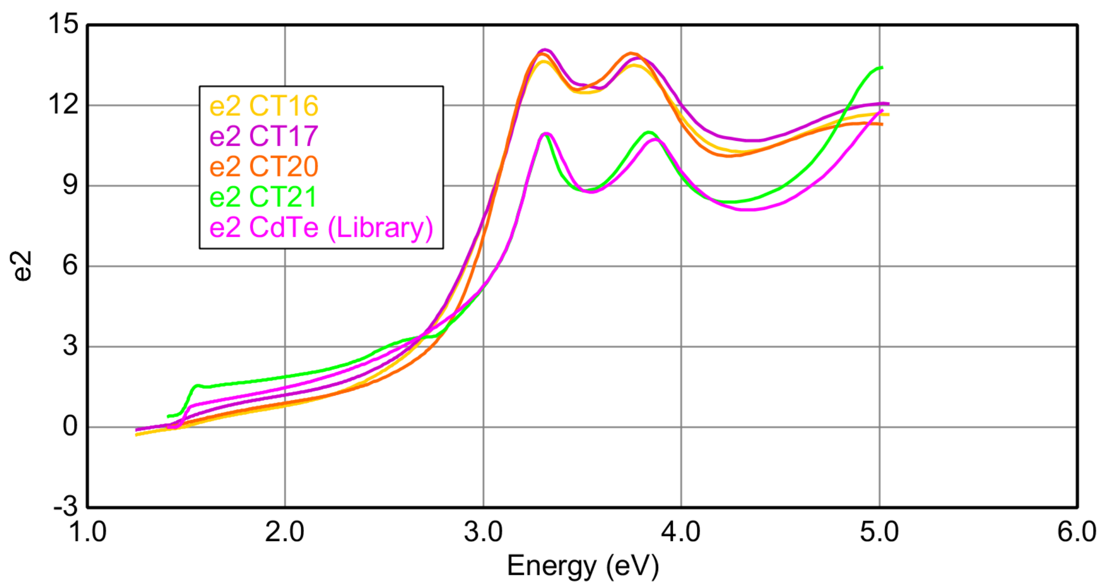

Figure 99. Comparison of imaginary parts of the dielectric functions which were obtained from CdTe/Oxide/ GaAs layer model for CT16, CT17, CT20 andCT21 and imaginary part of the dielectric function of CdTe in the software library.

CHAPTER 6

CONCLUSIONS AND FUTURE STUDIES

In this study some optical properties of CdTe grown on GaAs by MBE were determined by SE. In addition, some important optical parameters of alternative (GaAs) and lattice matched CdZnTe substrate material were obtained. Data was collected for the range from 2.4 eV to 5.05 eV (220-1000 nm) and the dielectric functions of these materials were determined by using proper general oscillators. Excellent agreement was established between experimental SE measurement and the fitting which was achieved by using these constructed dielectric functions. MSE values were acceptably small for all fits. A roughness layer (or EMA layer) was not included but instead oxide layer was included to the optical models in the *ex-situ* data analysis of these materials. A better fits were obtained this way. Otherwise, unphysical thickness values such as negative roughnesses were frequently obtained by adding surface roughness layers to the present optical models.

Band structures and critical transition energies of CdTe, GaAs and CdZnTe materials were determined and compared with other published results and these critical energy values were found to be compatible with the literature values. The critical points, except the bandgap, were determined by taking the first derivative of the imaginary part of the dielectric function of the material. The bandgap energy was determined both by taking the second derivative of the imaginary part of the dielectric function and by taking the first derivative of the real part of the dielectric function. The difference between the values of the bandgaps obtained from these two methods was about 0.001 eV. For the consistency, first derivative of the real part of the dielectric function was used to report bandgap energies of the samples. The broadening parameters of the oscillators used in the modeling of the dielectric function were tried to be associated with the lifetime of the excited electrons in the conduction band. However, the values found were higher than those reported in the literature.

The temperature dependencies of the critical transition energies of CdTe were determined. The sample temperature was varied from room temperature to about 118°C. It was seen that, as the temperature increased, energy values of the critical points were

decreased about linearly for this range of temperature. As a result, it was shown that the critical points including E_g, E_1 and $E_1+\Delta$ can be used to determine the temperature of CdTe. In a future study these parameters can be used for temperature determination during *in-situ* process.

Thickness values obtained from SE and FTIR results were correlated for all epitaxially grown CdTe samples. These values were linearly fitted and a positive Pearson correlation coefficient was obtained as 98.8% indicating very well agreement between the two techniques. A thickness variation map obtained by e*x-situ* ellipsometric measurements of sample CT9 grown over 4-inch diameter wafer yielded variation of just 25 nm over the surface. On the other hand, it was shown that by mapping optical properties (refractive index or <e2> at 3.31 eV) of the same sample, four regions with different optical properties appeared. These four regions were also distinguished by bare eye easily.

Existence of a dependency between roughness obtained by AFM measurements and <e2> values at E1 critical point (3.31eV) was demonstrated for some of the samples. It was found that surface roughness is exponentially decreasing function of <e2> at 3.31 eV. Since it was not possible to obtain precise surface roughness of the sample by adding the EMA roughness layer in the optical model used, the <e2> parameters at 3.31eV were thought as convenient way to determine surface roughness. In a future study relation between roughness and <e2> at E_1 can be determined at different temperatures.

Thickness determination and model selection were carried out for the nucleation layer of the CdTe on GaAs. The behavior of the pseudo dielectric functions was explained. It was shown that the experimental data of the nucleation layer included signals both from GaAs substrate and CdTe epilayer even at measurements at high energy ranges.

REFERENCES

1. Rogalski, A., HgCdTe infrared detector material: history, status and outlook. Reports on Progress in Physics, 2005. 68(10): p. 2267.

2. Zanatta, J., et al., Heteroepitaxy of HgCdTe (211) B on Ge substrates by molecular beam epitaxy for infrared detectors. Journal of electronic materials, 1998. 27(6): p. 542-545.

3. Sporken, R., et al., Molecular beam epitaxial growth of CdTe and HgCdTe on Si (100). Applied Physics Letters, 1989. 55(18): p. 1879-1881.

4. Zanatta, J., et al., Molecular beam epitaxy growth of HgCdTe on Ge for third-generation infrared detectors. Journal of electronic materials, 2006. 35(6): p. 1231-1236.

5. Arias, J., et al., Dislocation density reduction by thermal annealing of HgCdTe epilayers grown by molecular beam epitaxy on GaAs substrates. Journal of Vacuum Science & Technology B, 1991. 9(3): p. 1646-1650.

6. Finger, G., et al. Performance of large-format HgCdTe and InSb arrays for low-background applications. in Astronomical Telescopes and Instrumentation. 2000. International Society for Optics and Photonics.

7. Carmody, M., et al., LWIR HgCdTe on Si detector performance and analysis. Journal of electronic materials, 2006. 35(6): p. 1417-1422.

8. Badano, G., et al., In situ real-time analysis of the MBE growth of CdTe on Ge: A comparison of ellipsometry data analysis techniques. Journal of crystal growth, 2006. 296(2): p. 129-134.

9. Badano, G., X. Baudry, and I.C. Robin, In Situ Spectroscopic Ellipsometry of Rough Surfaces: Application to CdTe (211) B/Ge (211) Grown by Molecular-Beam Epitaxy. Journal of electronic materials, 2009. 38(8): p. 1652-1660.

10. Edwall, D., et al., Composition control of long wavelength MBE HgCdTe using In-situ spectroscopic ellipsometry. Journal of electronic materials, 2001. 30(6): p. 643-646.

11. Lennon, C., et al., Real-Time In Situ Monitoring of GaAs (211) Oxide Desorption and CdTe Growth by Spectroscopic Ellipsometry. Journal of electronic materials, 2012. 41(10): p. 2965-2970.

12. Drude, P., Bestimmung der optischen Constanten der Metalle. Annalen der Physik, 1890. 275(4): p. 481-554.

13. Chen, J., Spectroscopic Ellipsometry Studies of II-VI Semiconductor Materials and Solar Cells, 2010, University of Toledo.

14. Palik, E.D., Handbook of optical constants of solids. Vol. 3. 1998: Academic press.

15. Rothen, A., The ellipsometer, an apparatus to measure thicknesses of thin surface films. Review of Scientific Instruments, 1945. 16(2): p. 26-30.

16. Cahan, B. and R. Spanier, A high speed precision automatic ellipsometer. Surface Science, 1969. 16: p. 166-176.

17. Jasperson, S. and S. Schnatterly, An improved method for high reflectivity ellipsometry based on a new polarization modulation technique. Review of Scientific Instruments, 1969. 40(6): p. 761-767.

18. Aspnes, D. and A. Studna, High precision scanning ellipsometer. Applied Optics, 1975. 14(1): p. 220-228.

19. Collins, R., Automatic rotating element ellipsometers: Calibration, operation, and real-time applications. Review of Scientific Instruments, 1990. 61(8): p. 2029-2062.

20. Fujiwara, H., Spectroscopic ellipsometry: principles and applications. 2007: John Wiley & Sons.

21. Born, M. and E. Wolf, Principles of optics: electromagnetic theory of propagation, interference and diffraction of light. 1999: CUP Archive.

22. Jackson, J.D. and J.D. Jackson, Classical electrodynamics. Vol. 3. 1962: Wiley New York etc.

23. Johs, B.D., et al. Recent developments in spectroscopic ellipsometry for in-situ applications. in International Symposium on Optical Science and Technology. 2001. International Society for Optics and Photonics.

24. http://www.physik.uni-kl.de/hillebrands/research/methods/molecular-beam-epitaxy/.

25. http://www.jawoollam.com/.

26. http://www.jawoollam.com/pdf/CompleteEASE_Brochure.pdf.

27. Wooten, Frederick. Optical properties of solids. Vol. 111. New York: Academic press, 1972.

28. Collins, R.W. and K. Vedam, Optical properties of solids. Encyclopedia of Applied Physics, 1995. 12: p. 285.

29. Roessler, D., Kramers-Kronig analysis of reflection data. British Journal of Applied Physics, 1965. 16(8): p. 1119.

30. Herzinger, Craig M., and Blaine D. Johs. "Dielectric function parametric model, and method of use." U.S. Patent No. 5,796,983. 18 Aug. 1998.

31. Adachi, S., T. Kimura, and N. Suzuki, Optical properties of CdTe: experiment and modeling. Journal of applied physics, 1993. 74(5): p. 3435-3441.

32. Kim, C., et al., Temperature dependence of the optical properties of CdTe. Physical Review B, 1997. 56(8): p. 4786.

33. Benhlal, J., et al., Temperature dependence of the dielectric function and of the parameters of critical point transitions of CdTe. Optical Materials, 1999. 12(1): p. 143-156.

34. Yao, H., P.G. Snyder, and J.A. Woollam, Temperature dependence of optical properties of GaAs. Journal of applied physics, 1991. 70(6): p. 3261-3267.

35. Chelikowsky, J.R. and M.L. Cohen, Nonlocal pseudopotential calculations for the electronic structure of eleven diamond and zinc-blende semiconductors. Physical Review B, 1976. 14(2): p. 556.

36. Erman, M., et al., Optical properties and damage analysis of GaAs single crystals partly amorphized by ion implantation. Journal of applied physics, 1984. 56(10): p. 2664-2671.

37. Adachi, S., Optical properties of crystalline and amorphous semiconductors. 1999.

38. Aoki, T. and S. Adachi, Temperature dependence of the dielectric function of Si. Journal of applied physics, 1991. 69(3): p. 1574-1582.

39. Suzuki, T. and S. Adachi, Optical properties of amorphous Si partially crystallized by thermal annealing. Japanese journal of applied physics, 1993. 32(11R): p. 4900.

40. Lautenschlager, P., et al., Temperature dependence of the dielectric function and interband critical points in silicon. Physical Review B, 1987. 36(9): p. 4821.

41. Lautenschlager, P., et al., Interband critical points of GaAs and their temperature dependence. Physical Review B, 1987. 35(17): p. 9174.

42. Fujiwara, H., M. Kondo, and A. Matsuda, Real-time spectroscopic ellipsometry studies of the nucleation and grain growth processes in microcrystalline silicon thin films. Physical Review B, 2001. 63(11): p. 115306.

43. Volintiru, I., M. Creatore, and M. Van De Sanden, In situ spectroscopic ellipsometry growth studies on the Al-doped ZnO films deposited by remote plasma-enhanced metalorganic chemical vapor deposition. Journal of applied physics, 2008. 103(3): p. 033704.

44. Hottier, F. and R. Cadoret, In situ observation of polysilicon nucleation and growth. Journal of Crystal Growth, 1982. 56(2): p. 304-312.

45. Shirai, H., T. Arai, and T. Nakamura, Control of the initial stage of nanocrystallite silicon growth monitored by in-situ spectroscopic ellipsometry. Applied surface science, 1997. 113: p. 111-115.

46. Seitz, H. and B. Schröder, In-situ ellipsometric studies on epitaxially grown silicon by hot-wire CVD. Solid state communications, 2000. 116(11): p. 625-629.

47. Kumar, S. and B. Drevillon, A real time ellipsometry study of the growth of amorphous silicon on transparent conducting oxides. Journal of Applied Physics, 1989. 65(8): p. 3023-3034.

48. Beydaghyan, G., et al., Ex situ ellipsometric investigation of nanocolumns inclination angle of obliquely evaporated silicon thin films. Applied Physics Letters, 2005. 87(15): p. 153103.

49. Britt, J. and C. Ferekides, Thin-film CdS/CdTe solar cell with 15.8% efficiency. Applied Physics Letters, 1993. 62(22): p. 2851-2852.

50. Cusano, D., CdTe solar cells and photovoltaic heterojunctions in II–VI compounds. Solid-State Electronics, 1963. 6(3): p. 217-218.

51. Smith, D., T. McGill, and J. Schulman, Advantages of the HgTe-CdTe superlattice as an infrared detector material. Applied Physics Letters, 1983. 43(2): p. 180-182.

52. Simingalam, S., et al., Development and fabrication of extended short wavelength infrared HgCdTe sensors grown on CdTe/Si substrates by molecular beam epitaxy. Solid-State Electronics, 2014.

53. Lawson, W., et al., Preparation and properties of HgTe and mixed crystals of HgTe-CdTe. Journal of Physics and Chemistry of Solids, 1959. 9(3): p. 325-329.

54. Reine, M., Fundamental properties of mercury cadmium telluride. Encyclopedia of Modern Optics, 2004.

55. Vilela, M., et al., HgCdTe Molecular Beam Epitaxy Growth Temperature Calibration Using Spectroscopic Ellipsometry. Journal of electronic materials, 2012. 41(10): p. 2937-2942.

56. Jacobs, R., et al., Relevance of thermal mismatch in large-area composite substrates for HgCdTe heteroepitaxy. Journal of Electronic Materials, 2008. 37(9): p. 1480-1487.

57. http://en.wikipedia.org/wiki/Indium_antimonide.

58. Özden, S., Characterization of Defect Structure of Epitaxial CdTe Films, in Physics2014, IZTECH.

59. Dhanaraj, G., et al., Crystal Growth Techniques and Characterization: An Overview, in Springer Handbook of Crystal Growth. 2010, Springer. p. 3-16.

60. Chen, Y., et al., MBE-Grown ZnTe/Si, a Low-Cost Composite Substrate. Journal of electronic materials, 2012. 41(10): p. 2917-2924.

61. Kuphal, E. "Liquid phase epitaxy." Applied Physics A 52.6 (1991): 380-409

62. MARKS, J., J. SCHINDLER, and C.R. KANNEWURF, Metalorganic chemical vapor deposition. 1982.

63. Cho, A. and J. Arthur, Molecular beam epitaxy. Progress in Solid State Chemistry, 1975. 10: p. 157-191.

64. Atay, F., et al., Optical, structural and surface characterization of CdO: Mg films. Journal of Materials Science: Materials in Electronics, 2011. 22(5): p. 492-498.

65. Kim, C.C. and S. Sivananthan, Modeling the optical dielectric function of II-VI compound CdTe. Journal of applied physics, 1995. 78(6): p. 4003-4010.

66. Cardona, M. and D. Greenaway, Fundamental reflectivity and band structure of ZnTe, CdTe, and HgTe. Physical Review, 1963. 131(1): p. 98.

67. Arwin, H. and D. Aspnes, Nondestructive analysis of Hg1− xCdxTe (x= 0.00, 0.20, 0.29, and 1.00) by spectroscopic ellipsometry. II. Substrate, oxide, and interface properties. Journal of Vacuum Science & Technology A, 1984. 2(3): p. 1316-1323.

68. Kumazaki, K., et al., Interband Critical Point Parameters Determined by Ellipsometry in CdxHg1− xSe. physica status solidi (b), 1989. 156(1): p. 371-376.

69. Li, J., et al. Spectroscopic ellipsometry studies of thin film CdTe and CdS: From dielectric functions to solar cell structures. in Photovoltaic Specialists Conference (PVSC), 2009 34th IEEE. 2009. IEEE.

70. http://en.wikipedia.org/wiki/Zinc_telluride.

71. Sridharan, M., et al., Optical constants of vacuum-evaporated Cd0. 96Zn0. 04Te thin films measured by spectroscopic ellipsometry. Journal of Materials Science: Materials in Electronics, 2002. 13(8): p. 471-476.

72. Sell, D., H. Casey Jr, and K. Wecht, Concentration dependence of the refractive index for n-and p-type GaAs between 1.2 and 1.8 eV. Journal of Applied Physics, 1974. 45(6): p. 2650-2657.

73. Ibrahim, Z., et al., First-principles calculation of the temperature dependence of the optical response of bulk GaAs. arXiv preprint arXiv:0710.1020, 2007.

74. Sacks, R., et al., Growth related interference effects in band edge thermometry of semiconductors. Journal of Vacuum Science & Technology B, 2005. 23(3): p. 1247-1251.

75. Farrer, I., et al., Substrate temperature measurement using a commercial band-edge detection system. Journal of Crystal Growth, 2007. 301: p. 88-92.

76. He, L., et al. "MBE HgCdTe on Si and GaAs substrates." Journal of Crystal Growth 301 (2007): 268-272.

77. Zhao, W., et al., Microstructural Characterization of CdTe (211) B/ZnTe/Si (211) Heterostructures Grown by Molecular Beam Epitaxy. Journal of electronic materials, 2011. 40(8): p. 1733-1737.

78. Altsinger, R., et al., Nucleation and growth during molecular beam epitaxy (MBE) of Si on Si (111). Surface Science, 1988. 200(2): p. 235-246.

79. Shintri, S., et al., Effect of As Passivation on Vapor-Phase Epitaxial Growth of Ge on (211) Si as a Buffer Layer for CdTe Epitaxy. Journal of electronic materials, 2011. 40(8): p. 1637-1641.

80. Nishino, H., T. Saito, and Y. Nishijima, VIII ratio dependence of surface macrodefects in CdTe/ZnTe/GaAs (100) growth by metalorganic vapor phase epitaxy. Journal of crystal growth, 1996. 165(3): p. 227-232.

81. Mizeikis, V., et al., Carrier transport and recombination in MOVPE-grown CdTe/ZnTe/GaAs and ZnTe/GaAs heterostructures. Journal of crystal growth, 2000. 214: p. 234-239.

82. Kim, T., H. Park, and J. Lee, Interfacial stages of the ZnTe/GaAs strained heterostructures grown by temperature-gradient vapor transport deposition at low temperature. Applied physics letters, 1994. 64(19): p. 2526-2528.

83. Leo, G., et al., Influence of a ZnTe buffer layer on the structural quality of CdTe epilayers grown on (100) GaAs by metalorganic vapor phase epitaxy. Journal of Vacuum Science & Technology B, 1996. 14(3): p. 1739-1744.